# **Controls of Subsurface Geology on Barrier Islands Breaching**

Final Report May 2025

GLO CONTRACT NO. 23-020-003-D597

Prepared by:

Ramadan Abdelrehim, Ph.D. Candidate

Texas A&M University-Corpus Christi 6300 Ocean Dr., Unit 5850 Corpus Christi, Texas 78412 Phone: 361-775-8071

Email: <u>rabdelrehim@islander.tamucc.edu</u>

Submitted to: Texas General Land Office 1700 Congress Ave. Austin, TX 78701-1495

This report was funded in part by a Texas Coastal Management Program grant approved by the Texas Land Commissioner, providing financial assistance under the Coastal Zone Management Act of 1972, as amended, awarded by the National Oceanic and Atmospheric Administration (NOAA), Office for Coastal Management, pursuant to NOAA Award No. NA22NOS4190148. The views expressed herein are those of the author and do not necessarily reflect the views of NOAA, the U.S. Department of Commerce, or any of their subagencies.





# **List of Abbreviations**

Abbreviation	Meaning	
<b>CMP-27</b>	Coastal Management Program, Cycle 27 grant round	
DEM	Digital Elevation Model	
EM	Electromagnetic	
EM-31	Geonics Ltd. terrain-conductivity meter model EM-31	
FDEM	Frequency-Domain Electromagnetic Method	
FWL	Fresh-Water Lens	
GLO	Texas General Land Office	
GOM	Gulf of Mexico	
GNSS	Global Navigation Satellite System	
GSF	Geologic-Stratigraphic Feature(s)	
LiDAR	Light Detection and Ranging	
LM	Laguna Madre (back-barrier lagoon)	
NAVD88	North American Vertical Datum of 1988	
PV	"Profile Vertical" survey-line designation (e.g., PV11)	
RTK	Real-Time Kinematic (high-precision GNSS)	
RMS	Root-Mean-Square (inversion mis-fit statistic)	
RX	Receiver coil (in EM systems)	
SAGEEP	Symposium on the Application of Geophysics to Engineering and Environmental Problems	
SEG	Society of Exploration Geophysicists	
TDEM / TEM	Time-Domain (Transient) Electromagnetic Method	
TX	Transmitter loop/coil (in EM systems)	
USGS	United States Geological Survey	

## **Executive Summary**

The CMP-27 project, "Controls of Subsurface Geology on Barrier-Island Breaching" (Texas GLO Contract No. 23-020-003-D597), set out to determine how the hidden architecture beneath northern Padre Island shapes the dunes that defend the coast and, ultimately, where the barrier is most likely to fail during storms and become contaminated by salt-water intrusion. Under the revised work plan the team completed four sequential tasks: (1) collecting electromagnetic (EM) data and groundwater samples; (2) processing those measurements and merging them with high-resolution LiDAR to map subsurface geologic-stratigraphic features (GSF) and dune geometry; (3) transforming the science into education, outreach, and conference products; and (4) reporting quarterly progress while delivering a final synthesis.

Across over thirty field campaigns, investigators acquired more than forty-five line-kilometers of EM-31 apparent-conductivity profiles, imaging to roughly six meters depth, and about one hundred time-domain EM soundings that resolve resistivity contrasts to thirty meters. These geophysical transects were co-located with one-meter-resolution USGS LiDAR, RTK-GNSS control points, and fifty-four wells and auger holes for subsurface geology and salinity verification, producing an integrated geodatabase covering forty-five square kilometers of paired subsurface–surface observations. Non-parametric statistics revealed a strong inverse relationship between shallow conductivity and elevation (correlation coefficient = -0.69, p  $\ll 0.01$ ), confirming that low, narrow locations coincide with heightened saltwater intrusion and more conductive sediments that invite storm-surge penetration. Inversion of the TDEM soundings further revealed a three-layer framework: (i) a fresh-to-brackish fresh-water lens (FWL) averaging 8  $\pm$  5 m thick, (ii) an underlying brackish/saline zone 1–19 m thick, and (iii) a Pleistocene clay aquitard that shoals from more than 18 m beneath the central ridge to less than 6

m near the lagoon margins. Where the clay base rises and the FWL pinches to under four meters, dunes are noticeably lower, saline intrusion is greater, and wave energy can scour to the clay, pre-conditioning the island for breakthrough.

By synthesizing elevation, conductivity, FWL thickness, resistivity, and clay-depth grids, the team classified the landscape into four vulnerability bands. Class I (0–1 m NAVD88) and Class II (1–3 m) sectors—shown in red and orange, respectively, on the final breach-susceptibility map—are inundated annually by spring tides, tropical storms, or weak Category-1 hurricanes; they lack the sand volume needed to recover after repeated overwash. Class III (3–5 m) and Class IV (> 5 m) ridges, by contrast, overtop only in major hurricanes and serve as the island's natural backbone. Overlaying these classes with FDEM and TDEM data isolated four 500- to 2 000-metre-wide "pinch-point" corridors where thin Class I–II ridges coincide with conductivities above 300 mS m<sup>-1</sup>, thin FWL, and shallow clay depth: one just north of Packery Channel (north of the island's most heavily developed stretch), a second at the far northern edge of the study area, a third near the southern end of the developed section, and a fourth at the study area's southern limit. Historical aerial imagery shows that the first two locations opened repeatedly during Hurricanes Celia (1970), Allen (1980), and Hanna (2020), validating the model's predictive skill.

The project also met its education and outreach commitments. Four Ph.D., two master's, and three undergraduate students were trained in field geophysics and coastal GIS; one laboratory module was incorporated into TAMU-CC's Geophysics curriculum; and preliminary findings were presented at the 2024 Geological Society of America (GSA) Connects meeting, the 2024 Symposium on the Application of Geophysics to Engineering and Environmental Problems (SAGEEP), and the Society of Exploration Geophysicists (SEG) IMAGE meeting 2024. One

peer-reviewed manuscript has been published in The Leading Edge, and another is under review with the Journal of Hydrology.

In sum, this final report provides the Texas General Land Office with a clearer picture of how Padre Island's invisible subsurface dictates its visible—and vulnerable—surface. By coupling dense EM measurements with LiDAR-derived morphology, the project advances coastal management beyond heuristic elevation rules toward a quantitative model, where sand volume, freshwater storage, and clay depth run thin, the probability of breaching surges. Implementing the recommended zoning, dune-restoration, and monitoring measures in the identified corridors will not only safeguard high-value property and infrastructure but also preserve the island's freshwater reserves and ecological services as sea-level rise and hurricane activity intensify.

# **Table of Contents**

List of A	Abbreviations	2
Executi	ve Summary	3
1- Sec	etion (I)*	13
Hydrog	eologic controls on barrier island geomorphology: Insights from electromag	gnetic
surveys		13
2.1	Abstract	13
2.2	Introduction	14
2.3	Study area	15
2.4	Methods	18
Fre	equency-domain electromagnetic (FDEM):	18
DE	M:	20
2.5	Results	20
2.6	Discussion	23
2.7	Conclusion	29
	ences	
	etion (II)*	
Geologi	cal and Anthropogenic Controls on Freshwater Lens Variability in Barrier	<b>Islands:</b>
Insights	from Integrated Geophysical and Hydrogeological Surveys	46
2.1	Abstract	46
2.2	Introduction	47
2.3	Study Area	51
2.4	Data and Methods	55
2.4	.1 Time-domain Electromagnetic (TDEM) Geophysical Survey	55
2.4	.2 Hydrogeological Survey	62
2.4	.3 Topographical Survey	62
2.5	Results	64
2.5	.1 TDEM Data Inversion	64
2.5	.2 Spatial Variability in Subsurface Conditions and Surface Topograph	y in
Cr	oss-shore and Along-shore Directions	
2.5	.3 Statistical Analysis of Subsurface and Topographic Conditions	78
2.6	Discussion	82
3.1	Uncertainty Analysis	82
3.2	Morphology and Distribution of the FWL	83
3.3	Broader Implications and Challenges	87
2.7	Conclusions	89
2.8	Supplementary Material:	91
Refer	ences	103
3- Sec	etion (III)	119
	ted Geophysical-Geospatial Analysis of Breach-Prone Zones on Northern P	
Island		119
3.1	Elevation-Based Vulnerability Framework	120
3.2	Composite Elevation-Conductivity Screening for Breach Susceptibility	
3.2		
3.2	.2 Subsurface Salinity Proxy: Frequency-Domain EM Conductivity	122

3.2.3	Spatial Patterns and Management Hotspots	123
3.3	Subsurface Controls on Breach Susceptibility	127

# **List of Figures**

Figure 1-1 a) Location map showing Padre Island, the study area, and the locations of FDEM
profiles b) LiDAR-derived DEM illustrating the diverse topographic variations across the study
area c) A typical barrier island profile demonstrates the various characteristics that can be
observed from the gulf-side to the Lagoon shoreline
Figure 1-2 Field image and schematic representation of the Geonics EM-31 system
configuration, illustrating the operational methodology for acquiring apparent conductivity
measurements along profiles
Figure 1-3 (a) Spatial variations in the apparent conductivity across Padre Island. Also shown
are the spatial variability in apparent conductivity with (b and c) human development, (c and d)
depth to water table, and (c) vegetation cover.
Figure 1-4 Spatial variations in apparent conductivity and elevation across Padre Island. The
four distinct zones are shown with light colors (Zone I: blue; Zone II: yellow; Zone III: tan; Zone
IV: green). Profile locations are shown in Figure 1a
Figure 2-1 (a) Location map of the study area on Padre Island, including developed and
undeveloped zones. The inset shows Padre Island's location, off the coast of southern Texas,
USA. (b) High-resolution (1-m) DEM of the study area shows the elevation of the study area, in
meters above sea level. (c) Padre Island general cross-section, illustrating the island's diverse
geomorphological features (modified from Brown et al. 1977)

Figure 2-2 Fieldwork on Padre Island: (a) Geonics G-TEM system setup for TDEM data
acquisition, showing the Slingram configuration. The square $10\text{-m} \times 10\text{-m}$ TX loop and the $0.6\text{-m}$
m-diameter RX coil are positioned 15 m away from the TX loop's center. (b) Water sample
collection and field analysis. (c) Location and elevation measurements using the Trimble R8
Global Navigation Satellite System (GNSS) receiver. 58
Figure 2-3 Locations of TDEM sounding stations, 2D resistivity profiles derived from the
inverted data, and collected water samples. Sounding names include both profile number and
station/sounding identifiers (e.g., PV11TEM12 means profile 11, sounding 12)
Figure 2-4 Inversion results for four representative TDEM soundings from distinct geographical
settings across Padre Island: (a) near a well with recorded lithology, (b) at the beach, (c) at the
island center and near a well with recorded lithology, and (d) near LM. The left side of each
panel shows the TDEM-measured data. The center of each panel displays the best-fit model (red
continuous line) alongside equivalent model solutions (dashed dark green lines). The right side
of each panel contains the inversion results and the interpretation of a three-layer model for the
sounding station. 66
Figure 2-5 (a) Elevation, (b) resistivity profile, and (c) salinity for profile PV11. In panel b, the
contour lines at 8 and 1 $\Omega$ .m delineate the approximate depths to the saltwater interface and the
top of the Pleistocene clay layer, respectively.
Figure 2-6 (a) Elevation, (b) resistivity profile, and (c) salinity for profile PV12. In panel b, the
contour lines at 8 and 1 $\Omega$ .m delineate the approximate depths to the saltwater interface and the
top of the Pleistocene clay layer, respectively.

Figure 2-7 (a) Elevation, (b) resistivity profile, and (c) salinity for profile PV13. In panel b, the
contour lines at 8 and 1 $\Omega$ .m delineate the approximate depths to the saltwater interface and the
top of the Pleistocene clay layer, respectively
Figure 2-8 (a) Elevation and (b) resistivity profile PV3. In panel b, the contour lines at 8 and 1
$\Omega$ .m delineate the approximate depths to the saltwater interface and the top of the Pleistocene
clay layer, respectively
Figure 2-9 (a) Elevation and (b) resistivity profile PV4. In panel b, the contour lines at 8 and 1
$\Omega$ .m delineate the approximate depths to the saltwater interface and the top of the Pleistocene
clay layer, respectively
Figure 2-10 (a) Elevation and (b) resistivity profile P2–P2'. In panel b, the contour lines at 8 and
1 $\Omega$ .m delineate the approximate depths to the saltwater interface and the top of the Pleistocene
clay layer, respectively
Figure 2-11 Spatial variability in the hydrogeological properties of Padre Island: (a) resistivity
of FWL, (b) thickness of FWL, (c) thickness of brackish/saline water, and (d) depth to the
Pleistocene clay layer
Figure 2-12. Geomorphological zones of Padre Island along with subsurface and surface
conditions: (a) average resistivity and thickness of FWL, dune volume, and depth to the clay
layer. Error bars represent the standard deviation in each parameter. (b) Correlation coefficients
between the FWL resistivity and elevation, dune volume, and clay layer depth. (c) Correlation
coefficients between the FWL thickness and elevation, dune volume, and clay layer depth. Zone
1 is the beach, Zone 2 is the foredune, Zone 3 is the vegetated barrier flats, and Zone 4 is the
back dune and wind tidal flats. 52

Figure 3- 1 Elevation-based vulnerability map of northern Padre Island. Colored polygons delineate four elevation bands derived from 1-m USGS LiDAR (NAVD88): Class I (0-1 m, red), Class II (1–3 m, orange), Class III (3–5 m, yellow), and Class IV (> 5 m, gray). Warmer colors indicate progressively higher susceptibility to daily tidal flooding, storm-surge overtopping, and barrier-island breaching, as summarized in Table 3-1. Gray hatching marks developed areas.. 125 Figure 3-2 Composite breach-susceptibility map integrating dune-ridge elevation and subsurface electrical conductivity. Panel (a) is the entire study area. Panels (a, c, and d) progress from north to south along northern Padre Island. Hollow black polygons outline the dune-core corridor where ground elevation is ≥ 3 m NAVD88 (Classes III–IV; interior shading: yellow = Class III, gray = Class IV). Superimposed circles plot FDEM apparent conductivity, colourcoded by salinity proxy: blue (195–272 mS m<sup>-1</sup>), green (272–300 mS m<sup>-1</sup>), and pink (> 300 mS m<sup>-1</sup>). Narrow Class I–II ridges overlain by pink, high-conductivity points mark the island's highest composite risk—locations with shallow saline groundwater, thin dunes, and a documented history of overwash (e.g., panel a, north of Packery Channel). Conversely, wide Class IV ridges with blue conductivity denote the island's most resilient backbone (e.g., panel d). This dual-layer visualization guides managers to prioritize dune nourishment, setback Figure 3-3 Fresh-water-lens resistivity map derived from TDEM soundings. Cool colours (≥ 15  $\Omega$  m) indicate fresh-brackish groundwater; warm colours (< 15  $\Omega$  m) reveal shallow saline intrusion and frequent tidal saturation. Red circles mark the most saline, breach-prone corridors. 

Figure 3-4 Thickness of the fresh-water lens. Blues and greens (≥ 8 m) correspond to a robust lens beneath wide, high dunes, whereas reds and yellows (< 8 m) flag areas where the lens has

nearly pinched out—zones prone to rapid salinization, overwash, and eventual breaching.
Critical thinning sectors are circled in red
Figure 3-5 Depth to the Pleistocene clay layer. Deep clay (> 18 m, blue) provides a substantial
sandy buffer; shallow clay (< 8 m, red) means only a thin, easily erodible sand veneer overlies
the island's clay floor, elevating scour and breach risk. Red circles highlight the shallowest, most
vulnerable pocket
Figure S 1 TDEM method's operating principle. (a) Transmitter (T <sub>x</sub> ) current I(t) gradually rises
to a steady state (Io) before abruptly shutting off. (b) Induced electromotive force voltage V(t)
proportional to the change rate of the primary magnetic field. (c) Decay of the secondary
magnetic field BS(t) caused by dissipating eddy currents in the subsurface (adopted from Everett
2013)
Figure S 2 Core description illustrating the lithology and age of subsurface layers from the North
Padre Island Core EE, collected by Garrison (1986) at Crane Island on the bay side of Padre
Island (adapted from (Garrison & McCoy, 2007))
Figure S 3 Statistical analysis of the equivalent models for the three subsurface layers,
displaying the average resistivity and thickness/depth of each layer, with standard deviation as an
error bar to represent the uncertainty in subsurface properties: a) FWL, b) Salt/Brackish Water
Laver. c) Clay Laver. 96

# **List of Tables**

Table 1- 1 Measurement statistics by zone. Conductivity and elevation values were reported by
$mean \pm STD \dots 25$
Table 1-2 Measurement statistics by profile, subdivided into zones. Measurements for the
undeveloped area PV8 are shown in bold
Table 3-1 Elevation-based vulnerability classes for northern Padre Island. This table groups
island terrain into four elevation bands (NAVD88) and summarizes, for each band, the typical
hydrodynamic forcing required to cause flooding or breaching, the expected recurrence interval
based on regional hurricane climatology, and key management implications (e.g., permitting
restrictions, dune-nourishment priorities). Higher classes (III-IV) correspond to wider, higher
dune ridges that offer robust protection, whereas Classes I-II identify low-lying corridors
exposed to daily tidal inundation or frequent storm-surge overtopping
Table S 1 Coordinates, elevation, and water sample collection details for TDEM stations (cells
with an ✓ checkmark represents locations where samples were collected, while cells with an ×
checkmark indicates where no samples were collected.)
Table S 2 Resistivity and thickness of subsurface layers, along with station elevation statistics of
all the TDEM stations. 101
Table S 3 Resistivity and thickness of subsurface layers, along with station elevation and dune
volume statistics for stations in various zones across the island

## 1- Section (I)\*

# Hydrogeologic controls on barrier island geomorphology: Insights from electromagnetic surveys

(\*) The following content was partially included in the published manuscript: Abdelrehim, R., Ahmed, M., Everett, M.E., 2023. Hydrogeologic controls on barrier island geomorphology: Insights from electromagnetic surveys. Lead. Edge 42, 608–614. https://doi.org/10.1190/tle42090608.1.

#### 2.1 Abstract

Barrier islands provide a first line of defense for coastal communities against storms, hurricanes, and sea-level rise. The geomorphology of barrier islands exerts a major control on storm impacts and island recovery. In turn, the barrier islands' geomorphology is affected by the subsurface hydrogeological conditions. In this study, we investigated an important relationship between the subsurface hydrogeological conditions and the geomorphology of Padre Island on the Texas Gulf Coast with a focus on the influence of human development. We measured apparent electrical conductivities using frequency-domain electromagnetic (FDEM) surveys and spatially correlated them with the island's morphology, the latter generated from a 1-m resolution digital elevation model (DEM). Four distinct zones were identified from the observed variations in apparent conductivity and elevation, revealing their inverse correlation. The beach area (Zone I) exhibits the highest apparent conductivity (289.7  $\pm$  66.3 mS/m) and the lowest elevations (1.4  $\pm$  0.2 m). These trends are largely due to the proximity of the beach to saline groundwater and maritime floods. Conversely, the foredune area (Zone II) presents the lowest apparent conductivity (19.0  $\pm$  3.4 mS/m) and the highest elevation (4.5  $\pm$  0.4 m), owing to its greater

distance from the saline waters, deeper groundwater levels, and relatively dry soil conditions. Human development has significantly impacted Zones III (east central zone) and IV (west central zone), contributing to an increase in apparent conductivity (Zones III:  $40.3 \pm 21.8$  mS/m, Zones IV:  $159.5 \pm 83.0$  mS/m) and a reduction in elevation (Zones III:  $2.1 \pm 0.5$  m, Zones IV:  $1.3 \pm 0.4$ ). Anthropogenic activities have modified hydrological patterns, introduced conductive materials, and altered vegetation cover and soil composition. This research elucidates the interplay between subsurface electrical conductivity, surface morphology, and the impact of human development on barrier island geomorphology, providing crucial insights for coastal management and conservation efforts.

## 2.2 Introduction

Approximately 600 million individuals, roughly 10% of the global population, reside in coastal regions that are less than 10 m above sea level. Population growth, urbanization, and coastal migration are all projected to increase (Baztan et al., 2015; Nicholls et al., 2007) Coastal communities are confronted with unique challenges compared to their inland counterparts, including heightened risks associated with hazards such as high-tide flooding, hurricanes, tsunamis, and sea level rise. These challenges to sustainability are expected to be complicated by ongoing climatic and anthropogenic forcings (NOAA, 2023).

Barrier islands provide a first line of defense for coastal communities against the aforementioned maritime hazards (Ruggiero et al., 2018; NOAA, 2021). Barrier island geomorphology plays a crucial role in determining the response of these systems to extreme events (Wernette et al., 2018). For example, the island's width and elevation exert a major control on its ability to absorb storm surges (Houser et al., 2018, 2008). The height, width, and vegetation cover of dunes helps shape the impact of extreme events by dissipating wave energy

and mitigating inland flooding (Houser and Hamilton, 2009; Nott, 2006; Sallenger Jr, 2000). The availability of sediments beneath the island and its near-shore environment also influences recovery from extreme events (Houser and Hamilton, 2009; Leatherman, 1976).

The geomorphology of barrier islands results from complex, scale-dependent interactions over wide ranges of time and space. Factors affecting an island's geomorphology include antecedent geologic structures and processes, sea-level changes, wave and current dynamics, sediment supply, vegetation cover, and human activities (Cooper et al., 2012; Wernette et al., 2018). We are interested in probing how subsurface hydrogeological conditions and human development contribute to the geomorphology of barrier islands. Padre Island, a major barrier system off the Texas Gulf Coast, was selected as a convenient, representative test site (Figure 1-1).

## 2.3 Study area

Padre Island, located on the Texas Gulf Coast, is the world's longest barrier island at 182 km in length. Roughly 3 km wide, it stretches from the city of Corpus Christi in the north to the resort community of South Padre Island in the south (Pendleton et al., 2004). The island is oriented N-S, bordered by the Gulf of Mexico on the east and hypersaline Laguna Madre on the west (Figure 1-1). The southern and central part of Padre Island are preserved as Padre Island National Seashore (length ~108 km) and a portion of the lower island (South Padre Island) is protected as part of the Laguna Atascosa National Wildlife Refuge (length ~56 km). The study area of this research spans the northernmost 20 km of the island, comprising both developed and "protected" undeveloped stretches (Figure 1-1).

Padre Island's origin and geologic history have been discussed in detail elsewhere (Brown et al., 1977; Garrison et al., 2010; Houser et al., 2018; Wernette et al., 2018). Briefly, during interglacial stages of the Pleistocene, inland rivers and streams discharged to a network of deltas along the Gulf Coast shoreline. Headwater tributaries of entrenched valley systems deeply eroded the Pleistocene ravinement surfaces. Pleistocene river deposits now underlie the modern wind-tidal flats. As sea levels rose during the Holocene and flooded the preexisting stream valleys, some of them became bays and estuaries. Once sea levels stabilized, sand shoals and offshore bars between the drowned river valleys began to merge. In the late Holocene, the shoals emerged from the sea to become a series of low, discontinuous sandy islands aligned parallel to the mainland shoreline.

Stratigraphically, the base of the barrier-lagoon system consists of Pleistocene sand and mud overlain by shoreface sand and mud, washover and aeolian deposits, and lagoonal muds (Brown et al., 1977; Houser et al., 2018). The depth to the Pleistocene ravinement surface (in this case, the top of the Beaumont formation) varies considerably along the length of the island. The thickness of modern deposits of shoreface sands is estimated to be 2–3 m, whereas the thickness of older shoreface sands and muds can be ~10 m or greater within the paleochannels (Garrison et al., 2010). A topographical analysis shows that Padre Island exhibits a range of elevations extending from zero up to ~16 m above mean sea level. Despite the wide range, the mean elevation of the island is relatively low, averaging only ~0.38 m. The study area ranges in elevation from zero to 13.3 m, averaging 1.8 m (Figure 1-1b). Figure 1c presents a generalized cross-section of Padre Island, delineating the diverse features that span from the Gulf of Mexico to the Laguna Madre, along with the distinct morphological zones identified in this study.

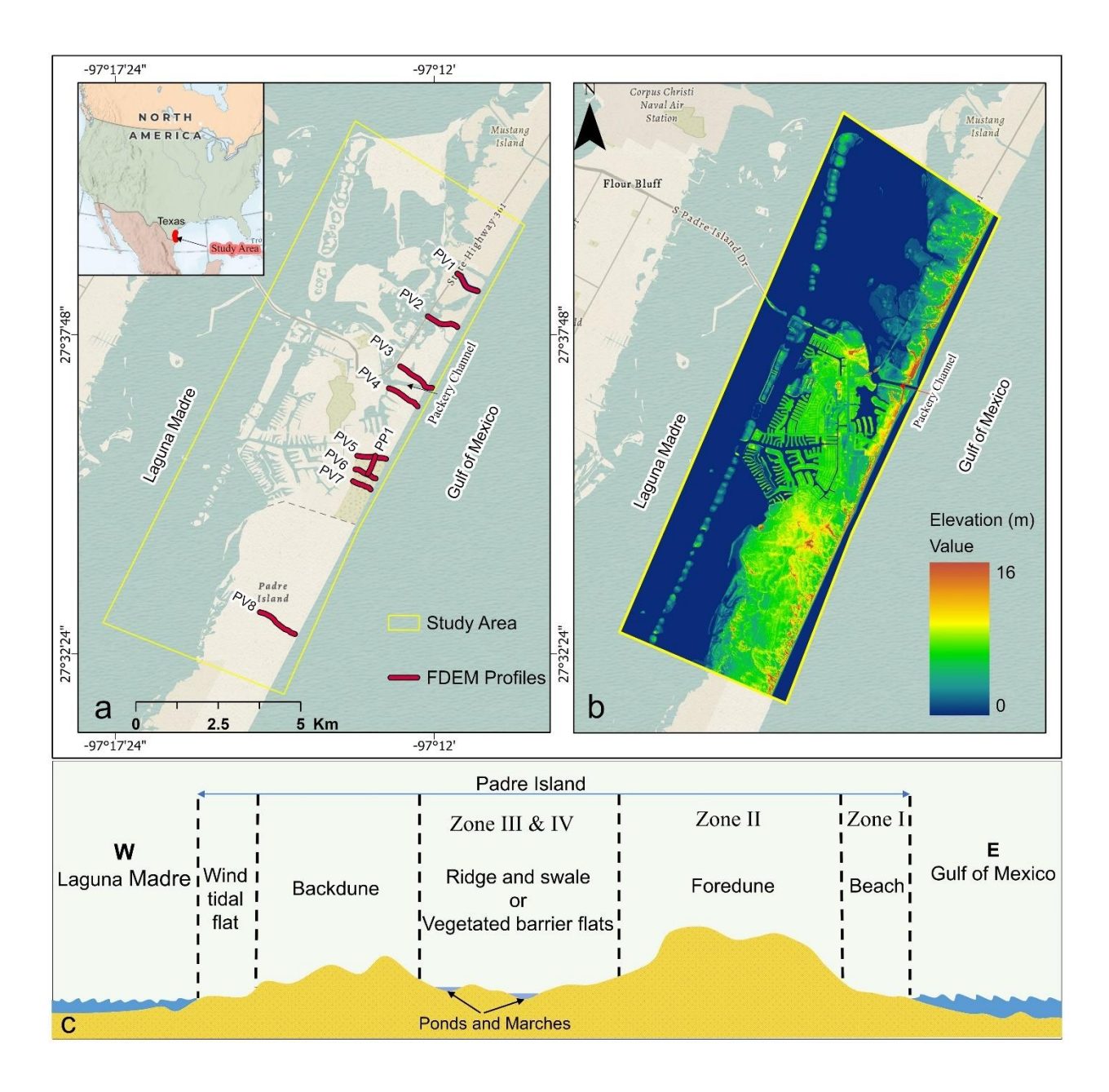


Figure 1- 1. (a) Location map showing Padre Island, the study area, and the locations of FDEM profiles; (b) LiDAR-derived DEM illustrating the diverse topographic variations across the study area; (c) A typical barrier island profile demonstrates the various characteristics that can be observed from the gulf-side to the Lagoon shoreline (Abdelrehim et al., 2023).

#### 2.4 Methods

In this study, surface and subsurface datasets were collected to investigate how subsurface hydrogeologic conditions control the geomorphology of Padre Island. The research focused on understanding the relationship between subsurface electrical conductivity, determined using frequency-domain electromagnetic (FDEM) techniques, and the island's geomorphology. A 1 m-resolution digital elevation model (DEM) was used to extract the island's geomorphological features. Hydrogeological conditions were inferred from the electromagnetic measurements, as described below. Correlations were then established between the hydrogeological conditions and the island's surface morphology, considering both developed and undeveloped areas. The correlations provide insight into mechanistic connections between surface characteristics and subsurface structures, as well as hydrological processes.

## Frequency-domain electromagnetic (FDEM):

The terrain conductivity meter is a noninvasive geophysical instrument that operates on the principles of electromagnetic induction. Meter readings record lateral variations in apparent electrical conductivity as the instrument is moved along a profile. Apparent conductivity, in turn, is a measure of bulk electrical conductivity averaged over the instrument footprint. More precisely, apparent conductivity at a given location is simply the electrical conductivity of a hypothetical homogeneous half space that would generate the observed meter reading at that location. This technique, also known as the frequency-domain electromagnetic (FDEM) method, has become a popular tool for near-surface geophysical applications because the one-person portable terrain meters can cover large areas in a short period of time and are inexpensive compared to many other geophysical techniques (Aly et al., 2018; Everett, 2013; McNeill, 1980).

FDEM surveys were conducted using the Geonics Ltd. EM-31 instrument along the 9 profiles shown in Figure 1-1a. These profiles were oriented perpendicular and parallel to the shoreline. One of the profiles (PV8) is situated in a pristine, undeveloped area. The remaining profiles are located within developed regions of Padre Island (Figure 1-1a).

The EM-31 instrument (Geonics Limited, 1995) (Figure 1-2) provides a rapid qualitative means to map apparent conductivity in coastal environments. The EM-31 is robust, efficient, and easy to operate. A time-varying magnetic field is generated by the transmitter coil, which penetrates the conductive ground and, according to Faraday's law, induces eddy currents to flow in the subsurface. The induced currents, in turn, generate a secondary magnetic field that is detected by the receiver coil and registered as a voltage. A simple formula converts the received voltage to apparent conductivity (McNeill 1980). The EM-31 device operates at a fixed frequency of 9.8 kHz and a fixed 3.66 m offset between the transmitter and receiver coils. The depth of investigation is ~6 m, depending on the subsurface conductivity (McNeill, 1980; Reid and Howlett, 2001).

Very high-resolution terrain conductivity data were collected in this study. An average of 11 measurements were collected per profile meter in continuous acquisition mode. The nine profiles were 582 to 1234 m (Figure 1-1a). A thorough quality control was implemented to ensure the reliability and validity of the measurements. Non-positive apparent conductivity readings, herein attributed to interference from nearby man-made structures, were identified within the dataset. These readings are presumed to be non-representative of the naturally varying subsurface conditions and hence were systematically excluded from subsequent data analyses. This rigorous data cleansing approach enhances the robustness of our interpretations by reducing the impact of potential anthropogenic signals.

## **DEM:**

High-resolution (1 m) DEM data were used in this study to extract the island's geomorphology. This product was collected in 2018 through the U.S. Geological Survey 3D Elevation Program (3DEP) using light detection and ranging (LiDAR) technology (USGS, 2020). The 1-m DEM is the highest resolution offered in the 3DEP product suite. The DEM (vertical accuracy  $\pm 0.53$  m) represents the topographic bare-earth surface, excluding features such as buildings and vegetation (USGS, 2022).

#### 2.5 Results

On Padre Island, four distinct zones were identified by breakpoints in the apparent conductivity and elevation profiles (Figures 1-3, 1-4). Generally, elevation exhibited an inverse correlation with terrain conductivity (correlation coefficient: -0.69). Measurement statistics by zone are given in Table 1. Zone I, the beach, extends from the shoreline to the base of the foredune, with a highly variable length averaging 41.7 m. This zone displays a low elevation and the highest apparent conductivity of the four zones. Zone II, which has an average length of 221 m, encompasses the foredune and exhibits the highest elevation and the lowest apparent conductivity. Extending beyond the foredune to the central parts of the island, characterized by ridges and swales, Zone III has an average length of 335 m. The apparent conductivity and elevation in this zone are intermediate. Zone IV extends further into the central parts of the island with an average length of 286 m. This zone shares a similar elevation to Zone I but exhibits lower apparent conductivity.

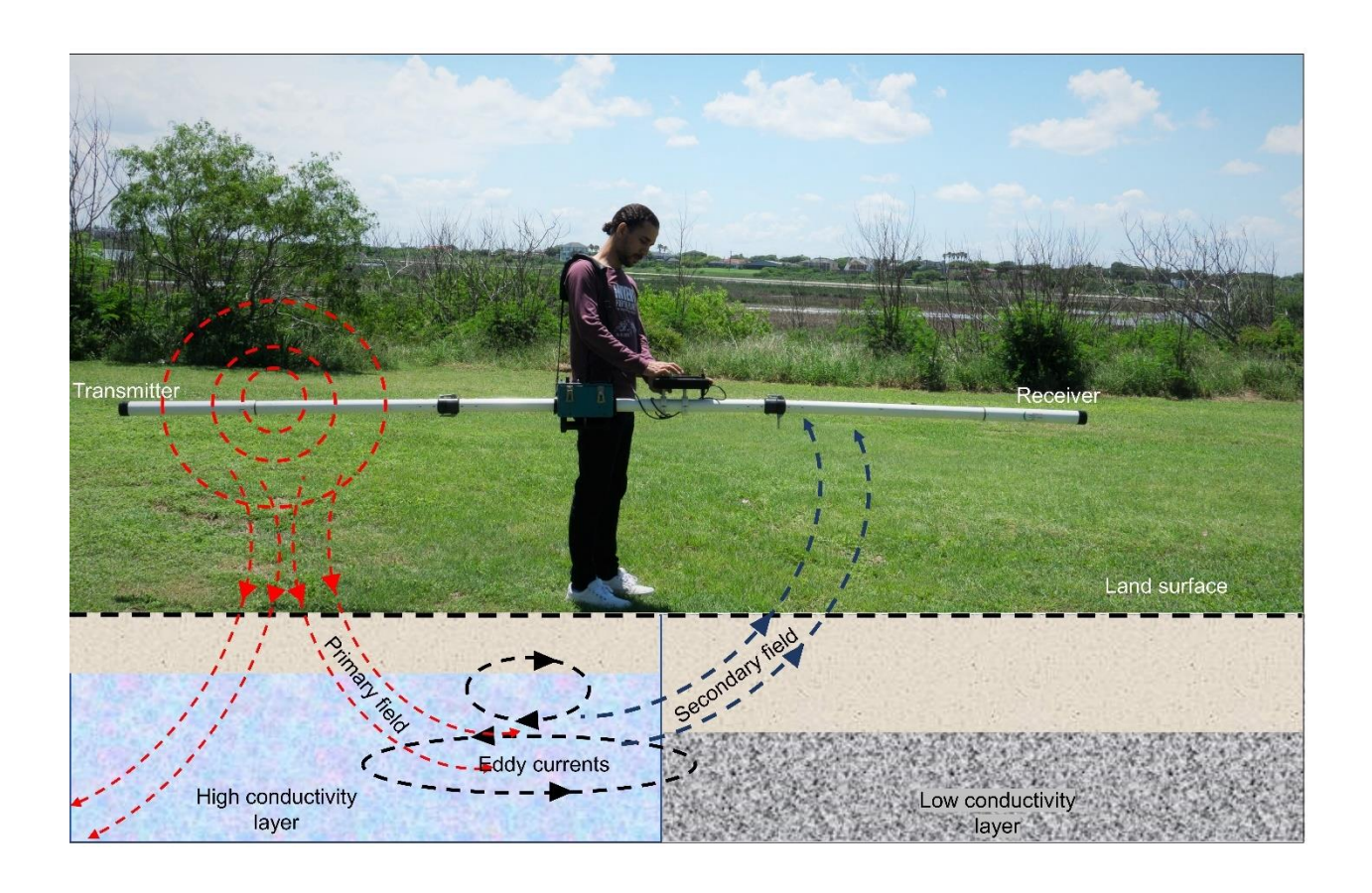


Figure 1- 2. Field image and schematic representation of the Geonics EM-31 system configuration, illustrating the operational methodology for acquiring apparent conductivity measurements along profiles (Abdelrehim et al., 2023).

Apparent conductivity and, to a lesser extent, elevation within the identified zones exhibit significant spatial variability (Figure 1-4). The measurement statistics by profile (average conductivity and average elevation), subdivided into zones, appear in Table 2. On the pristine, undeveloped areas of Padre Island (profile PV8), Zone I exhibits a moderate apparent conductivity. Despite relatively similar elevations to those of the undeveloped areas, Zone I apparent conductivity is considerably higher in the developed areas (profiles PV5,6,7). The apparent conductivity and elevation values in Zone II are comparable across both developed (PV4,5,6,7) and undeveloped (PV8) areas. Zone III apparent conductivity in undeveloped

regions, PV8, is relatively lower than that of developed area, PV5, whereas the opposite is true for elevation. The PP1 profile, operating within the scope of Zone III, maintains a direction parallel to the shoreline and stretches between the PV5 and PV6 points. Zone IV shows a significant difference in both elevation and apparent conductivity between developed and undeveloped areas. Over the undeveloped area PV8, Zone IV, apparent conductivity is low while elevation is high. Over the developed regions (PV2, 3, 4, 5), the converse is true.



Figure 1- 3. (a) Island-wide distribution of apparent electrical conductivity across Padre Island. Panels (b), (c), and (d) relate those conductivity values to three surface variables: (b) the intensity of human development, (c) depth to the water table, and (d) vegetation cover (Abdelrehim et al., 2023).

#### 2.6 Discussion

The beach area (Zone I) exhibits the highest apparent conductivity compared to the other zones. The beach is in closest proximity to the saline waters of the Gulf of Mexico which must play a significant role via enhancing the conductivity of groundwater underlying the shoreface. Zone I is also more prone to frequent maritime flooding caused by high tides and storm surges. The relatively frequent intrusion of saline water, infiltrating into the subsurface, should further enhance the apparent conductivity of Zone I. The continuous and repetitive back-and-forth movement of waves tends to level the beach area over time, resulting in the observed lower elevations.

The foredune area (Zone II) comprises the lowest apparent conductivity and the highest elevation among the identified zones. The combination of higher elevation, deeper groundwater level, infrequent occurrences of maritime flooding, infiltration of fresh precipitation, and presence of relatively dry soil collectively contributes to low electrical conductivity in this zone. As elevation increases, the near-surface is less susceptible to direct contact with saline water. Moreover, the relatively greater distance from the shoreline results in reduced exposure to salts and other minerals that would increase subsurface electrical conductivity. In areas where the groundwater table is relatively deep, the dune environment becomes more conducive to the growth of freshwater-dependent plant species that are adapted to soils with limited exposure to saline water. Their presence and growth contribute to the stabilization of the dune system. As these plants establish themselves, their root systems help bind the soil, preventing erosion and maintaining a high dune elevation. As rainfall occurs, fresh water infiltrates the soil, diluting the concentration of salts and minerals, leading to a decrease in electrical conductivity in the

foredune area. Finally, the relatively dry foredune conditions act as a barrier to the movement of electrical current, contributing to the observed lower apparent conductivity measurements.

Significant portions of Zones III and IV on Padre Island are affected by human development. Anthropogenic activity can modify natural hydrological processes, introduce new sources of high conductivity such as metal infrastructure, influence vegetation dynamics, and alter the composition of the soils and their fluid content and chemistry. For example, constructing waterway systems and housing development can disrupt groundwater flow patterns. The dredging of canals (e.g., Packery channel and housing development canals; Figure 1-1) can have significant consequences. By reducing the distance that groundwater must travel to its point of discharge to the sea, the construction of canals leads to lowered water table levels and, subsequently, increased conductivity in the surrounding areas. For example, areas near Packery channel and housing development canals on PV3, PV4, and PV5 exhibit higher conductivity values within zones III (44 to 95 mS/m) and IV (200 to 297 mS/m) (Figures 1-3b, 3c) in contrast to areas located farther away from them (24 to 29 mS/m) (Figure 1-3d). Additionally, the use of impervious materials in development reduces the recharge rate of water into the soil, increases runoff, and can create evaporation ponds with high salt and mineral contents. In Figures 1-3b and 3c, it can be observed that areas in close proximity to these ponds display elevated conductivity values ranging from 95 to 230 mS/m within zones III and IV. Conversely, areas situated far from the ponds exhibit lower conductivity values ranging from 24 to 29 mS/m. A shallower water table can weaken the dune's structure, lower its height, and make it more susceptible to erosion by storm events. If the water table is shallow, vegetation growth is impeded, further destabilizing the dune. Regions with shallower water table exhibit higher conductivity values (95 to 230 mS/m) within zones III and IV in contrast to areas located farther away from them (24 to 28

mS/m) (Figures 1-3c and 1-3d). Human development also introduces various conductive materials and substances into the environment, such as metal, wiring, fertilizers, and industrial waste. These additions alter the composition of the soil, generally increasing its apparent conductivity. Moreover, changes in vegetation cover caused by human development can have significant implications. Vegetation is crucial in regulating water balance, evapotranspiration rates, and nutrient dynamics. When natural vegetation is removed or altered, deeper infiltration can occur, potentially leading to increased electrical conductivity in the soil and groundwater. Areas with minimal vegetation cover exhibit higher conductivity values (250 to 380 mS/m) within zones III and IV, in contrast to regions with intense vegetation (15 to 25 mS/m) (Figure 1-3c).

Table 1- 1. Measurement statistics by zone. Conductivity and elevation values were reported by  $mean \pm STD$ 

Zone	Apparent conductivity [mS/m]	Elevation [m]
I (Beach Area)	289.7 ± 66.3 (highest)	$1.4 \pm 0.3$
II (Foredune area )	$19.0 \pm 3.4 \text{ (lowest)}$	$4.5 \pm 0.4$ (highest)
III (East central zone)	$40.3 \pm 21.8$	$2.1 \pm 0.5$
IV (West central zone)	159.5 ± 83.0	$1.3 \pm 0.4$ (lowest)

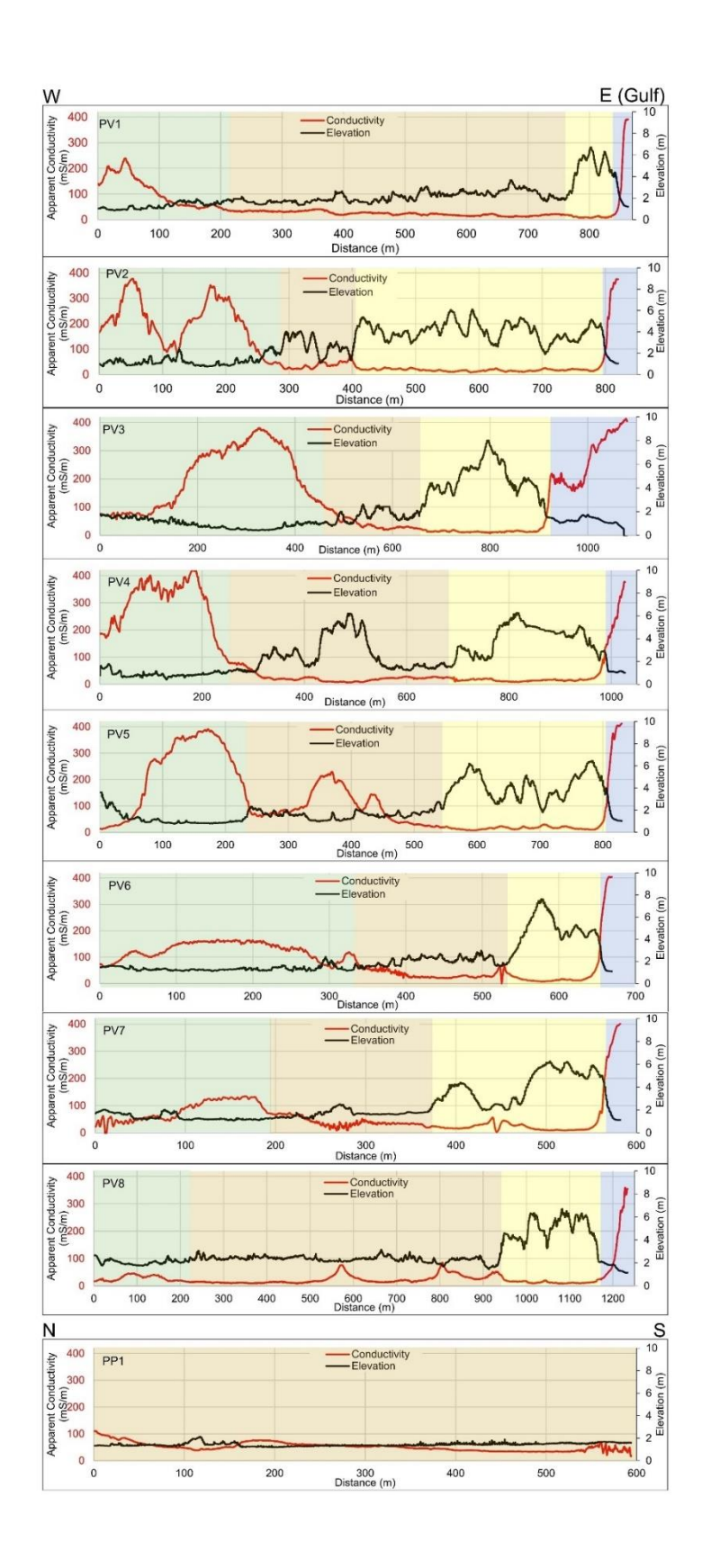


Figure 1- 4. Spatial variations in apparent conductivity and elevation across Padre Island. The four distinct zones are shown with light colors (Zone I: blue; Zone II: yellow; Zone III: tan; Zone IV: green). Profile locations are shown in Figure 1-1a.

Table 1-2. Measurement statistics by profile, subdivided into zones. Measurements for the undeveloped area PV8 are shown in bold

Zon	Profile	Apparent conductivity [mS/m]	Elevation [m]
e I	PV1	$293.1 \pm 106.8$	$1.5 \pm 0.2$
1	PV2	$285.1 \pm 100.8$ $285.1 \pm 95.5$	$1.3 \pm 0.2$ $1.4 \pm 0.3$
	PV3	$272.3 \pm 87.3$	$1.4 \pm 0.3$ $1.2 \pm 0.4$
	PV4	$272.3 \pm 87.3$ $254.7 \pm 70.2$	$1.2 \pm 0.4$ $1.1 \pm 0.1$
	PV5	$382.0 \pm 28.2$	$1.1 \pm 0.1$ $1.2 \pm 0.1$
	PV6	$337.0 \pm 73.5$	$1.2 \pm 0.1$ $1.6 \pm 0.7$
	PV7	$344.6 \pm 44.9$	$1.6 \pm 0.7$ $1.6 \pm 0.5$
	PV8	148.8 ± 115.1	$1.6 \pm 0.3$
II	PV1	$14.6 \pm 13.4$	$5.0 \pm 1.0$
11	PV2	$14.0 \pm 13.4$ $18.2 \pm 6.7$	$4.1 \pm 0.8$
	PV3	$19.2 \pm 26.5$	$4.6 \pm 1.5$
	PV4	$18.8 \pm 18.3$	$4.1 \pm 1.2$
	PV5	$22.5 \pm 34.2$	$4.1 \pm 1.1$
	PV6	$18.5 \pm 16.2$	$5.0 \pm 1.2$
	PV7	$25.4 \pm 28.5$	$4.1 \pm 1.4$
	PV8	$14.8 \pm 6.2$	4.9 ± 1.1
III	PV1	$23.9 \pm 7.7$	$2.1 \pm 0.5$
	PV2	$36.6 \pm 13.1$	$2.9 \pm 0.9$
	PV3	$43.8 \pm 23.7$	$1.6 \pm 0.5$
	PV4	$25.1 \pm 17.5$	$2.5 \pm 1.4$
	PV5	$94.8 \pm 58.7$	$1.6 \pm 0.4$
	PV6	$34.3 \pm 13.1$	$2.1 \pm 0.4$
	PV7	$39.9 \pm 16.2$	$1.7 \pm 0.3$
	PV8	$23.8 \pm 15.8$	$2.3 \pm 0.2$
	PP1	$52.8 \pm 15.8$	$1.4 \pm 0.1$
IV	PV1	$107.4 \pm 60.9$	$1.3 \pm 0.3$
	PV2	$199.6 \pm 95.5$	$1.3 \pm 0.5$
	PV3	$206.8 \pm 109.7$	$1.0 \pm 0.4$
	PV4	$297.2 \pm 90.4$	$0.9 \pm 0.2$
	PV5	$230.6 \pm 134.3$	$1.2 \pm 0.6$
	PV6	$124.1 \pm 32.3$	$1.3 \pm 0.2$
	PV7	$81.4 \pm 37.1$	$1.4 \pm 0.3$
	PV8	$28.6 \pm 9.8$	$2.1 \pm 0.2$

#### 2.7 Conclusion

Barrier islands are critical defenses against natural hazards for coastal communities worldwide, and their importance is expected to rise due to anticipated population growth, urbanization, and sea level rise. This research uses electromagnetic geophysical measurements to probe the complex links between subsurface hydrogeological conditions and barrier island geomorphology, through a comprehensive case study at Padre Island in Texas. Four distinct zones were identified, each marked by distinct levels of conductivity and elevation. The beach area shows high conductivity and low elevations due to its proximity to saline groundwater and maritime floods. The foredune area, on the other hand, demonstrates the lowest conductivity and highest elevation, attributed to its greater distance from saline waters, deeper groundwater levels, and relatively dry soil conditions. The study also reveals the significant impact of human development on the island, as evident in the changes in conductivity and elevation in the east and west central zones.

The findings emphasize the significant role of anthropogenic factors in substantially altering surface and subsurface conditions and subsequently impacting island morphology. The findings also suggest that understanding the interactions between surface and subsurface conditions can help guide sustainable development practices, ensuring the resilience of the coastal environment. Future research is needed to further refine our understanding of the interactions between subsurface conditions, surface morphology, and human activities across different geologic settings and scales. By doing so, we can better predict the behavior of barrier islands in the face of a changing climate and anthropogenic pressures, informing effective management and conservation strategies to safeguard our coastal communities.

#### References

- Abdelrehim, R., Ahmed, M., Everett, M.E., 2023. Hydrogeologic controls on barrier island geomorphology: Insights from electromagnetic surveys. Lead. Edge 42, 608–614. https://doi.org/10.1190/tle42090608.1
- Abouelmagd, R.G., Barseem, M.S.M., Metwally, S.E.M., Farag, M.S.M., Mousa, S.E.A., 2020.

  Groundwater Exploration in Fractured Rocks Using Transient Electromagnetic Technique (
  TEM), West El-Minia, Egypt. Egypt. Geophys. Soc. 18, 145–154.
- Adeoti, L., Alile, O.M., Uchegbulam, O., 2010. Geophysical investigation of saline water intrusion into freshwater aquifers: A case study of Oniru, Lagos state. Sci. Res. Essays 5, 248–259.
- Al-Garni, M.A., El-Kaliouby, H.M., 2011. Delineation of saline groundwater and sea water intrusion zones using transient electromagnetic (TEM) method, Wadi Thuwal area, Saudi Arabia. Arab. J. Geosci. 4, 655–668. https://doi.org/10.1007/s12517-009-0094-5
- Aly, S.A., Farag, K.S.I., Atya, M.A., Badr, M.A.M., 2018. Use of electromagnetic–terrain conductivity and DC–resistivity profiling techniques for bedrock characterization at the 15th-of-May City extension, Cairo, Egypt. NRIAG J. Astron. Geophys. 7, 107–122. https://doi.org/10.1016/j.nrjag.2018.03.005
- Anderson, J.B., Wallace, D.J., Simms, A.R., Rodriguez, A.B., Milliken, K.T., 2014. Variable response of coastal environments of the northwestern Gulf of Mexico to sea-level rise and climate change: Implications for future change. Mar. Geol. 352, 348–366. https://doi.org/10.1016/j.margeo.2013.12.008
- Anderson, W.P., Evans, D.G., Snyder, S.W., 2000. The effects of Holocene barrier-island

- evolution on water-table elevations, Natteras Island, North Carolina, USA. Hydrogeol. J. 8, 390–404. https://doi.org/10.1007/s10040000081
- Archie, G.E., 1942. The electrical resistivity log as an aid in determining some reservoir characteristics. Trans. AIME 146.
- Ardali, A.S., Tezkan, B., Gürer, A., 2018. On the Salt Water Intrusion into the Durusu Lake,
  Istanbul: A Joint Central Loop TEM And Multi-Electrode ERT Field Survey. Pure Appl.
  Geophys. 175. https://doi.org/10.1007/s00024-018-1813-1
- Attwa, M., Günther, T., Grinat, M., Binot, F., 2011. Evaluation of DC, FDEM and IP resistivity methods for imaging perched saltwater and a shallow channel within coastal tidal flat sediments. J. Appl. Geophys. 75, 656–670. https://doi.org/10.1016/j.jappgeo.2011.09.002
- Ault, T., 2016. Island water stress. Nat. Clim. Chang. 6, 1062–1063. https://doi.org/10.1038/nclimate3171
- Babu, R., Park, N., Yoon, S., Kula, T., 2018. Sharp interface approach for regional andwell scale modeling of small island freshwater lens: Tongatapu island. Water (Switzerland) 10. https://doi.org/10.3390/w10111636
- Badan Ghyben, W., 1889. Nota in verband met de voorgenomen putboring nabij Amsterdam.

  Tijdshrift van het koninklyk Inst. van Ingenieurs 21.
- Barbier, E.B., 2015. Climate change impacts on rural poverty in low-elevation coastal zones. Estuar. Coast. Shelf Sci. 165, A1–A13. https://doi.org/10.1016/j.ecss.2015.05.035
- Barrett, B., Heinson, G., Hatch, M., Telfer, A., 2002. Geophysical methods in saline groundwater studies: Locating perched water tables and fresh-water lenses. Explor. Geophys. 33, 115–

- 121. https://doi.org/10.1071/EG02115
- Baztan, J., Chouinard, O., Jorgensen, B., Tett, P., Vanderlinden, J.P., Vasseur, L., 2015. Coastal Zones: Solutions for the 21st Century. https://doi.org/10.1016/B978-0-12-802748-6.02001-5
- Berkebile, C.A., Hay, R., 1995. Phase I Groundwater Resource Investigation at the Padre Island National Seashore.
- Brown, L.F., McGowen, J.H., Evans, T.J., Groat, C.G., Fisher, W.L., 1977. Environmental geologic atlas of the Texas coastal zone: Kingsville area, Texas, Bur. of Economic Geology, Austin, TX, U.S.A.
- Collins, W.H., Easley, D.H., 1999. Fresh-Water Lens Formation in an Unconfined Barrier-Island Aquifer. JAWRA J. Am. Water Resour. Assoc. 35, 1–22. https://doi.org/https://doi.org/10.1111/j.1752-1688.1999.tb05448.x
- Conroy, S.J., Milosch, J.L., 2011. An Estimation of the Coastal Premium for Residential Housing Prices in San Diego County. J. Real Estate Financ. Econ. 42, 211–228. https://doi.org/10.1007/s11146-009-9195-x
- Constable, S.C., Parker, R.L., Constable, C.G., 1987. Occam's inversion: a practical algorithm for generating smooth models from electromagnetic sounding data. Geophysics 52. https://doi.org/10.1190/1.1442303
- Cooper, J.A.G., Jackson, D.W.T., Dawson, A.G., Dawson, S., Bates, C.R., Ritchie, W., 2012.

  Barrier islands on bedrock: A new landform type demonstrating the role of antecedent topography on barrier form and evolution. Geology 40, 923–926.

- Costabel, S., Siemon, B., Houben, G., Günther, T., 2017. Geophysical investigation of a freshwater lens on the island of Langeoog, Germany Insights from combined HEM, TEM and MRS data. J. Appl. Geophys. 136, 231–245.

  https://doi.org/10.1016/j.jappgeo.2016.11.007
- Cozzolino, D., Greggio, N., Antonellini, M., Giambastiani, B.M.S., 2017. Natural and anthropogenic factors affecting freshwater lenses in coastal dunes of the Adriatic coast. J. Hydrol. 551, 804–818. https://doi.org/10.1016/j.jhydrol.2017.04.039
- Davis, R.A.J., 1999. The Evolving Coast, The Geographical Journal. https://doi.org/10.2307/3060522
- El-Kaliouby, H., Abdalla, O., 2015. Application of time-domain electromagnetic method in mapping saltwater intrusion of a coastal alluvial aquifer, North Oman. J. Appl. Geophys. 115, 59–64. https://doi.org/10.1016/j.jappgeo.2015.02.003
- Everett, M.E., 2013. Near-Surface Applied Geophysics. Cambridge University Press.
- Falgàs, E., Ledo, J., Marcuello, A., Queralt, P., Falgàs, E., Ledo, J., Marcuello, A., Queralt, P., 2009. Monitoring freshwater-seawater interface dynamics with audiomagnetotelluric data.
  NSGeo 7, 391–400. https://doi.org/10.3997/1873-0604.2009038
- Fetter, C.W.J., 1972. Position of the Saline Water Interface beneath Oceanic Islands. Water Resour. Res. 8, 1307–1315. https://doi.org/https://doi.org/10.1029/WR008i005p01307
- Fisher, K.R., Ewing, R.C., Tice, M., Nachon, M., Duran Vinent, O., 2021. Trends in barrier island geomorphology under continuous sea level rise: Padre Island from 1940-2020.
- Garrison, J.R., McCoy, B., 2007. The Nueces incised valley revisited: A reinterpretation of the

- sedimentology and depositional sequence stratigraphy of preserved Pleistocene and Holocene valley-fill sediments. Gulf Coast Assoc. Geol. Soc. 57, 291–304.
- Garrison, J.R., Williams, J., Miller, S.P., Weber, E.T., McMechan, G., Zeng, X., 2010. Ground-penetrating radar study of North Padre Island: implications for barrier island internal architecture, model for growth of progradational microtidal barrier islands, and Gulf of Mexico sea-level cyclicity. J. Sediment. Res. 80, 303–319.
- Geng, X., Boufadel, M.C., 2017. The influence of evaporation and rainfall on supratidal groundwater dynamics and salinity structure in a sandy beach. Water Resour. Res. 53, 6218–6238. https://doi.org/10.1111/j.1752-1688.1969.tb04897.x
- Geonics Limited, 1995. EM31-MK2 Operating Manual.
- Goldman, M.M., 1988. Transient electromagnetic inversion based on an approximate solution to the forward problem. Geophysics 53. https://doi.org/10.1190/1.1442394
- Golshan, M., Colombani, N., Mastrocicco, M., 2018. Assessing aquifer salinization with multiple techniques along the Southern Caspian Sea shore (Iran). Water (Switzerland) 10. https://doi.org/10.3390/w10040348
- Gonçalves, R., Farzamian, M., Monteiro Santos, F.A., Represas, P., Mota Gomes, A., Lobo de
   Pina, A.F., Almeida, E.P., 2017. Application of Time-Domain Electromagnetic Method in
   Investigating Saltwater Intrusion of Santiago Island (Cape Verde). Pure Appl. Geophys.
   174, 4171–4182. https://doi.org/10.1007/s00024-017-1642-7
- Grzegorzewski, A.S., Cialone, M.A., Wamsley, T. V., 2011. Interaction of barrier islands and storms: Implications for flood risk reduction in Louisiana and Mississippi. J. Coast. Res.

- 2011, 156–164. https://doi.org/10.2112/SI59-016.1
- Harris, W.H., 1967. Stratification of fresh and salt water on Barrier Islands as a result of differences in sediment permeability. Water Resour. Res. 3, 89–97.https://doi.org/10.1029/WR003i001p00089
- Heath, R.C., 1983. Basic Ground-Water Hydrology, U.S. Geological Survey Water-Supply paper 2220. https://doi.org/10.1002/job.4030160708
- Henry, H.R., 1964. Interfaces between salt water and fresh water in coastal aquifers. Geol. Surv. Water-Supply Pap. 1613–C, 70–83.
- Herzberg, A., 1901. Die wasserversorgung einiger Nordseebader. J. Gasbeleucht. Wasserversorg. 44, 815–819.
- Hill, G.W., Hunter, R.E., 1976. Interaction of biological and geological processes in the beach and nearshore environments, northern Padre Island, Texas, in: Richard A. Davis, J.,Ethington, R.L. (Eds.), Beach and Nearshore Sedimentation. Special Publications of SEPM.
- Holt, T., Greskowiak, J., Seibert, S.L., Massmann, G., 2019. Modeling the Evolution of a Freshwater Lens under Highly Dynamic Conditions on a Currently Developing Barrier Island. Geofluids 2019. https://doi.org/10.1155/2019/9484657
- Houser, C., Barrineau, P., Hammond, B., Saari, B., Rentschler, E., Trimble, S., Wernette, P., Weymer, B., Young, S., 2018. Role of the foredune in controlling barrier island response to sea level rise. Barrier Dyn. response to Chang. Clim. 175–207.
- Houser, C., Hamilton, S., 2009. Sensitivity of post-hurricane beach and dune recovery to event frequency. Earth Surf. Process. Landforms 34, 613–628.

- Houser, C., Hapke, C., Hamilton, S., 2008. Controls on coastal dune morphology, shoreline erosion and barrier island response to extreme storms. Geomorphology 100, 223–240. https://doi.org/10.1016/j.geomorph.2007.12.007
- Hunter, R.E., Dickinson, K.A., 1970. Map showing landforms and sedimentary deposits of the Padre Island portion of the South Bird Island 7.5-minute quadrangle, Texas. US Geological Survey.
- Interpex, 2008. Interpex Limited, 2008. IX1D v3 Instruction Manual, Version 1.11. Interpex Limited, Golden, Colorado.
- Ismail, M., Pradhanang, S.M., Boving, T., Motta, S., McCarron, B., Volk, A., 2024. Review of Modeling Approaches at the Freshwater and Saltwater interface in Coastal Aquifers. Land 13, 1–23. https://doi.org/10.3390/land13081332
- Jin, D., Hoagland, P., Au, D.K., Qiu, J., 2015. Shoreline change, seawalls, and coastal property values. Ocean Coast. Manag. 114, 185–193.
  https://doi.org/10.1016/j.ocecoaman.2015.06.025
- Kalisperi, D., Kouli, M., Vallianatos, F., Soupios, P., Kershaw, S., Lydakis-Simantiris, N., 2018.A Transient ElectroMagnetic (TEM) Method Survey in North-Central Coast of Crete,Greece: Evidence of Seawater Intrusion. Geosciences 8, 107.
- Kanta, A., Soupios, P., Barsukov, P., Kouli, M., Vallianatos, F., 2013. Aquifer characterization using shallow geophysics in the Keritis Basin of Western Crete, Greece. Environ. Earth Sci. 70. https://doi.org/10.1007/s12665-013-2503-z
- Kiflai, M.E., Whitman, D., 2023. Geophysical mapping of freshwater lens in Big Pine Key,

- Florida: Electromagnetic Induction Calibration and Application. Near Surf. Geophys. 21, 152–167. https://doi.org/10.1002/nsg.12244
- Kourgialas, N.N., Dokou, Z., Karatzas, G.P., Panagopoulos, G., Soupios, P., Vafidis, A., Manoutsoglou, E., Schafmeister, M., 2016. Saltwater intrusion in an irrigated agricultural area: combining density-dependent modeling and geophysical methods. Environ. Earth Sci. 75. https://doi.org/10.1007/s12665-015-4856-y
- Laignel, B., Vignudelli, S., Almar, R., Becker, M., Bentamy, A., Benveniste, J., Birol, F.,
  Frappart, F., Idier, D., Salameh, E., Passaro, M., Menende, M., Simard, M., Turki, E.I.,
  Verpoorter, C., 2023. Observation of the Coastal Areas, Estuaries and Deltas from Space.
  Surv. Geophys. 44, 1309–1356. https://doi.org/10.1007/s10712-022-09757-6
- Leatherman, S.P., 1976. Barrier island dynamics: overwash processes and eolian transport, in:

  Coastal Engineering 1976. American Society of Civil Engineers, New York, pp. 1958–
  1974.
- Ley, A., Haehnel, P., Bormann, H., 2023. Addressing the challenges of climate scenario-based impact studies in modelling groundwater recharge on small barrier islands at the German North Sea coast. J. Hydrol. Reg. Stud. 50, 101578.
  https://doi.org/10.1016/j.ejrh.2023.101578
- Ling, Z., Shu, L., Sun, Y., Wang, R., Li, Y., 2021. Impact of island urbanization on freshwater lenses: A case study on a small coral island. Water (Switzerland) 13, 1–17. https://doi.org/10.3390/w13223272
- Martínez-Moreno, F.J., Monteiro-Santos, F.A., Bernardo, I., Farzamian, M., Nascimento, C., Fernandes, J., Casal, B., Ribeiro, J.A., 2017. Identifying seawater intrusion in coastal areas

- by means of 1D and quasi-2D joint inversion of TDEM and VES data. J. Hydrol. 552, 609–619.
- Martorana, R., Lombardo, L., Messina, N., Luzio, D., 2014. Integrated geophysical survey for 3D modelling of a coastal aquifer polluted by seawater. Near Surf. Geophys. 12, 45–59. https://doi.org/10.3997/1873-0604.2013006
- McNeill, J.D., 1980. Electromagnetic Terrain Conductivity Measurement at Low Induction Numbers. Geonics Ltd. Tech. Note TN-6, Mississauga, Ontario, Canada.
- Nabighian, M.N., Corbett, J.D., 1991. Electromagnetic Methods in Applied Geophysics. Society of Exploration Geophysics. https://doi.org/https://doi.org/10.1190/1.9781560802686
- Nicholls, R.J., Wong, P.P., Burket, V.R., Codignotto, J., Hay, J.E., McLean, R.F., Ragoonaden,
  S., Woodroffe, C.D., 2007. Coastal systems and low-lying areas, in: M.L. Parry, Canziani,
  O.F., Palutikof, J.P., Linden, P.J. van der, Hanson, C.E. (Eds.), Climate Change 2007:
  Impacts, Adaptation and Vulnerability. Cambridge University Press, Cambridge, UK, pp.
  315–356.
- Nielsen, L., Jørgensen, N.O., Gelting, P., 2007. Mapping of the freshwater lens in a coastal aquifer on the Keta Barrier (Ghana) by transient electromagnetic soundings. J. Appl. Geophys. 62, 1–15. https://doi.org/10.1016/j.jappgeo.2006.07.002
- NOAA, 2023. What threats do coastal communities face? National Ocean Service website [WWW Document]. URL https://oceanservice.noaa.gov/facts/coastalthreat.html (accessed 5.25.23).
- NOAA, 2021. What is a barrier island? National Ocean Service website [WWW Document].

- URL https://oceanservice.noaa.gov/facts/barrier-islands.html (accessed 5.25.23).
- Nott, J., 2006. Tropical cyclones and the evolution of the sedimentary coast of northern Australia. J. Coast. Res. 22, 49–62.
- NPS, 2024. Weather [WWW Document]. Weather Forecast Malaquite Beach Area. URL https://www.nps.gov/pais/planyourvisit/weather.htm (accessed 7.6.24).
- Paepen, M., Hanssens, D., De Smedt, P., Walraevens, K., Hermans, T., 2020. Combining resistivity and frequency domain electromagnetic methods to investigate submarine groundwater discharge in the littoral zone. Hydrol. Earth Syst. Sci. 24, 3539–3555. https://doi.org/10.5194/hess-24-3539-2020
- Paine, J.G., 2003. Determining salinization extent, identifying salinity sources, and estimating chloride mass using surface, borehole, and airborne electromagnetic induction methods.

  Water Resour. Res. 39. https://doi.org/10.1029/2001WR000710
- Panthi, J., Boving, T.B., Pradhanang, S.M., Russoniello, C.J., Kang, S., 2024. The contraction of freshwater lenses in barrier island: A combined geophysical and numerical analysis. J.Hydrol. 637, 131371. https://doi.org/10.1016/j.jhydrol.2024.131371
- Patra, H.P., Bhattacharya, P.K., 1966. Geophysical exploration for ground water around Digha in the coastal region of West Bengal, India. Geoexploration 4. https://doi.org/10.1016/0016-7142(66)90019-6
- Pendleton, E.A., Thieler, E.R., Williams, S.J., Beavers, R.L., 2004. Coastal Vulnerability

  Assessment of Padre Island National Seashore (PAIS) to Sea-Level Rise: US Geological

  Survey Open-File Report 2004-1090, 1-25.

- https://doi.org/https://www.researchgate.net/publication/237683541
- Pondthai, P., Everett, M.E., Micallef, A., Weymer, B.A., Faghih, Z., Haroon, A., Jegen, M., 2020. 3D characterization of a coastal freshwater aquifer in SE malta (mediterranean sea) by time-domain electromagnetics. Water (Switzerland) 12. https://doi.org/10.3390/W12061566
- Reid, J.E., Howlett, A., 2001. Application of the EM-31 terrain conductivity meter in highly-conductive regimes. Explor. Geophys. 32, 219–224.
- Ruggiero, P., Hacker, S., Seabloom, E., Zarnetske, P., 2018. The role of vegetation in determining dune morphology, exposure to sea-level rise, and storm-induced coastal hazards: a US Pacific Northwest perspective, in: Barrier Dynamics and Response to Changing Climate. Springer, pp. 337–361.
- Russoniello, C.J., Konikow, L.F., Kroeger, K.D., Fernandez, C., Andres, A.S., Michael, H.A., 2016. Hydrogeologic controls on groundwater discharge and nitrogen loads in a coastal watershed. J. Hydrol. 538. https://doi.org/10.1016/j.jhydrol.2016.05.013
- Sallenger Jr, A.H., 2000. Storm impact scale for barrier islands. J. Coast. Res. 16, 890–895.
- Sathish, S., Elango, L., 2016. An integrated study on the characterization of freshwater lens in a coastal aquifer of Southern India. Arab. J. Geosci. 9. https://doi.org/10.1007/s12517-016-2656-7
- Satish Kumar, V., Dhakate, R., Amarender, B., Sankaran, S., 2016. Application of ERT and GPR for demarcating the saline water intrusion in coastal aquifers of Southern India. Environ. Earth Sci. 75, 1–17. https://doi.org/10.1007/s12665-015-5207-8

- Schneider, J.C., Kruse, S.E., 2006. Assessing selected natural and anthropogenic impacts on freshwater lens morphology on small barrier Islands: Dog Island and St. George Island, Florida, USA. Hydrogeol. J. 14, 131–145. https://doi.org/10.1007/s10040-005-0442-9
- Schneider, J.C., Kruse, S.E., 2003. A comparison of controls on freshwater lens morphology of small carbonate and siliciclastic islands: Examples from barrier islands in Florida, USA. J. Hydrol. 284, 253–269. https://doi.org/10.1016/j.jhydrol.2003.08.002
- Sherwood, C.R., Ritchie, A.C., Over, J.S.R., Kranenburg, C.J., Warrick, J.A., Brown, J.A.,
  Wright, C.W., Aretxabaleta, A.L., Zeigler, S.L., Wernette, P.A., Buscombe, D.D.,
  Hegermiller, C.A., 2023. Sound-Side Inundation and Seaward Erosion of a Barrier Island
  During Hurricane Landfall. J. Geophys. Res. Earth Surf. 128, 1–32.
  https://doi.org/10.1029/2022JF006934
- Shevnin, V., Mousatov, A., Ryjov, A., Delgado-rodriquez, O., 2007. Estimation of clay content in soil based on resistivity modelling and laboratory measurements. Geophys. Prospect. 55, 265–275. https://doi.org/10.1111/j.1365-2478.2007.00599.x
- Shideler, G.L., 1986. Seismic and physical stratigraphy of late Quaternary deposits, South Texas coastal complex. US Geol. Surv. Prof. Pap. 1328, 9–31.
- Simms, A.R., Anderson, J.B., Blum, M., 2006. Barrier-island aggradation via inlet migration:

  Mustang Island, Texas. Sediment. Geol. 187, 105–125.

  https://doi.org/10.1016/j.sedgeo.2005.12.023
- Small, C., Nicholls, R.J., 2003. A global analysis of human settlement in coastal zones. J. Coast. Res. 19, 584–599.

- Soupios, P.M., Kalisperi, D., Kanta, A., Kouli, M., Barsukov, P., Vallianatos, F., 2010. Coastal aquifer assessment based on geological and geophysical survey, northwestern Crete, Greece. Environ. Earth Sci. 61, 63–77.
- Stone, G.W., McBride, R.A., 1998. Louisiana Barrier Islands and their importance in wetland protection: Forecasting shoreline change and subsequent response of wave climate. J. Coast. Res. 14.
- Stutz, M.L., Pilkey, O.H., 2011. Open-ocean barrier islands: Global influence of climatic, oceanographic, and depositional settings. J. Coast. Res. 27, 207–222. https://doi.org/10.2112/09-1190.1
- Tajul Baharuddin, M.F., Othman, A.R., Taib, S., Hashim, R., Zainal Abidin, M.H., Radzuan, M.A., 2013. Evaluating freshwater lens morphology affected by seawater intrusion using chemistry-resistivity integrated technique: A case study of two different land covers in Carey Island, Malaysia. Environ. Earth Sci. 69, 2779–2797. https://doi.org/10.1007/s12665-012-2098-9
- Thissen, L., Greskowiak, J., Gaslikova, L., Massmann, G., 2024. Climate change impact on barrier island freshwater lenses and their transition zones: a multi-parameter study.

  Hydrogeol. J. https://doi.org/10.1007/s10040-024-02800-3
- Todd, D.K., Mays, L.W., 2004. Groundwater hydrology. John Wiley & Sons.
- Torres, J., Kulp, M., FitzGerald, D., Georgiou, I., Lepper, K., 2020. Geomorphic and temporal evolution of a Mississippi delta flanking barrier island: Grand Isle, LA. Mar. Geol. 430, 106341. https://doi.org/10.1016/j.margeo.2020.106341

- TPWD, 2024. Texas Parks and Wildlife Department, Upper Laguna Madre [WWW Document].

  URL https://tpwd.texas.gov/landwater/water/habitats/bays/ulm/ulm\_index.phtml (accessed 7.4.23).
- Trabelsi, F., Mammou, A. Ben, Tarhouni, J., Piga, C., Ranieri, G., 2013. Delineation of saltwater intrusion zones using the time domain electromagnetic method: The Nabeul-Hammamet coastal aquifer case study (NE Tunisia). Hydrol. Process. 27. https://doi.org/10.1002/hyp.9354
- Tully, K., Gedan, K., Epanchin-Niell, R., Strong, A., Bernhardt, E.S., Bendor, T., Mitchell, M., Kominoski, J., Jordan, T.E., Neubauer, S.C., Weston, N.B., 2019. The invisible flood: The chemistry, ecology, and social implications of coastal saltwater intrusion. Bioscience. https://doi.org/10.1093/biosci/biz027
- UNEP, 2014. The importance of mangroves to people: A call to action, United Nations Environment Programme World Conservation Monitoring Centre.
- Urisha, D.W., Ozbilginb, M.M., 1989. The Coastal Ground-Water Boundary. Ground Water 27, 310–315.
- USGS, 2022. What is the vertical accuracy of the 3D Elevation Program (3DEP) DEMs? [WWW Document]. URL https://www.usgs.gov/faqs/what-vertical-accuracy-3d-elevation-program-3dep-dems (accessed 5.25.23).
- USGS, 2020. U.S. Geological Survey, 20200330, USGS one meter x69y309 TX South B5 2018:

  U.S. Geological Survey [WWW Document]. URL

  https://www.sciencebase.gov/catalog/item/5ead063282cefae35a253d64 (accessed 5.25.23).

- Vafidis, A., Soupios, P., Economou, N., Hamdan, H., Andronikidis, N., Kritikakis, G.,
  Panagopoulos, G., Manoutsoglou, E., Steiakakis, M., Candansayar, E., Schafmeister, M.,
  2014. Seawater intrusion imaging at Tybaki, Crete, using geophysical data and joint inversion of electrical and seismic data. First Break 32. https://doi.org/10.3997/1365-2397.32.8.76970
- Van der veer, P., 1977. Analytical solution for a two-fluid flow in a coastal aquifer involving a phreatic surface with precipitation. J. Hydrol. 35, 271–278. https://doi.org/10.1016/0022-1694(77)90006-3
- Weise, B.R., White, W.A., 1980. Padre Island National Seashore: a guide to the geology, natural environments, and history of a Texas barrier island. Bureau Of Economic Geology, Austin, Texas.
- Werner, A.D., Bakker, M., Post, V.E.A., Vandenbohede, A., Lu, C., Ataie-Ashtiani, B., Simmons, C.T., Barry, D.A., 2013. Seawater intrusion processes, investigation and management: Recent advances and future challenges. Adv. Water Resour. 51, 3–26. https://doi.org/10.1016/j.advwatres.2012.03.004
- Wernette, P., Houser, C., Bishop, M.P., 2016. An automated approach for extracting Barrier Island morphology from digital elevation models. Geomorphology 262, 1–7. https://doi.org/10.1016/j.geomorph.2016.02.024
- Wernette, P., Houser, C., Weymer, B.A., Everett, M.E., Bishop, M.P., Reece, B., 2018. Influence of a spatially complex framework geology on barrier island geomorphology. Mar. Geol. 398, 151–162. https://doi.org/10.1016/j.margeo.2018.01.011
- Winker, C.D., 1979. Late Pleistocene fluvial-deltaic deposition, Texas coastal plain and shelf.

## GCAGS Transactions.

- Withers, K., Smith, E., Gomez, O., Wood, J., 2004. Assessment of Coastal Water Resources and Watershed Conditions at Padre Island National Seashore, Texas.
- Wu, C.L.R., Stigter, T.Y., Craig, S.G., 2022. Assessing the Quantity and Quality Controls of the Freshwater Lens on a Semi-Arid Coral-Limestone Island in Sri Lanka. Front. Water 4, 1–18. https://doi.org/10.3389/frwa.2022.832227

## 2- Section (II)\*

Geological and Anthropogenic Controls on Freshwater Lens Variability in Barrier Islands:

Insights from Integrated Geophysical and Hydrogeological Surveys

(\*) Includes content that is also part of an article that is currently under review at the Journal of Hydrology: Abdelrehim, R., Ahmed, M., Everett, M.E., Murgulet, D., Prothro, L., Abdrabou, M., Omar, A., 2025. Geological and Anthropogenic Controls on Freshwater Lens Variability in Barrier Islands: Insights from Integrated Geophysical and Hydrogeological Surveys, <a href="https://doi.org/10.1016/j.jhydrol.2025.133627">https://doi.org/10.1016/j.jhydrol.2025.133627</a>

#### 2.1 Abstract

Barrier islands act as natural shields for coastal communities, protecting against sea-level rise, storms, and hurricanes. Their groundwater resources, represented by freshwater lenses (FWLs), are vital for sustaining ecosystems but are highly vulnerable to natural changes like seawater intrusion and drought, as well as human activities like canal dredging and housing developments. This study uses high-resolution geophysical, topographical, and hydrogeological surveys to investigate FWL on Padre Island, the longest barrier island in the world, located in southern Texas, USA. The findings reveal that FWL resistivity (33  $\pm$  18  $\Omega$ ·m) and thickness (8  $\pm$  5 m) decline near saltwater bodies like the Gulf of Mexico and Laguna Madre, and in developed areas, primarily due to saltwater intrusion. There were positive correlations (+0.31 to +0.43) between ground elevation and both FWL resistivity and thickness. Higher elevations (>2 m) support thicker (9  $\pm$  4 m) and fresher (34  $\pm$  20  $\Omega$ ·m) FWL due to increased recharge, reduced

evaporation, and limited saltwater intrusion. Dune volume correlates positively ( $\pm 0.51$ ) with FWL thickness, where larger dunes ( $\geq 16,800 \text{ m}^3$ ) sustain a thicker lens ( $10 \pm 3 \text{ m}$ ). In addition, areas with deeper subsurface clay layers ( $13 \pm 4 \text{ m}$ ) accommodate thicker ( $10 \pm 3 \text{ m}$ ) and fresher ( $36 \pm 15 \Omega \cdot \text{m}$ ) FWL, highlighting the influence of geological factors. This study provides a comprehensive framework for understanding FWL dynamics on complex barrier islands and underscores the importance of integrating geological, topographical, and anthropogenic factors to ensure that freshwater is being sustainably managed before further development takes place.

#### 2.2 Introduction

Coastal areas are some of the most densely populated areas on Earth; approximately 38% of the global population lives within 100 km of a coastline (Barbier, 2015; Small and Nicholls, 2003; UNEP, 2014). These regions support myriad activities, including mineral extraction, energy production, tourism and recreation, fishing, and industrial development (Laignel et al., 2023). However, despite their importance, coastal regions are among the environments most severely impacted by human activities, as well as natural changes such as variations in climate (Laignel et al., 2023).

Barrier islands are distinctive coastal geographical features (Conroy and Milosch, 2011; Jin et al., 2015). Worldwide, there are 2,149 individual barrier islands with a combined length of 20,783 km, constituting roughly 10% of all continental shorelines (Stutz and Pilkey, 2011). These elongated, narrow landforms aligned parallel to the mainland serve as critical buffers, protecting coastal ecosystems and human settlements against storm surges and erosion (Grzegorzewski et al., 2011; Stone and McBride, 1998; Torres et al., 2020). In addition, these

islands provide essential habitats for diverse flora and fauna, including migratory birds and endangered species (Conroy and Milosch, 2011; Jin et al., 2015; Sherwood et al., 2023).

The freshwater resources of barrier islands primarily consist of surficial water and shallow aquifers, predominantly replenished by precipitation events (Anderson et al., 2000; Ley et al., 2023). Due to the difference in saltwater and freshwater densities, fresh groundwater in barrier islands exists as a distinct freshwater lens (FWL) atop a denser saltwater layer (Badan Ghyben, 1889; Herzberg, 1901) (Ling et al., 2021; Panthi et al., 2024; Wu et al., 2022). The thickness of the FWL is greatest at the center of the Island, gradually diminishing as it approaches the coastline and the back bay systems (Urisha and Ozbilginb, 1989).

The dimensions and geometry of the FWL during steady-state conditions, assuming a fixed lateral boundary and a sharp fresh and saline water interface, were provided by Henry (1964), Todd and Mays (2004), and Van Der Veer (1977), among others. However, in reality, the actual FWL boundary undergoes continuous fluctuations, and the interface is more accurately described as a transitional zone. This is due to the heterogeneous and anisotropic nature of sedimentary deposits, as well as the continuous movement of both saline water and fresh groundwater (Harris, 1967). The vertical and horizontal dimensions of FWLs are influenced by various factors, including island width and the geological time of their formation, as well as hydrogeological and hydrological variables such as hydraulic properties of the sediments, saltwater intrusion, seasonal and tidal inundation, variations in terrain and vegetation, and groundwater recharge (Anderson et al., 2000; Ault, 2016; Fetter, 1972; Panthi et al., 2024; Schneider and Kruse, 2006).

Several studies have characterized FWLs on barrier islands, along with their spatial or temporal variability (Harris, 1967; Kiflai and Whitman, 2023; Ling et al., 2021; Schneider and

Kruse, 2006; Thissen et al., 2024; Wu et al., 2022). These studies used advanced numerical groundwater modeling techniques to provide detailed insights into FWL properties and their dynamic behavior. The findings of these studies suggest that in areas where fresh and saline water are stratified, freshwater tends to be present in permeable zones, while saline water predominantly occupies low-permeability zones (Harris, 1967). These studies also highlighted the significant influence of geological factors such as sediment types, thickness, and heterogeneity on the distribution of the FWLs (Anderson et al., 2000; Collins and Easley, 1999; Harris, 1967). However, the identification of consistent patterns has been hampered by the largely unmapped variability in barrier island stratigraphy (Davis, 1999). In addition, numerical groundwater models require extensive, dense, and long-term monitoring hydrogeologic datasets, which are often scarce due to the high costs, time, and labor involved in their collection (Ismail et al., 2024). These models also often simplify complex subsurface conditions, which can limit the accuracy of their outputs.

Previous studies employed geophysical techniques to investigate FWLs in various settings. For instance, Nielson et al. (2007) used time-domain electromagnetic (TDEM) surveys to map the freshwater–saltwater interface in Ghana, while Tajul Baharuddin et al. (2013) combined electrical resistivity and geochemical analyses to assess seawater intrusion impacts on FWL morphology in Malaysia. Sathish and Elango (2016) characterized FWLs in southern India using similar techniques. More recently, Costabel et al. (2017) used a combination of electromagnetic geophysical methods to investigate FWLs on German barrier islands. Kiflai and Whitman (2023) employed electrical resistivity to assess the impact of storm surges and recovery processes on FWLs. These studies provided valuable insights into FWL dynamics, but limited research has directly compared FWL characteristics in developed and undeveloped areas. Such

comparisons are needed to understand the effects of human development on the spatial and temporal variabilities in FWLs. Schneider and Kruse (2006) used geophysical techniques and numerical modeling to examine the influence of natural and anthropogenic factors on FWLs in Florida. They found that recharge variability and hydrological conductivity play significant roles in FWL asymmetry, while seasonal variations primarily affect the FWL surface. They also acknowledged the impact of development on FWL thinning. Ling et al. (2021) used numerical modeling to assess the effects of urbanization on FWLs in small coral islands, highlighting the potential for significant reductions in FWL volume due to increased impervious surfaces.

Previous studies rarely integrated a comprehensive analysis of geological, geophysical, hydrogeological, topographical, and anthropogenic factors to understand FWL dynamics on barrier islands. In our study, we address the complex interplay between surface and subsurface characteristics that drive FWL dynamics, offering a holistic approach not previously attempted. Earlier research focused on small barrier islands or limited sections of larger ones, often characterized by simpler geological and morphological conditions. These studies typically relied on a small number of profiles—either parallel or perpendicular to the shoreline—or limited data points, limiting their ability to capture the full complexity of FWL dynamics.

This study represents the first effort to combine geological, geophysical, hydrogeological, and topographical analyses with an assessment of human development impacts to achieve a detailed understanding of the factors influencing FWL characteristics on barrier islands. Unlike prior studies, this research investigates the intricate relationships between FWL properties and the complex surface morphology and subsurface geological conditions of Padre Island, in southern Texas (Figure 2-1). Using an innovative approach, we integrated TDEM geophysical soundings with hydrogeological and topographical surveys to characterize the spatial variability

of the FWL along and across-shore. This comprehensive dataset enabled us to assess how subsurface geology, surface morphology, and human activities affect FWL salinity, thickness, and lateral distribution. The insights gained from this study are critical not only for understanding FWL dynamics on Padre Island but also for providing a transferable framework for studying other complex barrier systems worldwide.

## 2.3 Study Area

Padre Island is located on the Gulf of Mexico (GOM) coast of Texas and is the longest connected barrier island in the world (length ~185 km) (Figure 2-1). It is roughly 3 km wide and extends from the city of Corpus Christi in the north to the South Padre Island resort in the south (Pendleton et al., 2004). The island has a roughly north—south (N-S) orientation, with the GOM on the east and the hypersaline Laguna Madre (LM) on the west. Most of Padre Island is preserved as Padre Island National Seashore (length: 108 km), and a portion of the lower island (South Padre Island) is protected as part of the Laguna Atascosa National Wildlife Refuge (length: 56 km). The study area extends from the Mustang Island—Padre Island border in the north to Bird Island Basin Road, spanning approximately 24 km (Figure 2-1). This area comprises a diverse landscape, encompassing both developed regions and seemingly protected undeveloped stretches (Figure 2-1a).

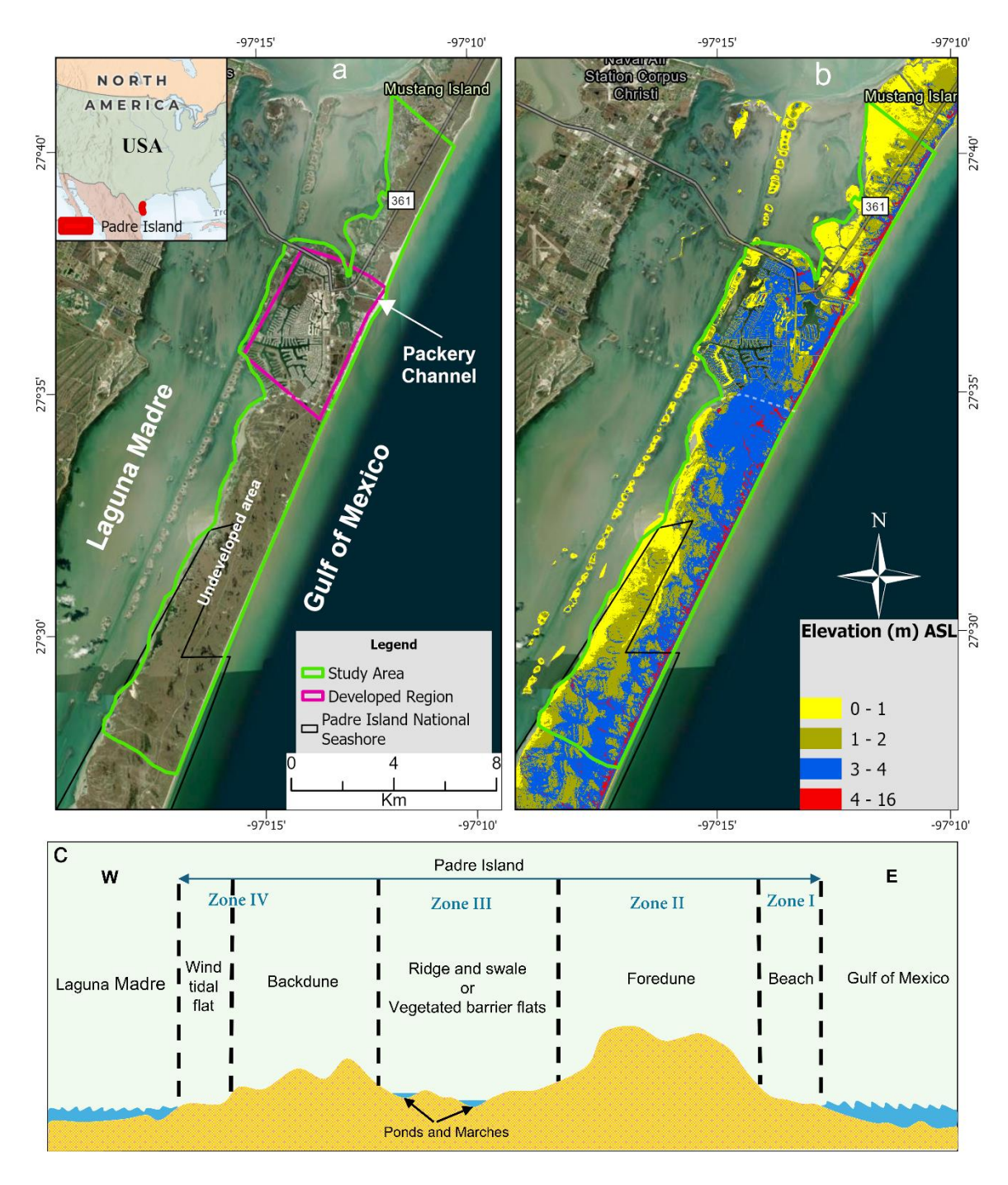


Figure 0-1. (a) Location map of the study area on Padre Island, including developed and undeveloped zones. The insert shows Padre Island's location, off the coast of southern Texas, USA. (b) High-resolution (1-m) DEM of the study area shows the elevation of the study area, in meters above sea level. (c) Padre Island general cross-section, illustrating the island's diverse geomorphological features (modified from Brown et al. 1977).

The geologic history and origin of Padre Island have been discussed in detail in Brown et al., (1977), Garrison et al., (2010), Houser et al., (2018), and Wernette et al., (2018). During the Pleistocene interglacial stages, inland rivers and streams discharged along the Gulf Coast shoreline through a network of deltas, which were located near the present-day continental shelf edge. In the vicinity of present-day wind-tidal flats, the headwater tributaries of incised valley systems deeply eroded the Pleistocene ravinement surfaces and filled them with Pleistocene river deposits. During the Holocene, the sea level rose and flooded the preexisting stream valleys, and some of them became bays and estuaries. When the sea levels stabilized, offshore bars and sand shoals between the drowned river valleys began to merge. In the late Holocene, the shoals emerged from the sea to become a series of low, discontinuous sandy islands aligned parallel to the mainland shoreline. Stratigraphically, the Pleistocene sand and mud are the base of the barrier-lagoon system, overlain by shoreface sand and mud, washover and aeolian deposits, and lagoonal mud (Brown et al., 1977; Houser et al., 2018). The Pleistocene ravinement surface (Beaumont formation) varies considerably across the length and the width of the island. This boundary shows a consistent seaward dip (average gradient of 5 m per kilometer), likely attributable to a combination of initial paleo slope conditions and subsidence effects (Shideler, 1986). The thickness of the modern Holocene deposits of shoreface sands is estimated to be 2–3 m, whereas the thickness of older Holocene shoreface sands and muds can be ~10 m or greater within the paleochannels (Garrison et al., 2010).

A topographical analysis of 1-m-resolution digital elevation model (DEM) data shows that Padre Island exhibits a range of elevations extending from the mean sea level up to ~16 m above mean sea level. Despite the wide range in elevations, the mean elevation of the study area

is relatively low, averaging only  $\sim$ 1.7 m (Figure 2-1b). Figure 2-1c shows a general cross-section of the island, delineating the diverse coastal geomorphological features that span from the GOM to the LM (Brown et al., 1977).

Padre Island exhibits a subtropical semiarid climate, characterized by predominantly hot and arid conditions (Anderson et al., 2014; Weise and White, 1980; Withers et al., 2004). In January, the average minimum temperature dips to around 15°C. August boasts the warmest temperatures, with an average maximum reaching 29°C (NPS, 2024). Precipitation levels across Padre Island vary in amount and frequency, with the northern region experiencing approximately 79 cm/year and the southern area receiving around 64 cm/year. Drought occurrences are common, with evaporation rates averaging 158 cm/year, typically surpassing precipitation levels (Withers et al., 2004).

The tidal regime prevalent across Padre Island is micro-tidal, characterized by minimal tidal amplitudes of less than 0.5 m (Hill and Hunter, 1976). On the beachfront, tidal patterns may be amplified by strong wind currents (Withers et al., 2004). Gulf tides typically adhere to a diurnal rhythm, although there are instances of a mixed semi-diurnal tide pattern (Weise and White, 1980).

Within Padre Island, groundwater resides in an unconfined aquifer, primarily comprised of Holocene eolian/marine sands deposited atop the Pleistocene-age Beaumont Formation (Berkebile and Hay, 1995). The freshwater zone lies above the seawater zone. It gradually thickens as it extends toward the island's central region before tapering into a thinner layer to the west, near the LM, and the east, near the GOM. Groundwater discharge occurs mainly through direct seepage to both the GOM and the LM (Berkebile and Hay, 1995).

#### 2.4 Data and Methods

A comprehensive suite of geophysical, hydrogeological, and topographical surveys was acquired across Padre Island to provide detailed vertical and spatial information on the FWL, along with insights into subsurface geological and hydrogeological characteristics. The TDEM data provided detailed information about the thickness and depth of subsurface layers, along with their electrical resistivity, which is predominantly influenced by sediment composition, porosity, groundwater saturation, and salinity. Water samples were collected at several TDEM locations and served as ground truth for calibrating TDEM models. Topographical surveys were used to evaluate the relationship between surface geomorphological features and the subsurface hydrogeological features revealed by TDEM data.

## 2.4.1 Time-domain Electromagnetic (TDEM) Geophysical Survey

Several geophysical techniques are widely employed for mapping freshwater resources and saltwater intrusion in coastal regions (Kalisperi et al., 2018; Kanta et al., 2013; Kourgialas et al., 2016; Patra and Bhattacharya, 1966; Soupios et al., 2010; Vafidis et al., 2014). Among the commonly used techniques are electrical methods (Adeoti et al., 2010; Kiflai and Whitman, 2023; Martínez-Moreno et al., 2017) and electromagnetic methods, which include magnetotellurics (Falgàs et al., 2009), ground-penetrating radar (Satish Kumar et al., 2016), frequency-domain (Abdelrehim et al., 2023; Attwa et al., 2011; Paepen et al., 2020; Schneider and Kruse, 2006, 2003), and TDEM methods (El-Kaliouby and Abdalla, 2015; Gonçalves et al., 2017; Martínez-Moreno et al., 2017; Martorana et al., 2014; Pondthai et al., 2020). These techniques detect variations in subsurface electrical conductivity, which are influenced by lithological properties, notably clay content, porosity, saturation, and groundwater chemistry

(Archie, 1942; Barrett et al., 2002). TDEM techniques are highly favored across diverse environments, including coastal environments, due to their minimal disruption to the landscape, straightforward deployment protocols, sensitivity to changes in the subsurface material conductivity, and efficient data collection capabilities (Abouelmagd et al., 2020; Al-Garni and El-Kaliouby, 2011; Ardali et al., 2018; Golshan et al., 2018; Kalisperi et al., 2018; Trabelsi et al., 2013).

The principles of operation of the TDEM technique are covered in detail by Nabighian & Corbett (1991) and Everett (2013). A typical TDEM system employs a current waveform that starts with a slow rise to a steady value, followed by a rapid shutoff, resembling a linear ramp (Figure 2-S1a). When this current passes through the transmitter loop, it generates a primary magnetic field directly proportional to, and in phase with, the transmitter current. Faraday's law of induction dictates that an impulsive electromotive force is also induced. This electromotive force is proportional to the negative rate of change of the primary magnetic field over time. During the current shutoff phase, the induced electromotive force drives eddy currents within the conductive ground (Figure 2-S1b). After the current ramp terminates, the electromotive force vanishes, and the eddy currents begin to decay due to Ohmic dissipation. This decay process produces a weak secondary magnetic field whose strength diminishes with time. The receiver coil measures the rate of change of this decaying secondary magnetic field with time (Figure 2-S1c). In many TDEM systems, receiver voltage measurements are taken during the "off-time" after the transmitter current has stopped. The advantage of off-time recording is to avoid masking the relatively weak secondary signal with the significantly stronger primary signal that is present during the "on-time" when the transmitter current is flowing.

A Geonics G-TEM system (Figure 2-2a) was employed to acquire the TDEM-sounding data at 99 locations and 3 repeat stations for data quality control across the study area, which encompasses both developed and undeveloped areas (Figure 2-3). We used a Slingram configuration, with a square  $10\text{-m} \times 10\text{-m}$  T<sub>X</sub> loop and a high-frequency 0.6-m diameter R<sub>X</sub> coil at 15 m offset from the T<sub>X</sub> center (Figure 2-2a). The effective area of the R<sub>X</sub> coil is 31.4 m<sup>2</sup>. Following a comprehensive testing, a R<sub>X</sub> gain setting of 3 was considered to be the optimal gain for the study area and was thereafter applied consistently throughout the survey. At each location, the T<sub>X</sub> generated a 3-A current ramp-off waveform, and the R<sub>X</sub> measured the induced voltage decay over 30-time gates ranging from 88.13 to 6978  $\mu$ s. Each sounding consisted of four records, with a 15-second integration time per record, collected at a 30-Hz base frequency.

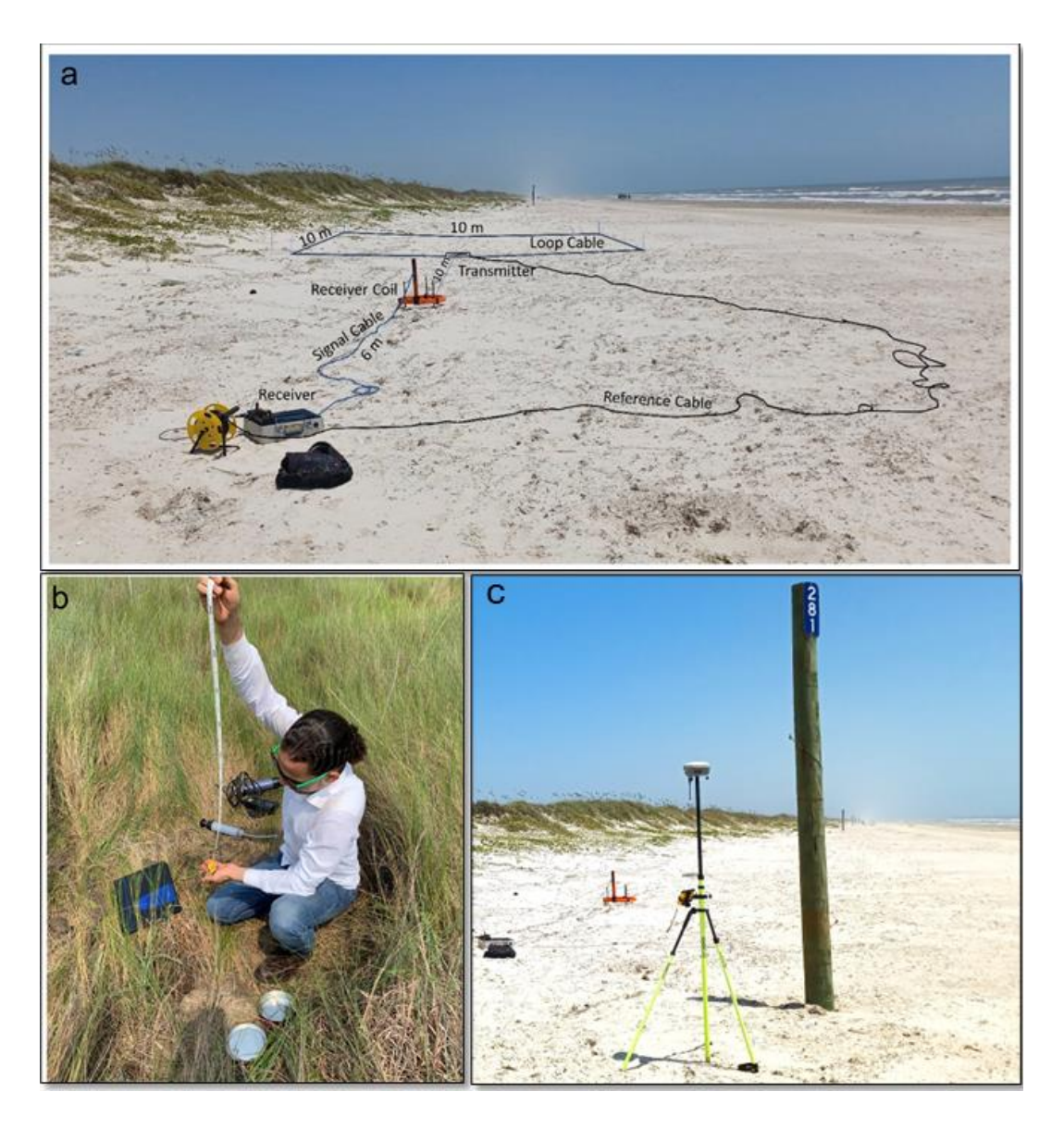


Figure 0-2. Fieldwork on Padre Island: (a) Geonics G-TEM system setup for TDEM data acquisition, showing the Slingram configuration. The square 10-m × 10-m TX loop and the 0.6-m-diameter RX coil are positioned 15 m away from the TX loop's center. (b) Water sample collection and field analysis. (c) Location and elevation measurements using the Trimble R8 Global Navigation Satellite System (GNSS) receiver (Author under review article).

The majority of the TDEM data collection occurred primarily during the dry months (July 2023, September 2023, and May 2024), with a smaller subset (19 soundings) acquired in wetter conditions during January 2024 (Table S1). TDEM soundings were collected along 12 profiles perpendicular to the shoreline and 2 longer profiles parallel to the shoreline (Figure 2-3). Within each perpendicular profile, TDEM stations are numbered consecutively from east to west, starting at the GOM coast and progressing toward LM. Sounding names were assigned to include both profile and station names (e.g., PV11TEM12 means profile vertical [PV] 11, TEM station 12). Areas with potential anthropogenic electromagnetic interference (e.g., powerlines, pipelines) were avoided during data acquisition. To visualize the spatial distribution of hydrogeological features within the study area, the one-dimensional (1D) model inverted from each TDEM sounding was compiled into two-dimensional (2D) resistivity cross-sections along 12 shorenormal (length: 0.5–3 km) and 2 shore-parallel (length: ~23 km) profiles (Figures 2-5–10).

Following data acquisition, the TDEM-sounding data were visually inspected on log-log plots that compare resistivity to time. Outlier points or those exhibiting early-time reverse polarity due to the survey configuration (the receiver is placed outside the transmitter coil, so reverse-polarity signals are possible) were removed or masked before inversion. Soundings with excessive noise (more than 10 outlier data points) were reacquired at the same locations. The TDEM data were then inverted using IX1D software (Interpex, 2008), applying a smooth model inversion approach based on Occam's principle (Constable et al., 1987) to estimate subsurface resistivity depth profiles. An iterative inversion continued until a root-mean-square error (RMS) below 10% was achieved (80% of the layered models and 70% of the smooth models had RMS less than 6%). Initial layered model inversions used six to eight layers, which was subsequently simplified to three layers to better reflect the known hydrogeological framework of Padre Island:

(1) uppermost dry/unsaturated zone transitioning into a freshwater-saturated zone, recognized as the FWL; (2) intermediate saltwater-saturated zone; and (3) basal low-permeability Pleistocene clay layer. Resistivity constraints for each layer were informed by existing literature (El-Kaliouby and Abdalla, 2015; Kalisperi et al., 2018; Pondthai et al., 2020; Shevnin et al., 2007), onsite measurements of resistivity and water salinity, and available well data (Berkebile and Hay, 1995). Freshwater-saturated sand (e.g., FWL) resistivities were constrained to 8–100  $\Omega$ ·m, salt/brackish-water saturated sand to 1–8  $\Omega$ ·m, and the saltwater-saturated Pleistocene clay to <1  $\Omega$ ·m.

Because the geophysical inversions were inherently non-unique, we performed an equivalence analysis to assess the range of layered models consistent with an observed TDEM sounding. This analysis aimed to identify alternative models that could adequately explain the data beyond the single best-fit solution. The principle of equivalence acknowledges that in real-world scenarios with discrete measurements and potential errors, multiple models can often fit observed resistivity data within a prescribed acceptable tolerance (Interpex, 2008). For each sounding, up to 30 equivalent models were identified. To ensure robust interpretation, we implemented a two-step quality control process: (1) Outlier identification and exclusion: We carefully identified initial equivalent model sets that included outliers that deviated significantly from the general resistivity-versus-depth trend. These were removed from further analysis. (2) Model statistical analysis: The remaining equivalent models for each station were averaged to better balance model complexity and interpretability. Their standard deviation was used to represent the uncertainty ranges in both resistivities and thicknesses. The average model statistics are provided in the supplementary material (Figure 2-S3).

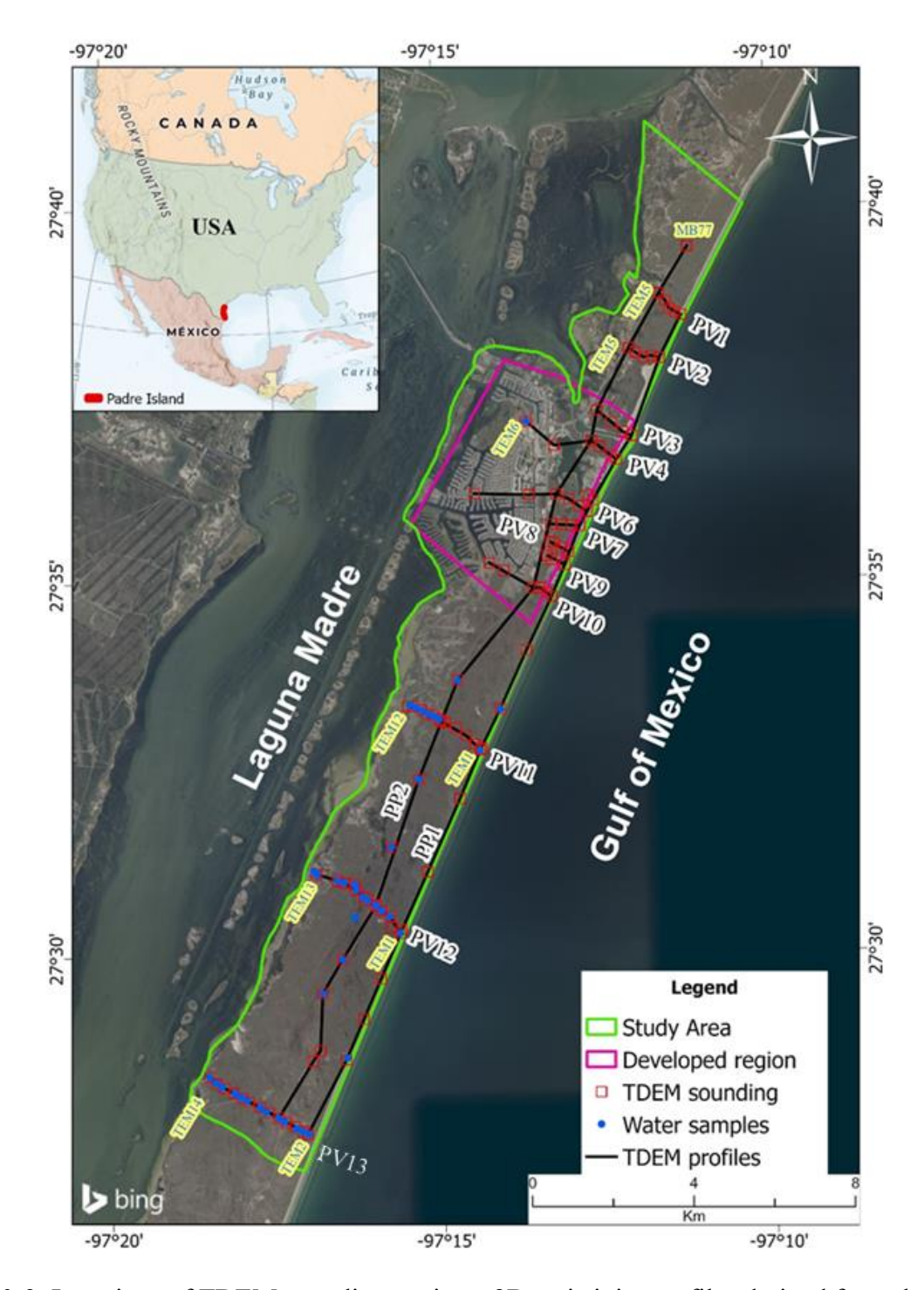


Figure 0-3. Locations of TDEM sounding stations, 2D resistivity profiles derived from the inverted data, and collected water samples. Sounding names include both profile number and station/sounding identifiers (e.g., PV11TEM12 means profile 11, sounding 12).

## 2.4.2 Hydrogeological Survey

To complement, validate, and refine the TDEM interpretation, 44 groundwater samples were collected from locations across Padre Island (Figure 2-2b; Table 2-S1). Of these, 41 samples were obtained from hand-augured holes (auger depth: 1.8 m) co-located with TDEM soundings. The remaining three samples were collected from surface water sources (surface ponds, the GOM beach, and LM beach). The average depth to groundwater in the hand-augured holes was 0.5 m (range: 0.1–1.35 m). Field measurements of electrical conductivity in microsiemens per centimeter (μS/cm) and salinity in a practical salinity unit (PSU) were made for the collected water samples using a YSI ProDSS multiparameter. Groundwater salinity is directly correlated with electrical conductivity at a shallow depth inferred from resistivity data (conductivity = 1/resistivity) obtained from the TDEM soundings (Goldman, 1988; Paine, 2003; Trabelsi et al., 2013). The following salinity ranges were used to categorize water samples: freshwater: <1 PSU; slightly saline: 1–3 PSU; moderately saline: 3–10 PSU; very saline: 10–35 PSU; and brine: >35 PSU (Heath, 1983). The salinity of a GOM water sample was measured at 34.5 PSU and an LM water sample was 58 PSU.

## 2.4.3 Topographical Survey

A GNSS receiver (Trimble R8) (Figure 2-2c) was employed to obtain precise coordinates and elevations for 55 of the TDEM soundings. The remaining soundings were geolocated using a handheld Garmin GNSS. The collected elevations were then used along with a high-resolution (1-m) LiDAR-derived DEM collected over Padre Island (USGS, 2020). GNSS measurements, which are known for their precision in capturing ground-level elevations at specific points, were combined with DEM-derived elevations, which provide a broader, continuous representation of

the landscape. This integration allowed for a comprehensive assessment of the surface variations across the study area and provided a robust dataset for further geospatial and statistical analysis. These data were used to assess the relationship between surface geomorphological features and the subsurface hydrogeological features revealed by the TDEM data.

To more accurately represent station elevations and account for variations in the topography of the surrounding area, a 200-m buffer zone was created around each TDEM station. The average elevation within this buffer was used to represent the ground elevation. A 200-m buffer size was chosen to effectively capture local variations in elevation and dune volume around each station, because the surrounding topography strongly influences the station locations. These areas receive recharge primarily from their immediate surroundings. In some cases, although the stations are positioned within dune fields, data were collected in relatively flat, lower-elevation areas due to the challenges of acquiring measurements directly on the dunes. However, these locations still broadly represent conditions within the high dune field. In addition, the 200-m buffer minimizes significant overlap between TDEM stations between consecutive stations along any given profile. The same buffer was applied to calculate dune volume using ArcGIS to calculate the three-dimensional (3D) volume above a specific elevation threshold, in our case, the volume above 2-m elevation (an average dune toe elevation in the area) (Wernette et al., 2016). Both dune height and volume were later used to examine their effects on the characteristics of the FWL.

#### 2.5 Results

#### 2.5.1 TDEM Data Inversion

Three main layers were identified from the TDEM inversion results: freshwater-saturated sands (recognized as the FWL), salt/brackish water-saturated sands, and the Pleistocene clay layer. Statistical analysis of equivalent models (Figure 2-S3) indicated that the FWL (uppermost Layer 1) exhibited an average resistivity of 33  $\Omega$ ·m and an average thickness of 8 m, with the standard deviation (the error bars) representing the uncertainty range at each sounding location (Figure 2-S3a). The saline/brackish water zone (Layer 2) showed an average resistivity of 4  $\Omega$ ·m and an average thickness of 6 m (Figure 2-S3b). Finally, the Pleistocene clay layer (basal Layer 3) displayed an average resistivity of 0.3  $\Omega$ ·m and an average depth of 14 m (Figure 2-S3c).

Several soundings were collected in a distinct geographical setting for calibration of TDEM inversion with ground truth data: near a well with recorded lithology as PV13 profile and MB77 station (Simms et al., 2006) (Figure 2-4a), at the beach (Figure 2-4b), at the island center (Figure 2-4c), and near LM (Figure 2-4d). Notably, the RMS misfit for the soundings does not exceed 6%. In addition, the equivalent models exhibit minimal deviation from the best-fit model.

We compared the TDEM-derived results with existing well data along the Bird Island Road (PV13) profile, which reached the Pleistocene clay layer (Hunter and Dickinson, 1970). The TDEM inversion results at these locations were compared to the actual depths of the clay layer (e.g., Figure 2-4c), as recorded in the wells. The comparison revealed a high degree of agreement for six out of the seven TDEM stations, with differences consistently less than ±1.5 m. However, one station, PV13TEM5, exhibited a discrepancy of more than 5 m between the TDEM-derived depth and the well data.

Sounding MB77 (Figure 2-4a) reveals a three-layer model consistent with the known stratigraphy: 9-m-thick dry/freshwater-saturated sediments characterized by resistivity of 70  $\Omega$ ·m, underlain by 4-m-thick saline/brackish saturated sediments with resistivity of 1.2  $\Omega$ ·m. The basal Pleistocene clay layer, encountered at a depth of 13 m, exhibits a low resistivity of 0.2  $\Omega$ ·m, consistent with high clay content. Notably, the TDEM-derived depth to clay (13 m) closely matches the 14 m depth reported in the nearby well (Simms et al., 2006).

Figure 2-4b presents a TDEM sounding (PV12TEM1) at the GOM beach, revealing a thin FWL layer of 2.2 m and low resistivity values around 12  $\Omega$ ·m. In contrast, Figure 2-4c shows a TDEM sounding from the island center, indicating a much thicker FWL of approximately 14 m with relatively high resistivity values exceeding 30  $\Omega$ ·m, as well as a deep clay layer at a depth of around 19 m.

Sounding PV12TEM12 (Figure 2-4d), acquired in a hypersaline salt marsh near LM, shows resistivity values below 1  $\Omega$ ·m. At that location, the Pleistocene clay layer was detected at a mere 0.6 m deep using a hand auger. The measured water salinity of 108 PSU indicates a brine-like environment. The TDEM signal exhibited early-time reverse polarity in the first 11 of the 30-time gates at this site. Similar locations near LM (e.g., PV12TEM13, PV11TEM12, PV3TEM5) and close to the GOM (e.g., PV13TEM2, PV12TEM1, PV12TEM5, PP1TEM1) have witnessed the same effects with a smaller number of time gates.

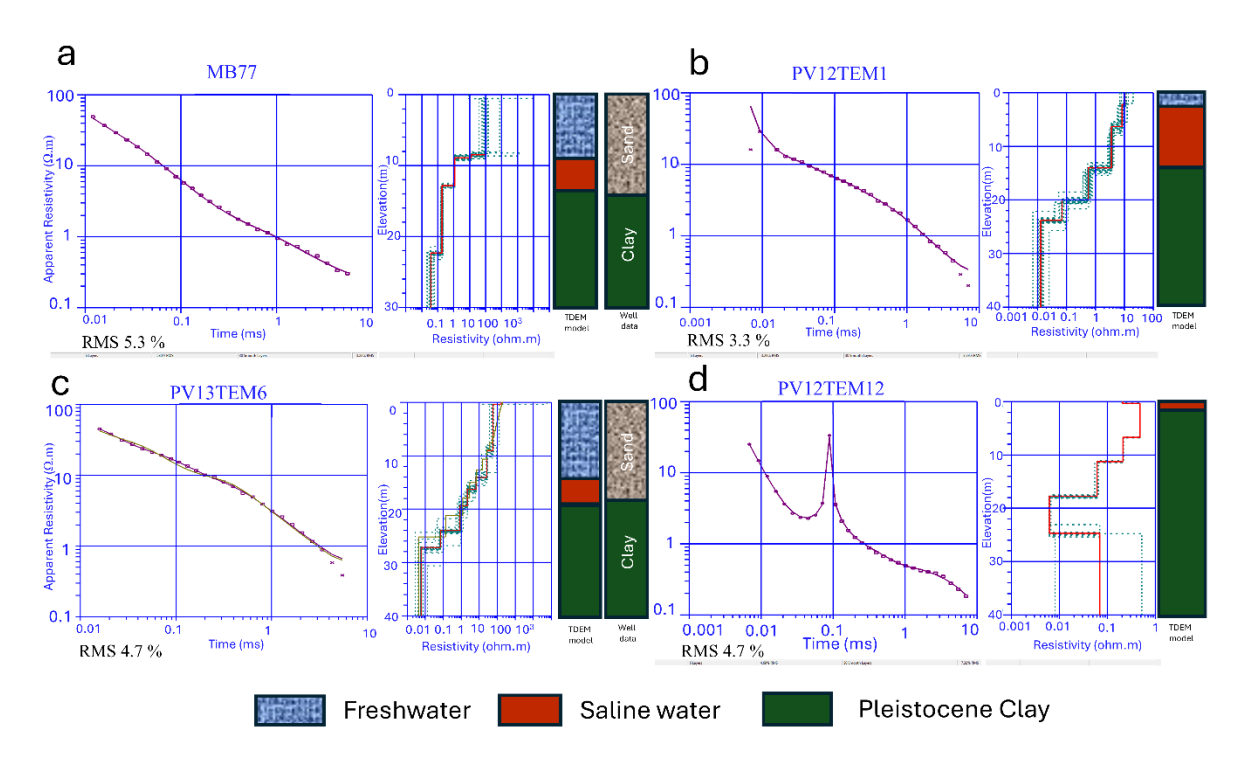


Figure 0-4. Inversion results for four representative TDEM soundings from distinct geographical settings across Padre Island: (a) near a well with recorded lithology, (b) at the beach, (c) at the island center and near a well with recorded lithology, and (d) near LM. The left side of each panel shows the TDEM-measured data. The center of each panel displays the best-fit model (red continuous line) alongside equivalent model solutions (dashed dark green lines). The right side of each panel contains the inversion results and the interpretation of a three-layer model for the sounding station (Author article under review, Journal of Hydrology).

# 2.5.2 Spatial Variability in Subsurface Conditions and Surface Topography in Cross-shore and Along-shore Directions

The subsurface conditions, including electrical resistivity, thickness of the three TDEMderived subsurface layers, and groundwater salinity, were analyzed in cross-shore and alongshore directions in conjunction with surface topography. Elevation was categorized into three classes: low (<1 m), intermediate (1–2 m), and high (>3 m). Resistivity values were similarly grouped to reflect subsurface characteristics: low ( $\leq$ 1  $\Omega$ ·m) corresponding to the clay layer, intermediate (>1 to  $\leq$ 8  $\Omega$ ·m) representing salt/brackish water, and high (>8  $\Omega$ ·m) indicating freshwater. In addition, the depth to the clay layer was classified into three ranges: shallow ( $\leq$ 5 m), intermediate (>5 to  $\leq$ 10 m), and deep (>10 m).

Profile PV11, located cross-shore in a pristine area of the island (Figure 2-3), serves as a reference baseline for understanding the state of the subsurface hydrogeological conditions (e.g., FWL) and their relationships with topography (Figure 2-5). This TDEM profile was collected on 15 September 2023 and 26 January 2024 (with water samples obtained only on the latter date). Stations PV11TEM10 and PV11TEM11, located closer to LM (elevations: 2.24 and 2 m, respectively), exhibited a thin (4–7 m) and high-resistivity (20–70  $\Omega$ ·m) FWL. In contrast, toward the central portion of the island (e.g., PV11TEM6, PV11TEM7, and PV11TEM8) a relatively thicker FWL (8–10 m) was mapped (Figure 2-5b). This area exhibits fresh to slightly saline water (0.84–1.4 PSU) and low resistivity values (10–30  $\Omega$ ·m) (Figure 2-5c). At the central parts of the island (e.g., PV11TEM5) the FWL thickness reaches its maximum (15.3 m) (Figure 2-5a).

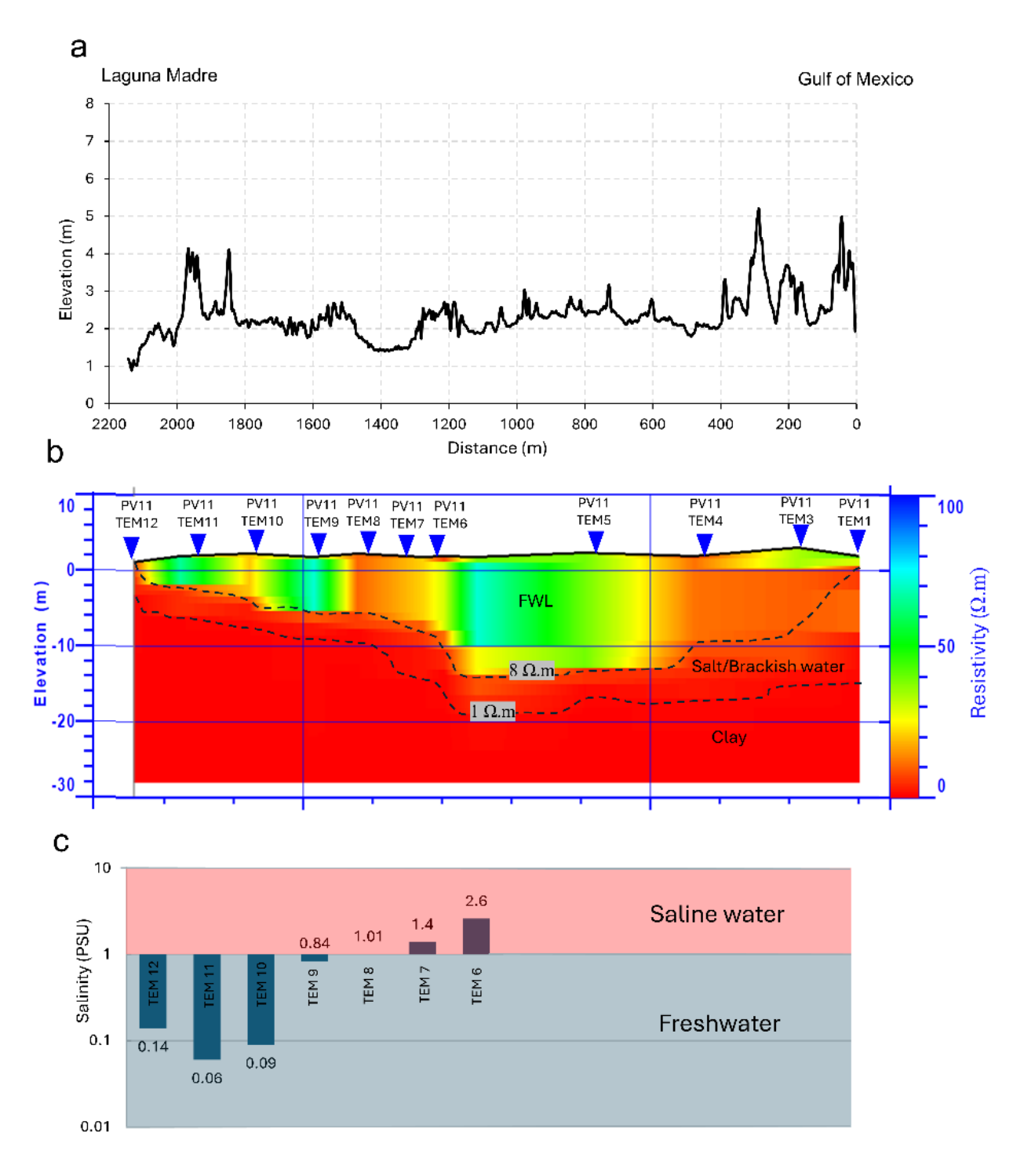


Figure 0-5. (a) Elevation, (b) resistivity profile, and (c) salinity for profile PV11. In panel b, the contour lines at 8 and 1  $\Omega$ .m delineate the approximate depths to the saltwater interface and the top of the Pleistocene clay layer, respectively.

Stations PV11TEM1 and PV11TEM3 near the GOM, and PV11TEM12 located near LM, showed resistivity values for the FWL of around 30  $\Omega$ ·m (Figure 2-5b), a small thickness of less than 3 m, and average elevations of 2 m for GOM stations and 1.2 m for the LM station. The resistivity and thickness of the saline/brackish water layer are significantly higher at the locations close to the GOM ( $\sim$ 5  $\Omega$ ·m and  $\sim$ 11 m, respectively) compared to the locations close to the LM ( $\sim$ 3  $\Omega$ ·m and  $\sim$ 4 m, respectively). The depth to the Pleistocene clay layer (Figure 2-5b) generally decreases toward the LM from 15 m (PV11TEM1) to 4.5 m (near PV11TEM12).

Profile PV12 (Figure 2-6) revealed different subsurface and morphological patterns than those shown in PV11. Near LM (PV12TEM12 and PV12TEM13, elevations of 0.6 and 0.9 m, respectively) (Figure 2-6a), the FWL is absent, and the area is dominated by brine (108 PSU at PV12TEM12), as indicated by very low resistivity values (0.4  $\Omega \cdot m$ ). Farther inland, stations PV12TEM10, and PV12TEM11 exhibit moderately to very saline water (9– 18 PSU) with resistivities less than 3  $\Omega$ ·m and low elevation (1.2, 1.1, and 1 m, respectively) (Figures 2-6b and 2-6c). The lowest salinities, indicative of FWL, occur at the center of the island at stations PV12TEM6, PV12TEM7, and PV12TEM8 (0.7, 0.19, and 0.48 PSU, respectively) (Figure 2-6c), with corresponding high resistivities (35, 44, and 57  $\Omega$ ·m) and moderate elevation (1.92, 1.65, 1.02 m, respectively) (Figures 2-6a and 2-6b). Station PV12TEM5 showed a low resistivity value ( $\sim 3 \ \Omega \cdot m$ ) at a shallow depth ( $\sim 1.5 \ m$ ), as mapped through TDEM measurements and confirmed by water salinity data (Figures 2-6a and 2-6b). At sounding PV12TEM3, the thickness and the resistivity of the FWL were reported at 14.2 m and 26  $\Omega$ ·m, respectively. This region exhibits a moderate elevation of 2.75 m. Near the GOM coast (elevation: 1.9 m), a thin (1.4 m), FWL layer (resistivity of 28 Ω·m at PV12TEM1) was mapped.

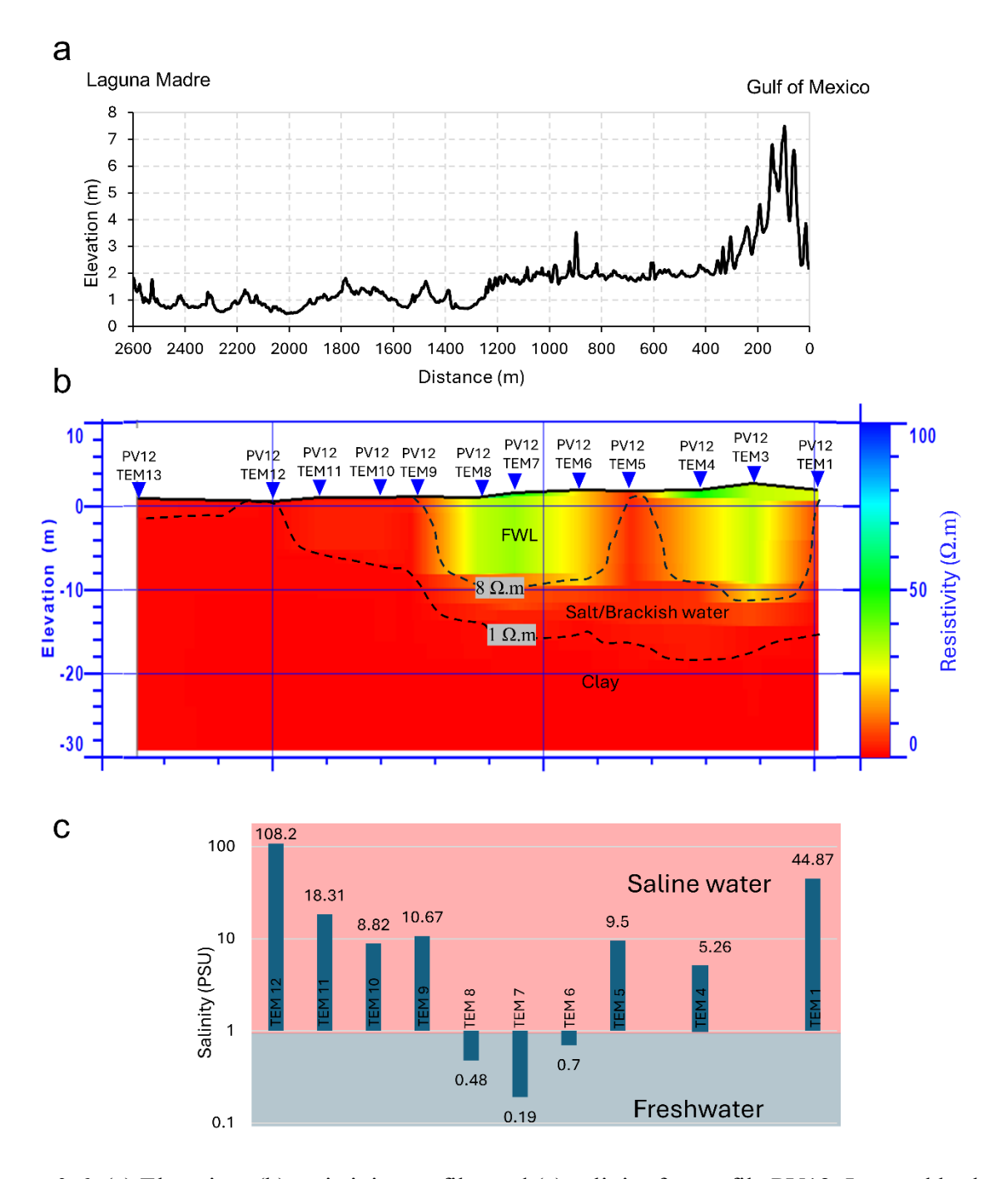


Figure 0-6. (a) Elevation, (b) resistivity profile, and (c) salinity for profile PV12. In panel b, the contour lines at 8 and 1  $\Omega$ .m delineate the approximate depths to the saltwater interface and the top of the Pleistocene clay layer, respectively.

TDEM data for profile PV13 along Bird Island Road (Figure 2-7), collected on January 26, 2024, followed a minor rain event (maximum precipitation of 3.6 cm on January 23). Stations PV13TEM6 through PV13TEM14, located inland close to LM (elevation: 1.6–3 m) (Figure 2-7a), exhibit low salinity (0.05–0.18 PSU) (Figure 2-7c) and relatively high resistivity (16–82  $\Omega$ ·m) values for the FWL. Conversely, stations PV13TEM3, PV13TEM4, and PV13TEM5, situated closer to the GOM coast and behind the foredune, display fresh and slightly saline water (0.94–1.78 PSU) with corresponding resistivity values between 11 and 52  $\Omega$ ·m. The deepest clay layer (10–19 m) underlies stations PV13TEM6 through PV13TEM9, coinciding with the lowest salinity values (0.13–0.18 PSU) and high resistivity values (28–82  $\Omega$ ·m) indicative of freshwater (Figures 2-7b and 2-7c). A distinct decrease in the thickness of the saline/brackish water layer was observed from the GOM side toward LM. Interestingly, stations PV13TEM9 and PV13TEM10 recorded low salinities of 0.2 and 0.08 PSU, despite low resistivity values ( $<20 \Omega$ ·m).

Profile PV3 (Figure 2-8) is located in developed areas north of Packery Channel, which connects the GOM and LM; it demonstrates the substantial impact of development (e.g., Packery Channel) on the presence of freshwater. The profile shows a significant reduction in the thickness of the FWL, which is restricted to less than 2 m within the high dune area. The elevation profile reveals that areas with elevations below 2 m (PV3TEM1, PV3TEM3, and PV3TEM4, with elevations 1, 1.2, and 1.5 m, respectively) (Figure 2-8a), and those more than 600 m away from both the GOM and LM, exhibit a complete absence of the FWL evidenced by the low resistivity values ( $<8 \ \Omega \cdot m$ ) (Figure 2-8b). The clay layer ranges in depth from 5 m near LM to 12 m near the GOM, generally dipping towards the GOM (Figure 2-8b).

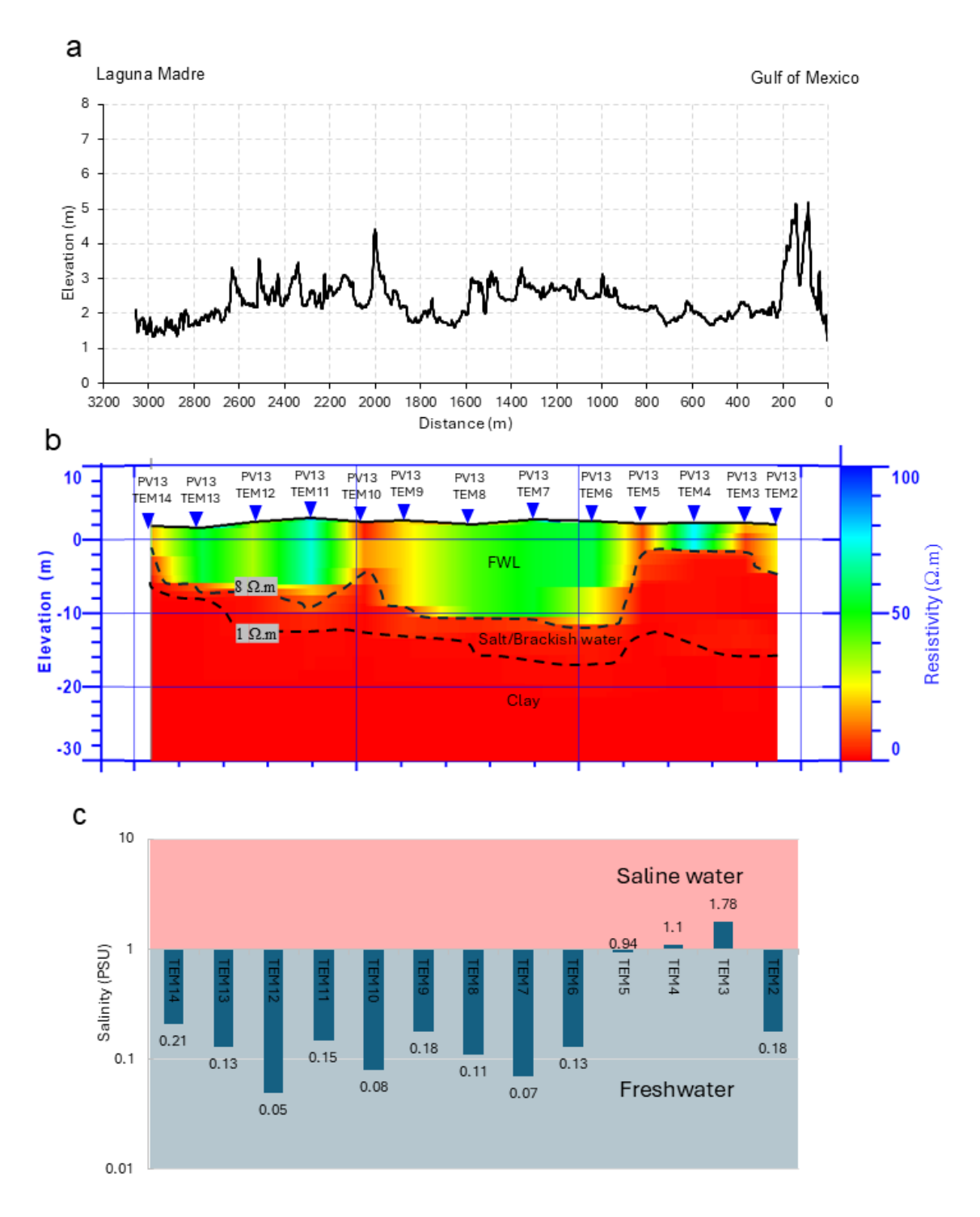


Figure 0-7. (a) Elevation, (b) resistivity profile, and (c) salinity for profile PV13. In panel b, the contour lines at 8 and 1  $\Omega$ .m delineate the approximate depths to the saltwater interface and the top of the Pleistocene clay layer, respectively.

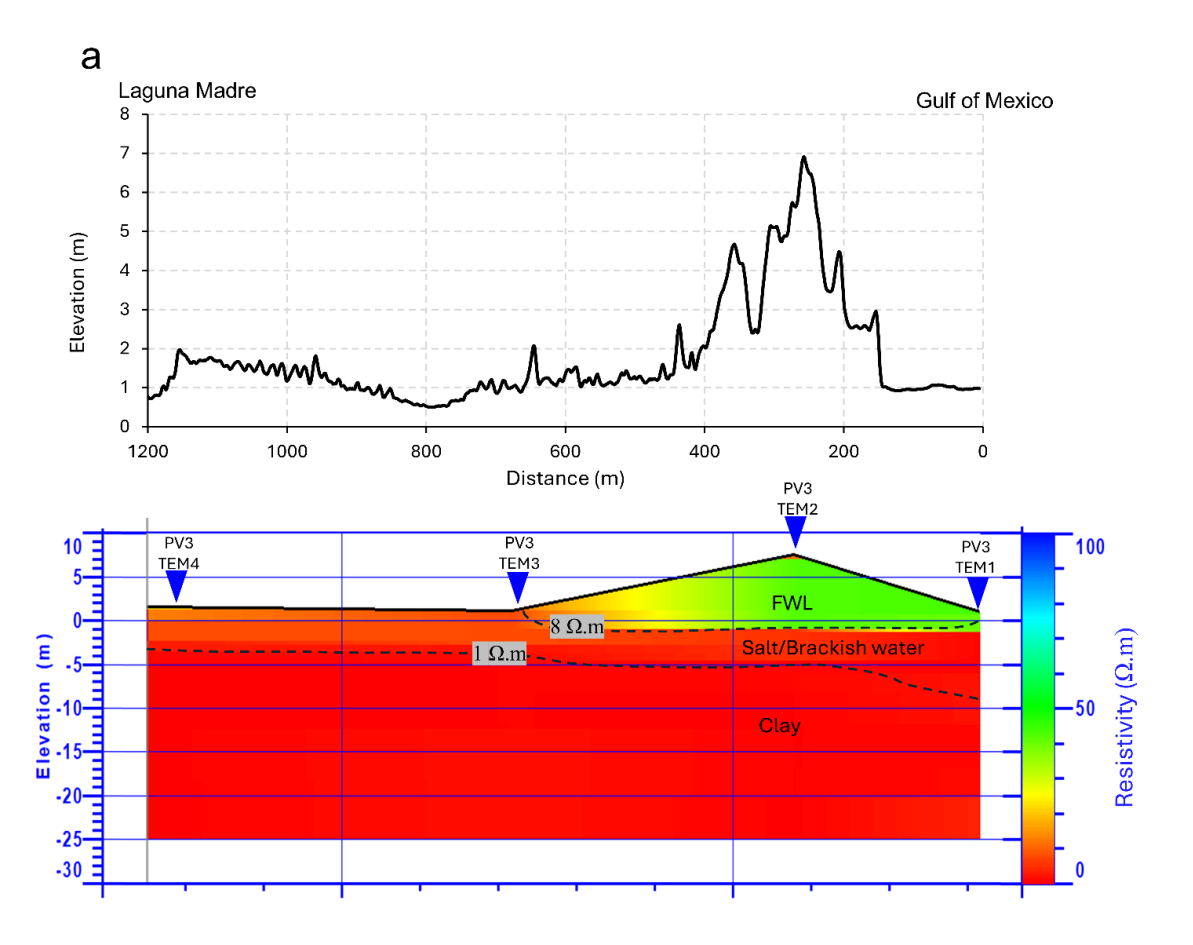


Figure 0-8. (a) Elevation and (b) resistivity profile PV3. In panel b, the contour lines at 8 and 1  $\Omega$ .m delineate the approximate depths to the saltwater interface and the top of the Pleistocene clay layer, respectively.

Profile PV4 (Figure 2-9), located in developed areas south of the Packery Channel and extending through a major housing development canal, also highlights the substantial impact of human development on FWLs. Sounding PV4TEM4, situated in an area with an elevation below 2 m and close to both Packery Channel (Figure 2-9a) and the housing canal, recorded no

presence of the FWL and exhibited low resistivity values of less than 8  $\Omega$ ·m. The profile shows the FWL under the high dune region (PV4TEM1-3), with thicknesses ranging from 4 to 10 m and high resistivity values (30–60  $\Omega$ ·m) (Figure 2-9b). Areas farther inland and within less developed regions demonstrated the presence of the FWL, with thicknesses ranging from 6 to 10 m. However, these areas had higher salinity, indicated by resistivity values of 25–30  $\Omega$ ·m, and were situated at elevations higher than 2 m.

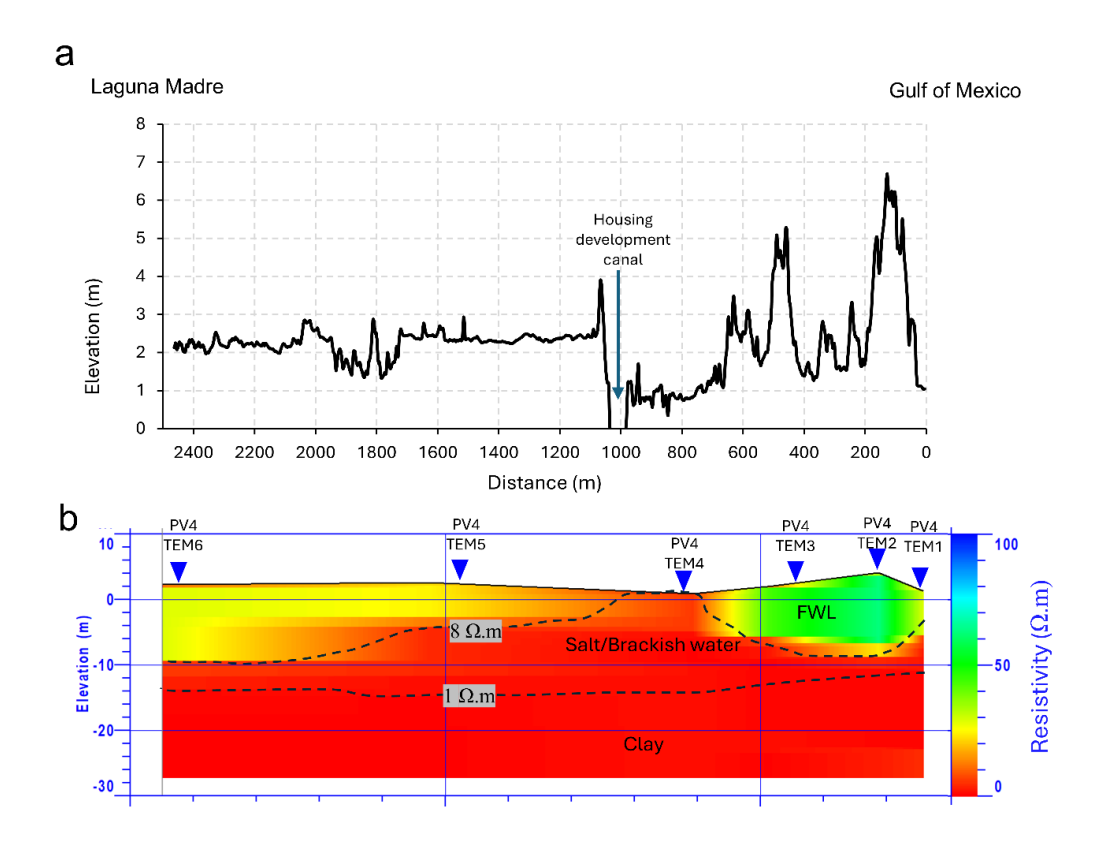


Figure 0-9. (a) Elevation and (b) resistivity profile PV4. In panel b, the contour lines at 8 and 1  $\Omega$ .m delineate the approximate depths to the saltwater interface and the top of the Pleistocene clay layer, respectively.

Profile P2–P2' (Figure 2-10) displays an along-shore N-S transect along the central axis of Padre Island. The depth to the Pleistocene clay layer increased from 10 m in the northern

portion to approximately 20 m in the southern portion (Figure 2-10b). Concurrently, a notable increase in the resistivity and thickness of the FWL was observed toward the south. The northern segment of the island, which coincides with an area of greater development, exhibited the most compromised FWL conditions. The FWL was significantly thinner, less than 9 m thick, and of higher salinity, as indicated by resistivity values below  $20~\Omega \cdot m$  (Figure 2-10b). In some locations within this developed zone, the FWL was absent; in others, it was extremely thin, measuring less than 5 m. In contrast, the southern portion of the profile, characterized by no development, exhibits more favorable conditions for lower salinity and thicker accumulation of FWL (~40  $\Omega \cdot m$  resistivity and ~12-m thickness).

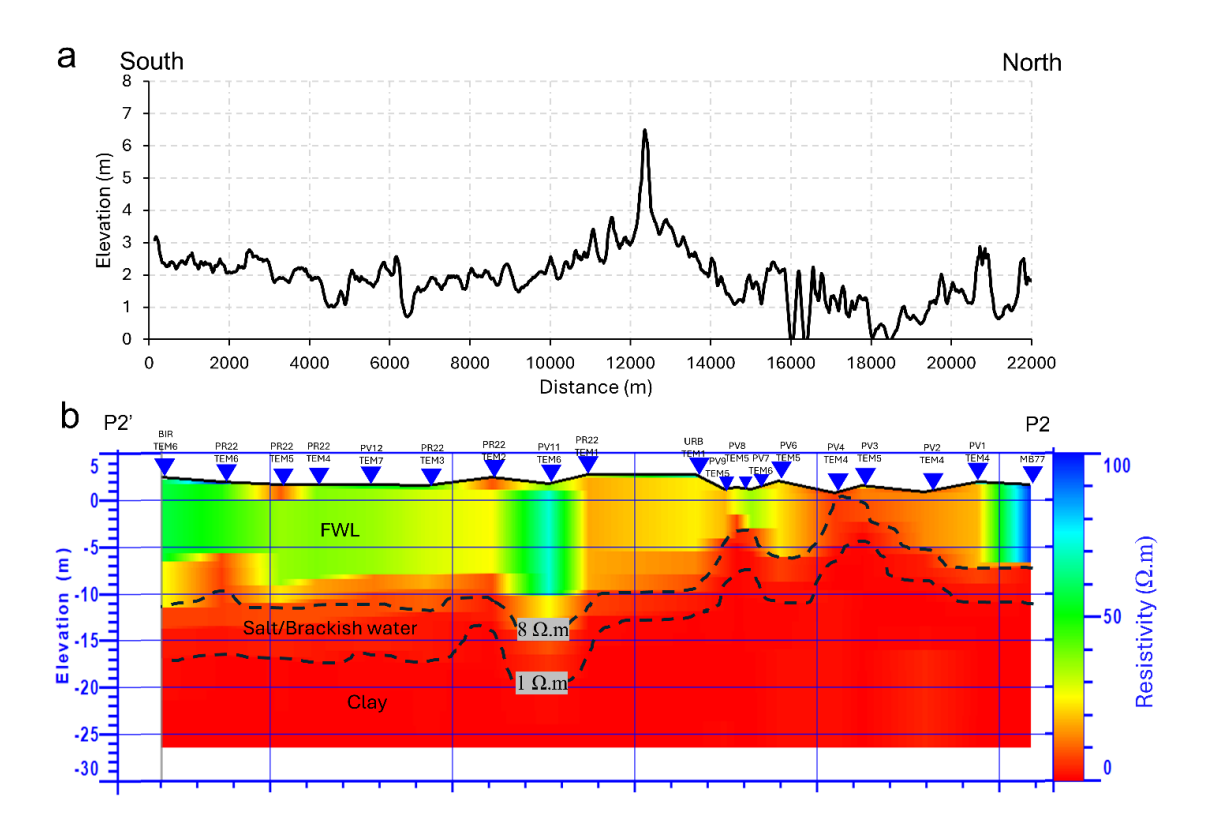


Figure 0-10. (a) Elevation and (b) resistivity profile P2–P2'. In panel b, the contour lines at 8 and 1  $\Omega$ .m delineate the approximate depths to the saltwater interface and the top of the Pleistocene clay layer, respectively.

To illustrate the spatial variability along both cross-shore and along-shore directions, the TDEM-derived resistivity and thickness of the FWL, thickness of the salt/brackish water layer and the depth to the Pleistocene clay layer were interpolated to generate isoresistivity, isopach, and depth maps as shown in Figure 2-11. Descriptive statistics for these layers over the entire study area are shown in Table 2-S2. The FWL (Layer 1) exhibited resistivity values of  $33 \pm 18 \ \Omega \cdot m$ , ranging from 8 to 82  $\Omega \cdot m$  (Figure 2-11a). Stations located within developed regions exhibit lower resistivity values ( $22 \pm 8 \ \Omega \cdot m$ ). The FWL thickness averaged  $8 \pm 5 \ m$ , with reduced values over the developed regions ( $7 \pm 3 \ m$ ) (Figure 2-11b). In the salt/brackish water-saturated layer (Layer 2), thickness varied according to location, averaging  $6 \pm 4 \ m$  (Figure 2-11c). The depth to the Pleistocene clay layer (Layer 3), ranged from less than 1 m to more than 22 m, with an average depth of  $13 \pm 5 \ m$ . The clay layer in the study area generally dips toward the GOM, with the deepest sections located near the GOM and the shallowest parts near LM (Figure 2-11d). The Pleistocene clay layer was notably shallow beneath the developed area, with an average depth of  $5 \pm 2 \ m$ , and gradually deepens southward along the island, reaching depths exceeding 15 m.

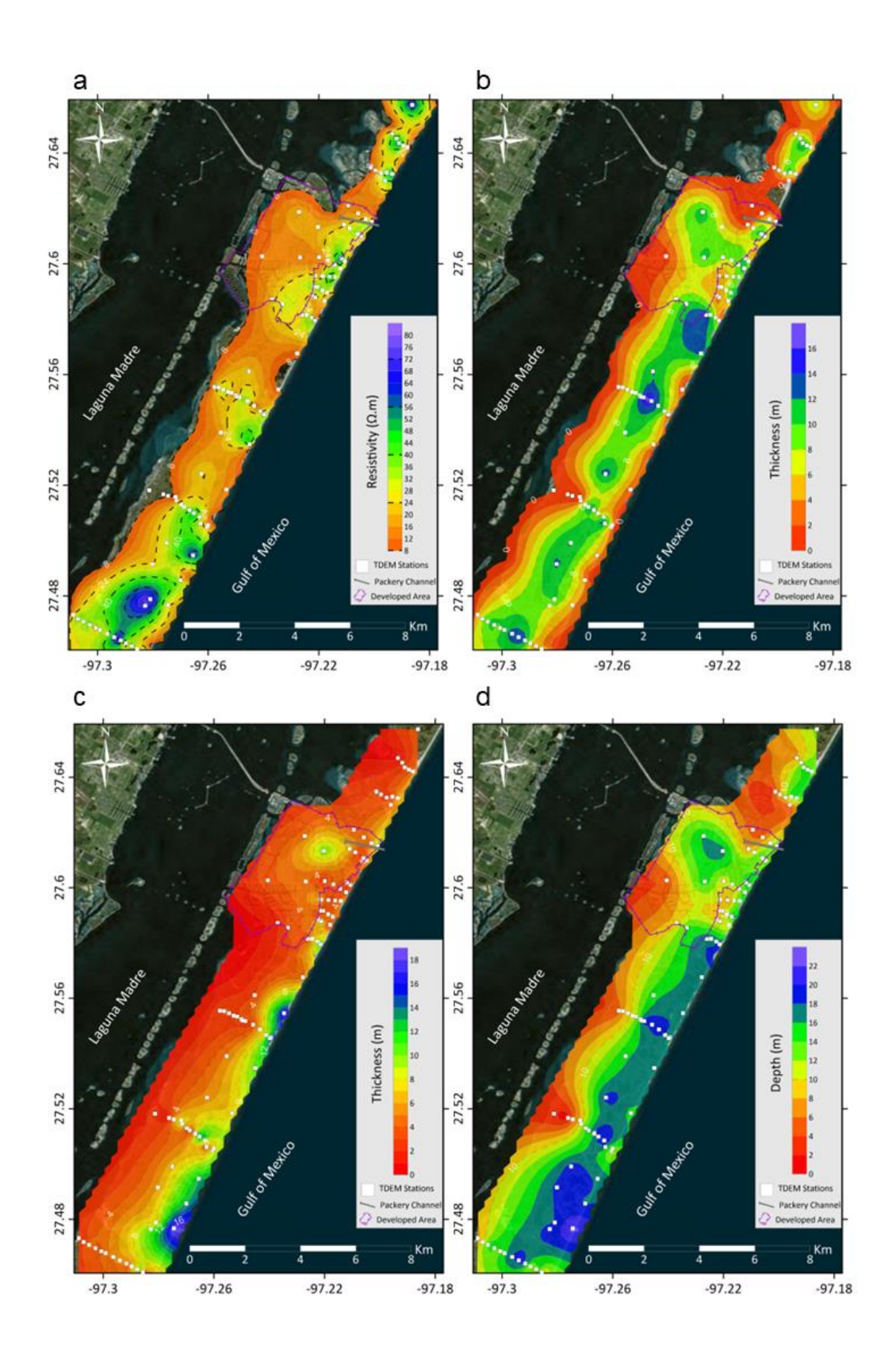


Figure 0-11. Spatial variability in the hydrogeological properties of Padre Island: (a) resistivity of FWL, (b) thickness of FWL, (c) thickness of brackish/saline water, and (d) depth to the Pleistocene clay layer.

# 2.5.3 Statistical Analysis of Subsurface and Topographic Conditions

Over the study area, the island was divided into four main geomorphologic zones based on elevation and proximity to the GOM and LM, as shown in Figure 2-1c. Zone 1 represents the beach, Zone 2 includes the foredune, Zone 3 consists of the vegetated barrier flats, and Zone 4 encompasses the back dune and wind tidal flats. Over these zones, we studied the FWL's resistivity and thickness, the clay layer's depth, the island's elevation, and the dune volume (Figure 2-12a) to draw conclusions based on each zone. Table 2-S3 includes descriptive statistics for these parameters over each zone. To investigate their mutual relationships, three sets of correlation values were calculated for each zone, comparing the FWL resistivity and thickness and the island's elevation, dune volume, and clay depth (Figure 2-12b).

Over Zone 1, the beach zone, a total of 17 TDEM stations were collected, with an average elevation of  $1.8 \pm 0.5$  m. The resistivities of the FWL and clay layer averaged  $32 \pm 16~\Omega$ ·m and  $0.4 \pm 0.3~\Omega$ ·m, respectively. The thickness of the FWL was  $5 \pm 2$  m, while the depth to the clay layer averaged  $15 \pm 4$  m (Figure 2-12a). The thickness of the FWL showed no correlation with elevation but was strongly correlated with dune volume (r = +0.51; p-value: 0.05).

In the foredune, Zone 2, a total of 23 TDEM stations were acquired, with an average elevation of  $3 \pm 1.3$  m (Figure 2-12a). The resistivities of the subsurface layers averaged  $36.9 \pm 1.6 \ \Omega \cdot m$  for the FWL and  $0.45 \pm 0.33 \ \Omega \cdot m$  for the clay layer. The thickness of the FWL

averaged  $10 \pm 2.7$  m. The average depth to the clay layer was  $13 \pm 3.7$  m. The FWL resistivity showed no significant correlation with elevation, dune volume, or depth of the clay layer (Figure 2-12b). The FWL thickness, however, exhibited a strong correlation with elevation (r = +0.58, p-value: 0.00) and the depth to the clay layer (r = +0.85, p-value: 0.00).

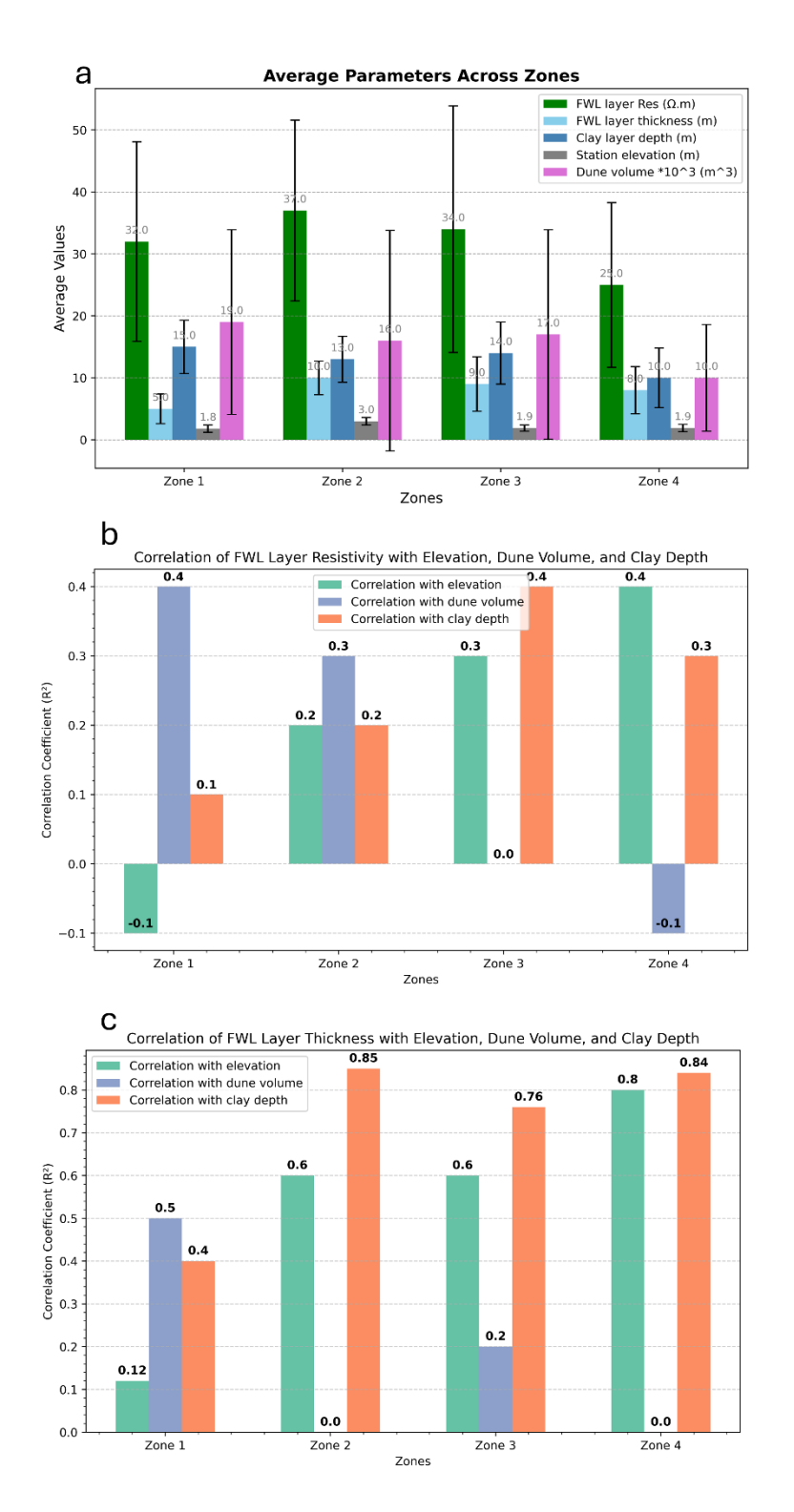


Figure 0-12. Geomorphological zones of Padre Island along with subsurface and surface conditions: (a) average resistivity and thickness of FWL, dune volume, and depth to the clay layer. Error bars represent the standard deviation in each parameter. (b) Correlation coefficients

between the FWL resistivity and elevation, dune volume, and clay layer depth. (c) Correlation coefficients between the FWL thickness and elevation, dune volume, and clay layer depth. Zone 1 is the beach, Zone 2 is the foredune, Zone 3 is the vegetated barrier flats, and Zone 4 is the back dune and wind tidal flats.

The vegetated barrier flats, Zone 3, with 39 TDEM stations, were the largest area sampled, exhibiting an average elevation of  $1.8 \pm 0.6$  m (Figure 2-12a). The subsurface resistivities averaged  $34 \pm 20~\Omega$ ·m for the FWL and  $0.28 \pm 0.27~\Omega$ ·m for the clay layer. The FWL had an average thickness of  $9.3 \pm 4.4$  m. The average depth to the clay layer was  $14 \pm 5$  m. The FWL resistivity had a strong positive correlation with station elevation (r = +0.31; p-value: 0.07; Figure 2-12b). Dune volume, however, showed no significant correlation with FWL resistivity. FWL thickness showed a strong positive correlation with station elevation (r = +0.64; p-value: 0.00). The FWL resistivity showed a significant positive correlation with the depth of the clay layer (r = +0.38; p-value: 0.02) and an even stronger correlation was observed between the FWL thickness and the depth of the clay layer (r = +0.76; p-value: 0.00).

Zone 4, 22 TDEM stations were measured in the back dune and wind tidal flats, with an average elevation of  $1.9 \pm 0.68$  m (Figure 2-12a). The subsurface resistivities averaged  $24.6 \pm 13~\Omega$ ·m for the FWL and  $0.22 \pm 0.14~\Omega$ ·m for the clay layer. The FWL had an average thickness of  $8 \pm 3.3$  m. The average depth to the clay layer was  $10 \pm 4.8$  m. The FWL resistivity positively correlated with station elevation (r = +0.43; p-value: 0.10; Figure 2-12b). On the other hand, the dune volume demonstrated no correlation with FWL resistivity. In this zone, the FWL thickness exhibited the strongest correlation with station elevation among all zones (r = +0.82; p-value:

0.00). The depth of the clay layer exhibited a negligible correlation with FWL resistivity, but a strong positive correlation with FWL thickness (r = +0.84; p-value: 0.00).

## 2.6 Discussion

### 3.1 Uncertainty Analysis

The subsurface of the island was characterized by three distinct geoelectrical layers: a freshwater-saturated sand layer (the FWL) with resistivities typically exceeding 8  $\Omega$ ·m and reaching up to 100  $\Omega$ ·m; a salt/brackish-water saturated sand layer with a range of resistivities between 1 and 8  $\Omega$ ·m; and a saltwater-saturated Pleistocene clay layer with resistivities generally less than 1  $\Omega$ ·m. These resistivity ranges align with findings from previous studies conducted in both laboratory settings and coastal environments (El-Kaliouby and Abdalla, 2015; Kalisperi et al., 2018; Pondthai et al., 2020; Shevnin et al., 2007). Notably, the RMS misfit for the soundings does not exceed 6%. The low RMS values and close agreement between equivalent and best-fit models in the inversion process indicate that the results are robust, and the quality of the collected data is high.

Due to the shallow depth of the water table on the island (average of 0.5 m), which cannot be resolved from the TDEM data, the FWL thickness is estimated with an uncertainty of  $\pm 0.5$  m. Conversely, the highly conductive saline water zone and underlying clay layer were well-resolved, with resistivity and depth uncertainties less than 10%. TDEM-derived depths to the clay layer (Layer 3) generally agreed strongly with seven of eight well measurements, with discrepancies typically less than  $\pm 1.5$  m. However, at station PV13TEM5, a significant discrepancy exceeding 5 m was observed. This discrepancy may be due to local geological

heterogeneity, such as unexpected variations in lithology or subsurface structures, particularly given the potential influence of regional variations within the 300-m distance between the TDEM station and the well location.

The salinity measurements obtained using the YSI ProDSS have an uncertainty of  $\pm 1.0\%$  of the reading or  $\pm 0.1$  ppt, whichever is greater. The vertical accuracy of the high-resolution DEM, which is used for extracting elevation and calculating dune volume, is characterized by a root mean square error (RMSE) of 0.53 m. The relative error in dune volume is therefore dependent on the ratio of the RMSE to the average dune height; smaller dunes will have a larger relative error in volume than larger dunes.

# 3.2 Morphology and Distribution of the FWL

Barrier islands have limited space for freshwater storage because they are narrow and, in our case, because a shallow, low-permeability clay layer is present. These factors contribute to the shallow geometry of the FWL, as well as a short residence time for the water flowing through it. The average residence time of groundwater on barrier islands is approximately 1 year (Panthi et al., 2024), which is significantly shorter than the residence times observed in continental coastal aquifers, such as the ~95 years reported by Russoniello et al. (2016). This short residence time reflects the dynamic nature of the FWL on barrier islands.

The recharge rate, which fluctuates seasonally, significantly influences the size and shape of the FWL. This was observed along profiles PV11 and PV13, which were collected after a rain event. These profiles exhibited a thicker and more consistent FWL, even near LM, indicating

freshwater discharge towards the lagoon. Stations PV11TEM1 and PV11TEM3, located near the GOM, and PV11TEM12 near LM, exhibited significant saltwater intrusion effects.

In contrast, profile PV12, collected during a drought, displayed a nonuniform FWL with saltwater intrusion extending more than 1 km from the LM side into the island's center, and a saltwater upconing was observed at 0.7 km (PV12TEM5) from the GOM side. At sounding PV12TEM3, the thickness and the resistivity of the FWL were reported at 14 m and 26  $\Omega$ ·m, respectively. This region exhibits a moderate elevation (>2 m) of 2.75 m. Near the GOM coast (elevation: 1.9 m), a thin (1.4 m) FWL layer (resistivity of 28  $\Omega$ ·m at PV12TEM1) was mapped. This suggests minimal freshwater presence due to saltwater intrusion. Freshwater samples and TDEM measurements confirm that the barrier island's FWL responds quickly to recharge events, with an average water table depth of 0.5 m. These findings align with the observations of Panthi et al. (2024), who noted that shallow water tables on barrier islands respond rapidly to recharge events. Interestingly, along profile PV13, stations PV13TEM9 and PV13TEM10 recorded a low salinity of 0.2 and 0.08 PSU, despite low resistivity values (<20  $\Omega$ ·m). This suggests that saltwater upconing is present close to the surface below the water table, as indicated by the resistivity values.

The depth to the Pleistocene clay layer (Figures 2-5b, 2-6b, and 2-7b) generally decreases toward the LM, ranging from approximately 20 m near the GOM to less than 5 m near the LM. This observed dip is consistent with the regional geological framework, influenced by glacio-eustatic sea-level fluctuations and paleo-drainage basin characteristics (Winker, 1979). This regional dip is further supported by previous studies, such as Shideler (1986), who reported a dip of approximately 5 m per kilometer. Given the average island width in the study area of 2.8 kilometers, this regional dip would result in an expected depth difference of approximately

14 m across the island, aligning with the observed trend in our data (15m). Figures 2-5b, 2-6c, and 7b illustrate this regional dip in the clay layer, providing visual support for the observed depth variations across the island. The thickness of the FWL exhibited a strong positive correlation with the depth to the underlying Pleistocene clay layer, with correlation coefficients ranging from 0.4 to 0.85 across different zones (Figure 2-12c).

FWL is strongly influenced by sediment permeability, with low-permeability layers limiting their horizontal extent and often resulting in asymmetrical shapes, as observed in our study (Figures 2-5b, 2-6b, and 2-7b) and other studies of developing barrier islands (Holt et al., 2019). This highlights the essential role of low-permeability layers in controlling freshwater distribution on barrier islands. It also emphasizes the importance of detailed investigations to understand their spatial characteristics and impact on freshwater resources (Babu et al., 2018). Furthermore, sustainable management of freshwater resources is complicated by low-permeability layers, which can increase the risks of salinization under conditions of reduced recharge or increased groundwater extraction (Babu et al., 2018).

Two primary locations consistently exhibited saltwater upconing away from the saltwater bodies along the three profiles (PV11, PV12, and PV13). The first zone, 1,000 m from LM, aligns with a low-elevation, seasonally flooded brackish marsh. The low-lying topography in this area creates a shallow zone that facilitates direct evaporation from the water table, thereby concentrating salts near the surface (Geng and Boufadel, 2017). This feature likely serves as a conduit for saltwater intrusion, with the marsh acting as a pathway for hypersaline lagoon water to flow into the island's interior. Density differences between the FWL and saltwater cause convective flow, where denser saline plumes sink and displace the freshwater, resulting in brackish to saline conditions. Another contributing factor could be saline water intrusion from

LM across a low-lying marsh feature, driven by wind-induced fluctuations in lagoon water levels (ranging from 0.6 to 0.9 m) (TPWD, 2024). The varying salinity within the marsh (brackish to fresh) reflects the dynamic interaction between hypersaline lagoon water, freshwater inputs, and evapotranspiration. Regardless of the distance from LM (up to 1 km), lower elevation areas are more prone to a lack of FWL, highlighting the significant role of elevation in controlling their distribution.

The second saltwater upconing zone, located approximately 700 m from the GOM, was observed across all recorded profiles in the undeveloped area. For example, the lower resistivity at TDEM stations PV11TEM4, PV12TEM5, and PV13TEM5 ( $\sim$ 10  $\Omega$ ·m) can be attributed to surface water ponds (elevation: 2 m) with high evaporation rates. Geng et al. (2017) found that evaporation from a shallow water table significantly increases pore water salinity, while Werner et al. (2013) attributed saltwater upconing to a combination of evapotranspiration and mechanical drainage processes.

In all profiles measured in the pristine area (PV11, PV12, and PV13), the maximum FWL thickness occurs at the island's center. This greater thickness and higher resistivity of the FWL is attributed to several factors: the increased distance from the GOM and LM, which are the primary sources of saltwater intrusion; a deeper clay layer that provides more space for freshwater storage (Holt et al., 2019); and the relatively higher elevation, which also provides more accommodation space and enhances the freshwater recharge (Cozzolino et al., 2017).

Anthropogenic activities, such as dune destruction; the construction of buildings, roads, and housing developments; and the creation of canals and waterways, significantly affect the freshwater resources on barrier islands (Abdelrehim et al., 2023; Cozzolino et al., 2017; Schneider and Kruse, 2006; Werner et al., 2013). Some infrastructure, like roads and buildings,

reduce freshwater recharge and increase runoff, while others, such as housing development, canals, and waterways, introduce saline water into the island's interior, raising the salinity of the FWL and expanding the saltwater intrusion zone. Areas near these developments, particularly in the northern part of the study area (profiles PV3 and PV4) (Figures 2-8, 9, and 11), show a complete absence or significantly reduced thickness and higher salinity of the FWL, highlighting the negative impact of these activities.

Profile P2–P2' (Figure 2-10) illustrates a southward deepening of the Pleistocene clay layer, ranging from approximately 9 m in the north to 19 m in the south. This deepening of the clay layer is reflected in the thickness and resistivity of the overlying FWL. The FWL under the undeveloped area exhibits an average thickness of 12 m and a resistivity of approximately  $40~\Omega\cdot m$ . In contrast, the FWL beneath developed areas displays significantly reduced characteristics, with a markedly thinner thickness (< 5 m) and lower resistivity (~10  $\Omega\cdot m$ ), highlighting the detrimental impact of development on the FWL. This underscores the need for improved management and development strategies, considering the island's limited freshwater resources.

### 3.3 Broader Implications and Challenges

Freshwater management on barrier islands presents significant challenges due to the complex interplay of factors that influence the presence, quality, and dynamics of this vital resource. Our study provides insights into these factors, highlighting their roles in shaping the FWL on complex sandy barrier islands in the world. Climate change is expected to exacerbate these challenges, with projected increases in droughts, temperatures, and evapotranspiration rates, which could reduce freshwater recharge and elevate salinity levels in the FWL. The

findings of this study underscore the importance of subsurface geology, surface topography, and anthropogenic activities in controlling the FWL. By understanding the interactions among these factors, coastal communities can better strategize to mitigate the potential shrinking of FWLs on barrier islands and protect freshwater resources in the future. Specifically, low-lying barrier islands such as Padre Island, where both topography and geology limit the FWL's growth and its capacity to adapt to rising sea levels, are at higher risk of resource depletion (Panthi et al., 2024). Furthermore, spatial and temporal variability in salinity and other biogeochemical changes within near-surface aquifers—especially on a seasonal scale—can significantly influence the mobility of contaminants, redox reactions, and nutrient cycling. Over time, these dynamics may result in cumulative effects that could have cascading ecological consequences, as highlighted by Tully et al. (2019).

This study faces certain challenges. This study relied on the available DEM collected in 2018 and limited GNSS measurements for characterizing surface topography. However, certain areas, such as the foredune and other dune locations, undergo dynamic changes, particularly after storms, which can lead to shifts in elevation and topographic features over time. These temporal variations mean that a more recent DEM could enhance the correlation between surface and subsurface features, providing a more accurate representation of topographic changes and their effects on the FWL. However, a significant correlation between the DEM and the field-collected elevations was observed.

In addition, future research could benefit from integrating remote sensing techniques to capture temporal changes in the island's freshwater resources. For instance, the Normalized Difference Vegetation Index could provide insights into vegetation health and its correlation with FWL dynamics. Similarly, tracking land use changes and land surface temperature variations

would help understand how human activities and environmental factors influence the freshwater resources on barrier islands over time.

The resolution of the TDEM data was limited at shallow depths, preventing direct estimation of the water table depth in some areas. This limitation was addressed through water sampling and direct measurements of the water table depth. However, for future studies, using short ground-penetrating radar profiles would offer a noninvasive technique to better locate the depth of the water table, particularly in protected areas where drilling wells and collecting water samples may not be feasible. Incorporating these additional techniques would improve the overall accuracy and comprehensiveness of subsurface characterization, especially in areas where access is restricted or challenging.

#### 2.7 Conclusions

This study used high-resolution geophysical, hydrogeological, and topographical surveys to investigate the factors controlling the characteristics of the FWL on Padre Island, the world's longest barrier island, in southern Texas, United States. The results offer new insights into the relationship between surface geomorphology, subsurface geological conditions, and the characteristics of the limited freshwater resources in such a delicate environment.

Our findings identified three distinct geoelectrical layers within the island's subsurface: FWL extending up to 18 m deep, a salt/brackish water layer with a thickness of 1–19 m, and a Pleistocene clay layer forming the basal sequence at depths of 1–23 m. The water salinity of the surface layer varied significantly across the island, from hypersaline water exceeding 100 PSU to

freshwater with salinity levels below 1 PSU. The average resistivity of the FWL on the island was  $33 \pm 18 \ \Omega \cdot m$ , with a range of 8–82  $\Omega \cdot m$ , reflecting variations in freshwater salinity.

The study identified five primary controls on the FWL's salinity and thickness:

- Proximity to development: Developed areas, particularly near the Packery Channel and major housing development canals, showed lower resistivity (22 ± 8 Ω·m) and thinner FWL (7 ± 3 m) due to reduced recharge rates, increased runoff, and enhanced pathways for saltwater intrusion.
- Distance from the GOM and LM: Areas closer to these bodies of water experienced greater saltwater intrusion, reducing the FWL salinity (30 ± 17 Ω·m) and thickness (5 ±4 m).
- Island surface elevation: Locations above 2 ± 0.5 m in elevation supported thicker (9 ± 4 m) and fresher (34 ± 20 Ω·m) FWLs. Significant correlations of +0.31 and +0.43 were observed between surface elevation and the resistivity of the FWL over the vegetated barrier flats and the wind tidal flat zones, respectively. Significant correlations of +0.58, +0.64, and +0.82 were observed between elevation and the thickness of FWL over the foredune, the vegetated barrier flats, and the wind tidal flat zones, respectively. Higher elevations host thicker, lower-salinity FWLs, while areas with lower elevation (<1 m) are dominated by saltwater regardless of proximity to the GOM or LM.
- **Dune volume**: Dune volume positively correlated (r: +0.51) with the thickness of the FWL over the beach zone; locations with higher (16,800 m<sup>3</sup>) dune volumes supported

thicker ( $10 \pm 2.7$  m) FWLs. This correlation suggests that recharge rates are higher in areas with greater dune volumes.

• Depth to the Pleistocene clay layer: We found significant correlations of +0.38 between the resistivity of FWLs and the depth to the clay layer over the vegetated barrier flats. Significant correlations of +0.85, +0.76, and +0.84 were observed between the thickness of FWLs and the depth to the clay layer over the foredune, the vegetated barrier flats, and the wind tidal flat zones, respectively. Areas with deeper clay layers (13 ± 4 m) exhibited thicker (10 ± 3 m) and more resistive (37 ± 145 Ω·m) FWL. Deeper clay layers allowed for greater accommodation space for thicker FWL, while shallower clay layers made areas more vulnerable to saltwater intrusion and drought.

The interaction between surface topography, subsurface geology (sediment type and thickness/depth), and development activities has significantly shaped the FWL dynamics on Padre Island. These findings highlight the critical need for responsible management and conservation of freshwater resources and the ecosystems that depend on them. Future conservation efforts should focus on mitigating the impacts of development and safeguarding the FWL from further degradation. This research provides a valuable framework for studying similar barrier islands worldwide, guiding the development of effective management strategies for these vulnerable coastal systems. The insights gained from this study will support better resource planning and direct future research efforts to ensure the sustainability and protection of freshwater resources in fragile barrier island environments.

### 2.8 Supplementary Material:

This supplementary material includes three figures and three tables to provide additional context and detailed analysis for the study:

Figure S1: Illustrates the principles of operation of the TDEM technique. A typical TDEM system employs a current waveform, I(t), that starts with a slow rise to a steady value (I<sub>0</sub>) followed by a rapid shutoff, resembling a linear ramp (Figure 2-S1a). When this current passes through the transmitter (T<sub>X</sub>) loop, it generates a primary magnetic field directly proportional to, and in phase with, the T<sub>X</sub> current. Faraday's law of induction dictates that an impulsive electromotive force is also induced. This electromotive force is proportional to the negative rate of change of the primary magnetic field over time. During the current shutoff phase, the induced electromotive force drives eddy currents within the conductive ground (Figure 2-S1b). After the current ramp terminates, the electromotive force vanishes, and the eddy currents begin to decay due to Ohmic dissipation. This decay process produces a weak secondary magnetic field ( $B^{S}(t)$ ) whose strength diminishes with time. The receiver  $(R_X)$  coil measures the rate of change of this decaying secondary magnetic field with time (Figure 2-S1c). In many TDEM systems, R<sub>X</sub> voltage measurements are taken during the "off-time" after the T<sub>X</sub> current has stopped. The advantage of off-time recording is that it avoids masking the relatively weak secondary signal with the significantly stronger primary signal present during the "on-time" when the T<sub>X</sub> current is flowing.

Figure 2-S2: Displays a lithological column for the top 25 m of North Padre Island, originally documented by Garrison (1986). This column serves as a reference for subsurface lithologies and their respective ages.

Figure 2-S3: Illustrates a statistical analysis of the equivalent models derived for the three subsurface layers across all TDEM data. This analysis highlights variations among the equivalent models relative to the best-fit model, offering insights into uncertainties in the inverted results.

Table 2-S1: Lists detailed metadata for all TDEM stations, including exact location, elevation, collection date, and water sample availability at each station.

Table 2-S2: Summarizes overall statistics (mean, standard deviation, range, minimum, and maximum) for the three subsurface layers and station elevations across all TDEM stations.

Table 2-S3: Presents zone-specific statistics (mean, standard deviation, range, minimum, and maximum) for the Island. These zone-specific values, categorized by elevation and proximity to water bodies, provide more constrained insights compared to the overall statistics in Table 2.

This information complements the main findings, enhancing the study's transparency and robustness.

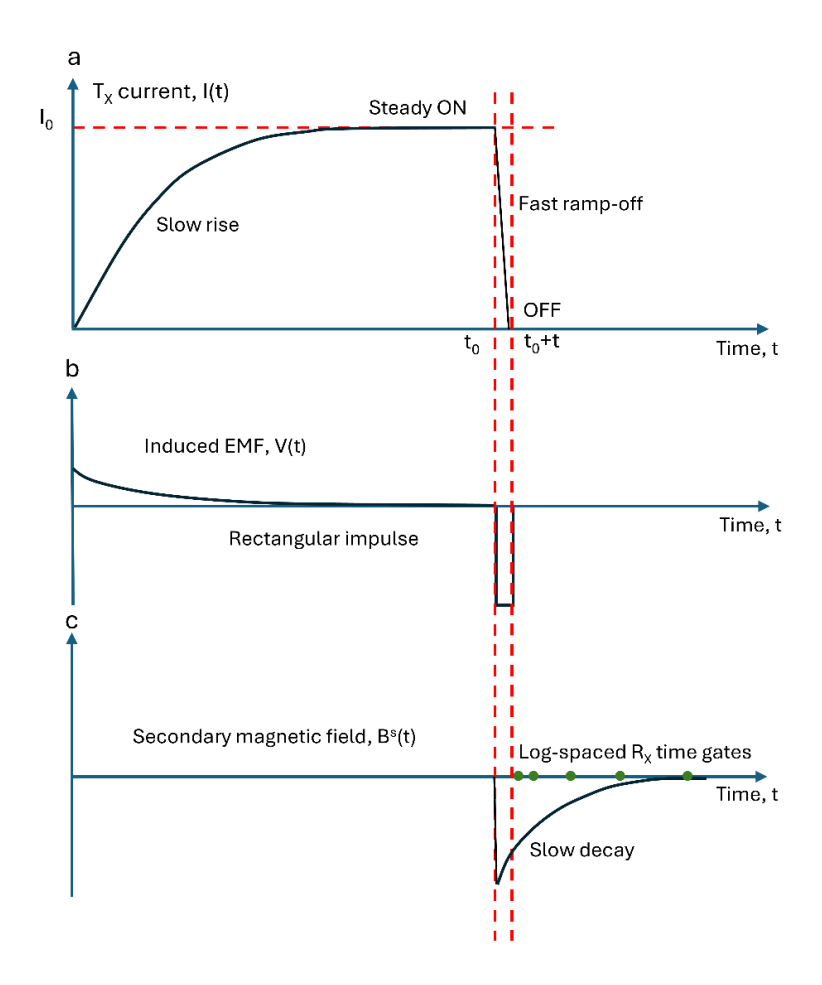


Figure S1. TDEM method's operating principle. (a) Transmitter  $(T_x)$  current I(t) gradually rises to a steady state  $(I_0)$  before abruptly shutting off. (b) Induced electromotive force voltage V(t) proportional to the rate of change of the primary magnetic field. (c) Decay of the secondary magnetic field BS(t) caused by dissipating eddy currents in the subsurface (adopted from Everett (2013).

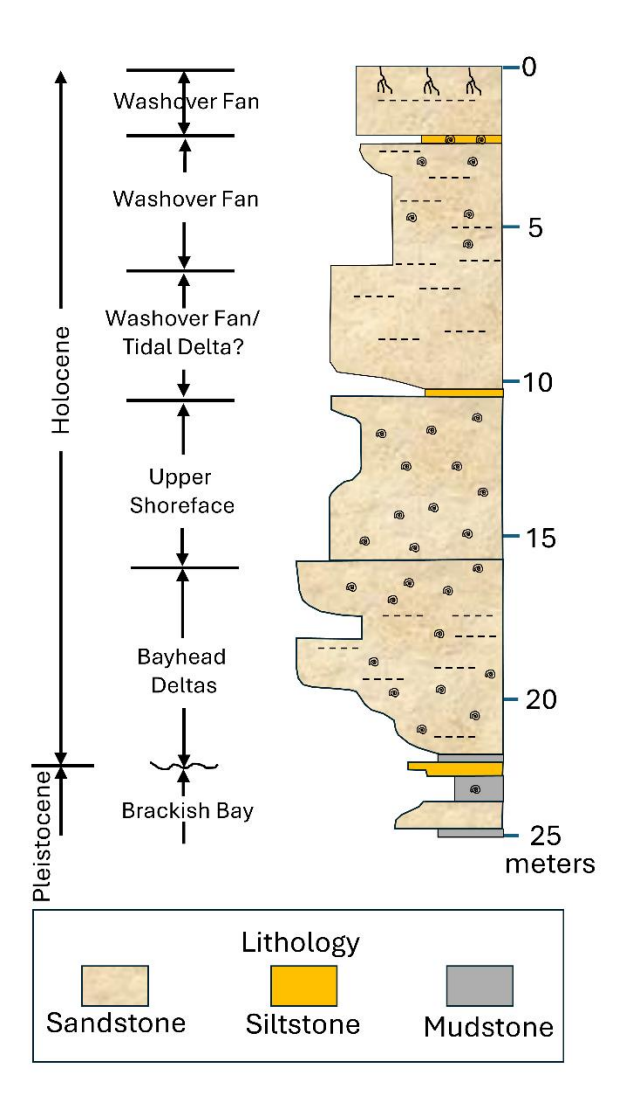


Figure S2. Core description illustrating the lithology and age of subsurface layers from the North Padre Island Core EE, collected by Garrison (1986) at Crane Island on the bay side of Padre Island (adapted from (Garrison and McCoy, 2007)).

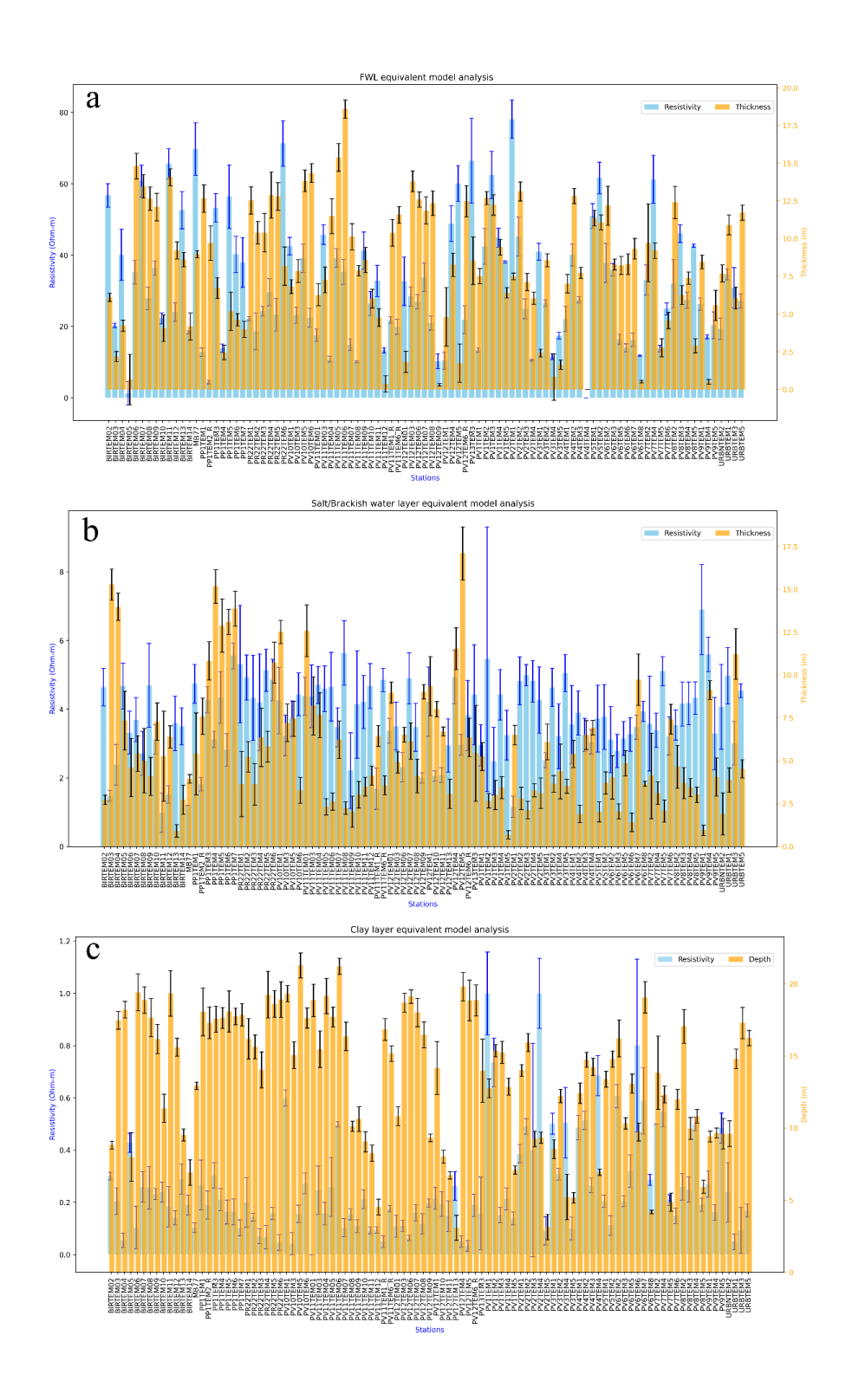


Figure S3. Statistical analysis of the equivalent models for the three subsurface layers, displaying the average resistivity and thickness/depth of each layer, with standard deviation as an error bar

to represent the uncertainty in subsurface properties: a) FWL, b) Salt/Brackish Water Layer, c) Clay Layer.

Table S.1 Coordinates, elevation, and water sample collection details for TDEM stations (cells with a checkmark "✓" represent locations where samples were collected, while cells marked with a "x" indicate where no samples were collected).

TDEM Station	Easting	Northing	Elevation (m)	Date	Water Sample	TDEM Station	Easting	Northing	Elevation (m)	Date	Water Sample
PV13TEM02	669534.6	3038576.2	2.1	26- Jan- 24	<b>√</b>	PV12TEM13	669751.2	3045007.2	0.9	9- May- 24	<b>✓</b>
PV13TEM03	669410.1	3038647.8	2.3	26- Jan- 24	<b>✓</b>	PV13TEM3	669843.0	3040647.0	2.0	15- Sep- 23	*
PV13TEM04	669210.7	3038763.5	2.1	26- Jan- 24	✓	PV1TEM1	678760.0	3058870.0	1.9	9- Aug- 23	*
PV13TEM05	669002.7	3038868.0	2.2	26- Jan- 24	✓	PV1TEM2	678614.0	3058943.0	2.6	18- Aug- 23	*
PV13TEM06	668813.3	3038980.8	2.5	26- Jan- 24	<b>✓</b>	PV1TEM3	678464.0	3059030.0	2.5	18- Aug- 23	*
PV13TEM07	668577.0	3039110.2	2.8	26- Jan- 24	<b>✓</b>	PV1TEM4	678373.0	3059217.0	2.1	18- Aug- 23	*
PV13TEM08	668339.2	3039243.5	2.1	26- Jan- 24	<b>✓</b>	PV1TEM5	678212.0	3059400.0	1.2	9- Aug- 23	*
PV13TEM09	668065.4	3039389.5	2.6	26- Jan- 24	✓	PV2TEM1	678230.0	3057800.0	1.7	9- Aug- 23	*
PV13TEM10	667906.1	3039469.2	2.4	26- Jan- 24	<b>✓</b>	PV2TEM2	678037.0	3057849.0	4.1	18- Aug- 23	*
PV13TEM11	667698.9	3039587.2	3.0	26- Jan- 24	✓	PV2TEM3	677837.0	3057810.0	1.2	9- Aug- 23	×

PV13TEM12	667468.9	3039713.8	2.5	26- Jan- 24	<b>✓</b>	PV2TEM4	677632.0	3057930.0	0.9	9- Aug- 23	×
PV13TEM13	667271.6	3039826.2	1.6	26- Jan- 24	<b>√</b>	PV2TEM5	677466.0	3058040.0	0.9	9- Aug- 23	×
PV13TEM14	667096.5	3039988.0	1.8	26- Jan- 24	<b>√</b>	PV3TEM1	677545.0	3055870.0	1.0	9- Aug- 23	×
MB77	678909.0	3060564.0	1.5	6- Jan- 24	×	PV3TEM2	677323.0	3055970.0	6.2	18- Aug- 23	×
PP1TEM1	674946.0	3050560.0	2.4	30- Jul- 23	×	PV3TEM4	677044.0	3056200.0	1.2	9- Aug- 23	×
PP1TEM2	674297.0	3049109.3	1.7	23- May- 24	<b>✓</b>	PV3TEM5	676686.0	3056500.0	1.5	9- Aug- 23	×
PP1TEM3	673304.0	3046890.0	2.9	30- Jul- 23	<b>✓</b>	PV4TEM1	677164.0	3055280.0	1.1	9- Aug- 23	×
PP1TEM4	672502.0	3045070.0	2.5	30- Jul- 23	×	PV4TEM2	677044.0	3055370.0	4.3	18- Aug- 23	×
PP1TEM5	671348.0	3042426.0	2.2	30- Jul- 23	×	PV4TEM3	676751.0	3055600.0	1.9	18- Aug- 23	×
PP1TEM6	670919.6	3041423.0	1.9	30- Jul- 23	×	PV4TEM4	676545.0	3055740.0	0.9	18- Aug- 23	×
PP1TEM7	670490.9	3040418.5	1.8	9- May- 24	×	PV5TEM1	676589.0	3054280.0	3.0	1- Aug- 23	×
PV10TM1	675569.0	3051890.0	1.2	30- Jul- 23	×	PV5TEM2	676475.0	3054390.0	3.8	1- Aug- 23	×
PV10TM3	675448.0	3052000.0	2.3	18- Aug- 23	×	PV6TEM2	676445.0	3053990.0	5.8	1- Aug- 23	×
PV10TM5	675265.0	3052110.0	3.8	18- Aug- 23	×	PV6TEM3	676234.0	3054124.0	2.7	1- Aug- 23	×
PV10TM6	675114.0	3052100.0	2.5	18- Aug- 23	×	PV6TEM5	675988.0	3054300.0	2.0	1- Aug- 23	×

PV11TM01	673843.0	3048130.0	1.6	30- Jul- 23	*	PV6TEM6	675679.0	3054420.0	2.3	1- Aug- 23	×
PV11TEM1_R	673803.8	3048091.6	1.9	15- Sep- 23	×	PV6TEM7	675003.0	3054400.0	2.0	1- Aug- 23	×
PV11TM03	673674.0	3048222.0	3.1	15- Sep- 23	*	PV6TEM8	673643.5	3054428.2	1.8	1- Aug- 23	×
PV11TM04	673453.0	3048440.0	2.0	15- Sep- 23	×	PV7TEM2	676263.0	3053640.0	3.5	1- Aug- 23	×
PV11TM05	673198.0	3048630.0	2.5	15- Sep- 23	×	PV7TEM4	676059.0	3053650.0	1.7	1- Aug- 23	×
PV11TM06 R	672825.8	3048793.7	2.3	15- Sep- 23	<b>√</b>	PV7TEM5	675821.0	3053670.0	1.6	1- Aug- 23	×
PV11TM06	672922.0	3048770.0	1.9	23- May- 24	<b>√</b>	PV7TEM6	675549.0	3053680.0	1.3	1- Aug- 23	×
PV11TM07	672783.4	3048844.5	2.1	26- Jan- 24	<b>✓</b>	PV8TEM2	675983.0	3053000.0	3.6	1- Aug- 23	×
PV11TM08	672625.8	3048947.8	2.2	26- Jan- 24	<b>√</b>	PV8TEM3	675818.0	3053100.0	2.4	1- Aug- 23	×
PV11TM09	672500.9	3048981.8	1.8	26- Jan- 24	<b>✓</b>	PV8TEM4	675632.0	3053230.0	1.2	1- Aug- 23	×
PV11TM10	672338.6	3049073.2	2.2	26- Jan- 24	<b>✓</b>	PV8TEM5	675527.0	3053240.0	1.3	1- Aug- 23	×
PV11TM11	672157.7	3049156.0	2.0	26- Jan- 24	<b>√</b>	PV9TEM1	675892.0	3052680.0	4.4	1- Aug- 23	×
PV11TM12	672012.3	3049169.5	1.2	26- Jan- 24	<b>√</b>	PV9TEM4	675569.0	3052810.0	1.3	18- Aug- 23	×
PV12TEM01	671829.0	3043560.0	1.9	30- Jul- 23	<b>√</b>	PV9TEM5	675456.0	3052900.0	1.2	1- Aug- 23	×
PV12TEM01_R	671865.0	3043640.3	1.9	23- May- 24	<b>√</b>	PR22TEM1	673238.1	3049813.5	2.8	23- May- 24	<b>✓</b>

PV12TEM03	671607.0	3043700.0	2.8	15- Sep- 23	×	PR22TEM2	672274.2	3047355.2	2.5	23- May- 24	<b>✓</b>
PV12TEM4	671555.2	3043962.9	1.9	23- May- 24	<b>✓</b>	PR22TEM3	671598.2	3045686.7	1.6	23- May- 24	<b>✓</b>
PV12TEM5	671354.4	3044114.1	1.8	23- May- 24	✓	PR22TEM4	670395.0	3042902.8	1.7	23- May- 24	<b>✓</b>
PV12TEM6_R	671205.6	3044227.3	1.9	9- May- 24	✓	PR22TEM5	669899.8	3042058.2	1.7	23- May- 24	<b>✓</b>
PV12TEM06	671211.2	3044256.2	1.8	23- May- 24	✓	PR22TEM6	669664.1	3040380.4	2.0	23- May- 24	×
PV12TEM07	671003.1	3044364.1	1.6	9- May- 24	<b>✓</b>	Urban TEM 2	674019.4	3052718.1	2.6	23- May- 24	×
PV12TEM08	670897.2	3044448.0	1.0	9- May- 24	<b>√</b>	Urban TEM 3	675623.5	3055628.0	2.5	23- May- 24	×
PV12TEM09	670722.9	3044623.9	1.2	9- May- 24	<b>✓</b>	Urban TEM 5	674930.0	3056217.6	2.3	23- May- 24	<b>✓</b>
PV12TEM10	670691.4	3044756.5	1.1	9- May- 24	<b>✓</b>	Urban TEM1	674390.3	3052533.9	2.8	23- May- 24	×
PV12TEM11	670427.1	3044791.6	1.0	9- May- 24	✓	Washover	677987.8	3057524.1	1.1	13- Jun- 24	×
PV12TEM12	670258.3	3044848.0	0.6	9- May- 24	✓						

Table S2. Resistivity and thickness of subsurface layers, along with station elevation statistics of all the TDEM stations.

	FWL Resistivity (Ω.m)	Salt/Brackish water layer Resistivity (Ω.m)	Clay Layer Resistivity (Ω.m)	FWL Thickness (m)	Salt/Brackish water layer Thickness (m)	Clay Layer Depth (m)	Station Elevation (m)
Mean	32.5	3.9	0.3	7.7	5.5	13.1	2.1
Standard Deviation	18.1	1.4	0.3	4.5	4.0	4.9	0.9
Range	78.3	6.9	1.3	18.5	18.1	22.3	5.6
Minimum	8.0	1.0	0.02	0.0	0.6	0.6	0.6
Maximum	82.3	7.9	1.3	18.5	18.7	22.9	6.2

Table S3. Resistivity and thickness of subsurface layers, along with station elevation and dune volume statistics for stations in various zones across the island.

	FWL Resistivity (Ω.m)	FWL Thickness (m)	Clay Layer Depth (m)	Station Elevation (m)	Dune volume (m³)
Zone 1		1			1
Mean	32	4.6	15	1.8	18918
Standard Deviation	16	2.4	4	0.5	14882
Range	56	6.2	19	1.9	40890
Minimum	9	1.4	4	1	22
Maximum	65	7.6	23	3	40912
Zone 2	·	•			
Mean	37	10	13	3.0	15518
Standard Deviation	15	3	4	1.3	17777
Range	52	10	15	5.0	58079
Minimum	11	5	5	1.2	40
Maximum	63	15	20	6.0	58120
Zone 3					
Mean	34	9.3	14.0	1.9	16796
Standard Deviation	20	4.4	5.0	0.6	16853
Range	74	18.0	17.7	2.9	54754
Minimum	9	1.5	3.3	0.9	0
Maximum	83	18.5	21.0	3.8	54754
Zone 4					
Mean	25	8	10.0	1.9	9925
Standard Deviation	13	3	4.8	0.7	8831
Range	42	13	16.9	2.4	27560
Minimum	10	0.6	0.6	0.6	0
Maximum	52	13.6	17.5	3.0	27560

#### References

- Abdelrehim, R., Ahmed, M., Everett, M.E., 2023. Hydrogeologic controls on barrier island geomorphology: Insights from electromagnetic surveys. Lead. Edge 42, 608–614. https://doi.org/10.1190/tle42090608.1
- Abouelmagd, R.G., Barseem, M.S.M., Metwally, S.E.M., Farag, M.S.M., Mousa, S.E.A., 2020.

  Groundwater Exploration in Fractured Rocks Using Transient Electromagnetic Technique (
  TEM), West El-Minia, Egypt. Egypt. Geophys. Soc. 18, 145–154.
- Adeoti, L., Alile, O.M., Uchegbulam, O., 2010. Geophysical investigation of saline water intrusion into freshwater aquifers: A case study of Oniru, Lagos state. Sci. Res. Essays 5, 248–259.
- Al-Garni, M.A., El-Kaliouby, H.M., 2011. Delineation of saline groundwater and sea water intrusion zones using transient electromagnetic (TEM) method, Wadi Thuwal area, Saudi Arabia. Arab. J. Geosci. 4, 655–668. https://doi.org/10.1007/s12517-009-0094-5
- Aly, S.A., Farag, K.S.I., Atya, M.A., Badr, M.A.M., 2018. Use of electromagnetic–terrain conductivity and DC–resistivity profiling techniques for bedrock characterization at the 15th-of-May City extension, Cairo, Egypt. NRIAG J. Astron. Geophys. 7, 107–122. https://doi.org/10.1016/j.nrjag.2018.03.005
- Anderson, J.B., Wallace, D.J., Simms, A.R., Rodriguez, A.B., Milliken, K.T., 2014. Variable response of coastal environments of the northwestern Gulf of Mexico to sea-level rise and climate change: Implications for future change. Mar. Geol. 352, 348–366. https://doi.org/10.1016/j.margeo.2013.12.008
- Anderson, W.P., Evans, D.G., Snyder, S.W., 2000. The effects of Holocene barrier-island

- evolution on water-table elevations, Natteras Island, North Carolina, USA. Hydrogeol. J. 8, 390–404. https://doi.org/10.1007/s100400000081
- Archie, G.E., 1942. The electrical resistivity log as an aid in determining some reservoir characteristics. Trans. AIME 146.
- Ardali, A.S., Tezkan, B., Gürer, A., 2018. On the Salt Water Intrusion into the Durusu Lake,
  Istanbul: A Joint Central Loop TEM And Multi-Electrode ERT Field Survey. Pure Appl.
  Geophys. 175. https://doi.org/10.1007/s00024-018-1813-1
- Attwa, M., Günther, T., Grinat, M., Binot, F., 2011. Evaluation of DC, FDEM and IP resistivity methods for imaging perched saltwater and a shallow channel within coastal tidal flat sediments. J. Appl. Geophys. 75, 656–670. https://doi.org/10.1016/j.jappgeo.2011.09.002
- Ault, T., 2016. Island water stress. Nat. Clim. Chang. 6, 1062–1063. https://doi.org/10.1038/nclimate3171
- Babu, R., Park, N., Yoon, S., Kula, T., 2018. Sharp interface approach for regional andwell scale modeling of small island freshwater lens: Tongatapu island. Water (Switzerland) 10. https://doi.org/10.3390/w10111636
- Badan Ghyben, W., 1889. Nota in verband met de voorgenomen putboring nabij Amsterdam.

  Tijdshrift van het koninklyk Inst. van Ingenieurs 21.
- Barbier, E.B., 2015. Climate change impacts on rural poverty in low-elevation coastal zones. Estuar. Coast. Shelf Sci. 165, A1–A13. https://doi.org/10.1016/j.ecss.2015.05.035
- Barrett, B., Heinson, G., Hatch, M., Telfer, A., 2002. Geophysical methods in saline groundwater studies: Locating perched water tables and fresh-water lenses. Explor. Geophys. 33, 115–

- 121. https://doi.org/10.1071/EG02115
- Baztan, J., Chouinard, O., Jorgensen, B., Tett, P., Vanderlinden, J.P., Vasseur, L., 2015. Coastal Zones: Solutions for the 21st Century. https://doi.org/10.1016/B978-0-12-802748-6.02001-5
- Berkebile, C.A., Hay, R., 1995. Phase I Groundwater Resource Investigation at the Padre Island National Seashore.
- Brown, L.F., McGowen, J.H., Evans, T.J., Groat, C.G., Fisher, W.L., 1977. Environmental geologic atlas of the Texas coastal zone: Kingsville area, Texas, Bur. of Economic Geology, Austin, TX, U.S.A.
- Collins, W.H., Easley, D.H., 1999. Fresh-Water Lens Formation in an Unconfined Barrier-Island Aquifer. JAWRA J. Am. Water Resour. Assoc. 35, 1–22. https://doi.org/https://doi.org/10.1111/j.1752-1688.1999.tb05448.x
- Conroy, S.J., Milosch, J.L., 2011. An Estimation of the Coastal Premium for Residential Housing Prices in San Diego County. J. Real Estate Financ. Econ. 42, 211–228. https://doi.org/10.1007/s11146-009-9195-x
- Constable, S.C., Parker, R.L., Constable, C.G., 1987. Occam's inversion: a practical algorithm for generating smooth models from electromagnetic sounding data. Geophysics 52. https://doi.org/10.1190/1.1442303
- Cooper, J.A.G., Jackson, D.W.T., Dawson, A.G., Dawson, S., Bates, C.R., Ritchie, W., 2012.

  Barrier islands on bedrock: A new landform type demonstrating the role of antecedent topography on barrier form and evolution. Geology 40, 923–926.

- Costabel, S., Siemon, B., Houben, G., Günther, T., 2017. Geophysical investigation of a freshwater lens on the island of Langeoog, Germany Insights from combined HEM, TEM and MRS data. J. Appl. Geophys. 136, 231–245.

  https://doi.org/10.1016/j.jappgeo.2016.11.007
- Cozzolino, D., Greggio, N., Antonellini, M., Giambastiani, B.M.S., 2017. Natural and anthropogenic factors affecting freshwater lenses in coastal dunes of the Adriatic coast. J. Hydrol. 551, 804–818. https://doi.org/10.1016/j.jhydrol.2017.04.039
- Davis, R.A.J., 1999. The Evolving Coast, The Geographical Journal. https://doi.org/10.2307/3060522
- El-Kaliouby, H., Abdalla, O., 2015. Application of time-domain electromagnetic method in mapping saltwater intrusion of a coastal alluvial aquifer, North Oman. J. Appl. Geophys. 115, 59–64. https://doi.org/10.1016/j.jappgeo.2015.02.003
- Everett, M.E., 2013. Near-Surface Applied Geophysics. Cambridge University Press.
- Falgàs, E., Ledo, J., Marcuello, A., Queralt, P., Falgàs, E., Ledo, J., Marcuello, A., Queralt, P., 2009. Monitoring freshwater-seawater interface dynamics with audiomagnetotelluric data.
  NSGeo 7, 391–400. https://doi.org/10.3997/1873-0604.2009038
- Fetter, C.W.J., 1972. Position of the Saline Water Interface beneath Oceanic Islands. Water Resour. Res. 8, 1307–1315. https://doi.org/https://doi.org/10.1029/WR008i005p01307
- Fisher, K.R., Ewing, R.C., Tice, M., Nachon, M., Duran Vinent, O., 2021. Trends in barrier island geomorphology under continuous sea level rise: Padre Island from 1940-2020.
- Garrison, J.R., McCoy, B., 2007. The Nueces incised valley revisited: A reinterpretation of the

- sedimentology and depositional sequence stratigraphy of preserved Pleistocene and Holocene valley-fill sediments. Gulf Coast Assoc. Geol. Soc. 57, 291–304.
- Garrison, J.R., Williams, J., Miller, S.P., Weber, E.T., McMechan, G., Zeng, X., 2010. Ground-penetrating radar study of North Padre Island: implications for barrier island internal architecture, model for growth of progradational microtidal barrier islands, and Gulf of Mexico sea-level cyclicity. J. Sediment. Res. 80, 303–319.
- Geng, X., Boufadel, M.C., 2017. The influence of evaporation and rainfall on supratidal groundwater dynamics and salinity structure in a sandy beach. Water Resour. Res. 53, 6218–6238. https://doi.org/10.1111/j.1752-1688.1969.tb04897.x
- Geonics Limited, 1995. EM31-MK2 Operating Manual.
- Goldman, M.M., 1988. Transient electromagnetic inversion based on an approximate solution to the forward problem. Geophysics 53. https://doi.org/10.1190/1.1442394
- Golshan, M., Colombani, N., Mastrocicco, M., 2018. Assessing aquifer salinization with multiple techniques along the Southern Caspian Sea shore (Iran). Water (Switzerland) 10. https://doi.org/10.3390/w10040348
- Gonçalves, R., Farzamian, M., Monteiro Santos, F.A., Represas, P., Mota Gomes, A., Lobo de
  Pina, A.F., Almeida, E.P., 2017. Application of Time-Domain Electromagnetic Method in
  Investigating Saltwater Intrusion of Santiago Island (Cape Verde). Pure Appl. Geophys.
  174, 4171–4182. https://doi.org/10.1007/s00024-017-1642-7
- Grzegorzewski, A.S., Cialone, M.A., Wamsley, T. V., 2011. Interaction of barrier islands and storms: Implications for flood risk reduction in Louisiana and Mississippi. J. Coast. Res.

- 2011, 156–164. https://doi.org/10.2112/SI59-016.1
- Harris, W.H., 1967. Stratification of fresh and salt water on Barrier Islands as a result of differences in sediment permeability. Water Resour. Res. 3, 89–97.https://doi.org/10.1029/WR003i001p00089
- Heath, R.C., 1983. Basic Ground-Water Hydrology, U.S. Geological Survey Water-Supply paper 2220. https://doi.org/10.1002/job.4030160708
- Henry, H.R., 1964. Interfaces between salt water and fresh water in coastal aquifers. Geol. Surv. Water-Supply Pap. 1613–C, 70–83.
- Herzberg, A., 1901. Die wasserversorgung einiger Nordseebader. J. Gasbeleucht. Wasserversorg. 44, 815–819.
- Hill, G.W., Hunter, R.E., 1976. Interaction of biological and geological processes in the beach and nearshore environments, northern Padre Island, Texas, in: Richard A. Davis, J.,Ethington, R.L. (Eds.), Beach and Nearshore Sedimentation. Special Publications of SEPM.
- Holt, T., Greskowiak, J., Seibert, S.L., Massmann, G., 2019. Modeling the Evolution of a Freshwater Lens under Highly Dynamic Conditions on a Currently Developing Barrier Island. Geofluids 2019. https://doi.org/10.1155/2019/9484657
- Houser, C., Barrineau, P., Hammond, B., Saari, B., Rentschler, E., Trimble, S., Wernette, P., Weymer, B., Young, S., 2018. Role of the foredune in controlling barrier island response to sea level rise. Barrier Dyn. response to Chang. Clim. 175–207.
- Houser, C., Hamilton, S., 2009. Sensitivity of post-hurricane beach and dune recovery to event frequency. Earth Surf. Process. Landforms 34, 613–628.

- Houser, C., Hapke, C., Hamilton, S., 2008. Controls on coastal dune morphology, shoreline erosion and barrier island response to extreme storms. Geomorphology 100, 223–240. https://doi.org/10.1016/j.geomorph.2007.12.007
- Hunter, R.E., Dickinson, K.A., 1970. Map showing landforms and sedimentary deposits of the Padre Island portion of the South Bird Island 7.5-minute quadrangle, Texas. US Geological Survey.
- Interpex, 2008. Interpex Limited, 2008. IX1D v3 Instruction Manual, Version 1.11. Interpex Limited, Golden, Colorado.
- Ismail, M., Pradhanang, S.M., Boving, T., Motta, S., McCarron, B., Volk, A., 2024. Review of Modeling Approaches at the Freshwater and Saltwater interface in Coastal Aquifers. Land 13, 1–23. https://doi.org/10.3390/land13081332
- Jin, D., Hoagland, P., Au, D.K., Qiu, J., 2015. Shoreline change, seawalls, and coastal property values. Ocean Coast. Manag. 114, 185–193.
  https://doi.org/10.1016/j.ocecoaman.2015.06.025
- Kalisperi, D., Kouli, M., Vallianatos, F., Soupios, P., Kershaw, S., Lydakis-Simantiris, N., 2018.A Transient ElectroMagnetic (TEM) Method Survey in North-Central Coast of Crete,Greece: Evidence of Seawater Intrusion. Geosciences 8, 107.
- Kanta, A., Soupios, P., Barsukov, P., Kouli, M., Vallianatos, F., 2013. Aquifer characterization using shallow geophysics in the Keritis Basin of Western Crete, Greece. Environ. Earth Sci. 70. https://doi.org/10.1007/s12665-013-2503-z
- Kiflai, M.E., Whitman, D., 2023. Geophysical mapping of freshwater lens in Big Pine Key,

- Florida: Electromagnetic Induction Calibration and Application. Near Surf. Geophys. 21, 152–167. https://doi.org/10.1002/nsg.12244
- Kourgialas, N.N., Dokou, Z., Karatzas, G.P., Panagopoulos, G., Soupios, P., Vafidis, A., Manoutsoglou, E., Schafmeister, M., 2016. Saltwater intrusion in an irrigated agricultural area: combining density-dependent modeling and geophysical methods. Environ. Earth Sci. 75. https://doi.org/10.1007/s12665-015-4856-y
- Laignel, B., Vignudelli, S., Almar, R., Becker, M., Bentamy, A., Benveniste, J., Birol, F.,
  Frappart, F., Idier, D., Salameh, E., Passaro, M., Menende, M., Simard, M., Turki, E.I.,
  Verpoorter, C., 2023. Observation of the Coastal Areas, Estuaries and Deltas from Space.
  Surv. Geophys. 44, 1309–1356. https://doi.org/10.1007/s10712-022-09757-6
- Leatherman, S.P., 1976. Barrier island dynamics: overwash processes and eolian transport, in:

  Coastal Engineering 1976. American Society of Civil Engineers, New York, pp. 1958–
  1974.
- Ley, A., Haehnel, P., Bormann, H., 2023. Addressing the challenges of climate scenario-based impact studies in modelling groundwater recharge on small barrier islands at the German North Sea coast. J. Hydrol. Reg. Stud. 50, 101578.
  https://doi.org/10.1016/j.ejrh.2023.101578
- Ling, Z., Shu, L., Sun, Y., Wang, R., Li, Y., 2021. Impact of island urbanization on freshwater lenses: A case study on a small coral island. Water (Switzerland) 13, 1–17. https://doi.org/10.3390/w13223272
- Martínez-Moreno, F.J., Monteiro-Santos, F.A., Bernardo, I., Farzamian, M., Nascimento, C., Fernandes, J., Casal, B., Ribeiro, J.A., 2017. Identifying seawater intrusion in coastal areas

- by means of 1D and quasi-2D joint inversion of TDEM and VES data. J. Hydrol. 552, 609–619.
- Martorana, R., Lombardo, L., Messina, N., Luzio, D., 2014. Integrated geophysical survey for 3D modelling of a coastal aquifer polluted by seawater. Near Surf. Geophys. 12, 45–59. https://doi.org/10.3997/1873-0604.2013006
- McNeill, J.D., 1980. Electromagnetic Terrain Conductivity Measurement at Low Induction Numbers. Geonics Ltd. Tech. Note TN-6, Mississauga, Ontario, Canada.
- Nabighian, M.N., Corbett, J.D., 1991. Electromagnetic Methods in Applied Geophysics. Society of Exploration Geophysics. https://doi.org/https://doi.org/10.1190/1.9781560802686
- Nicholls, R.J., Wong, P.P., Burket, V.R., Codignotto, J., Hay, J.E., McLean, R.F., Ragoonaden,
  S., Woodroffe, C.D., 2007. Coastal systems and low-lying areas, in: M.L. Parry, Canziani,
  O.F., Palutikof, J.P., Linden, P.J. van der, Hanson, C.E. (Eds.), Climate Change 2007:
  Impacts, Adaptation and Vulnerability. Cambridge University Press, Cambridge, UK, pp.
  315–356.
- Nielsen, L., Jørgensen, N.O., Gelting, P., 2007. Mapping of the freshwater lens in a coastal aquifer on the Keta Barrier (Ghana) by transient electromagnetic soundings. J. Appl. Geophys. 62, 1–15. https://doi.org/10.1016/j.jappgeo.2006.07.002
- NOAA, 2023. What threats do coastal communities face? National Ocean Service website [WWW Document]. URL https://oceanservice.noaa.gov/facts/coastalthreat.html (accessed 5.25.23).
- NOAA, 2021. What is a barrier island? National Ocean Service website [WWW Document].

- URL https://oceanservice.noaa.gov/facts/barrier-islands.html (accessed 5.25.23).
- Nott, J., 2006. Tropical cyclones and the evolution of the sedimentary coast of northern Australia. J. Coast. Res. 22, 49–62.
- NPS, 2024. Weather [WWW Document]. Weather Forecast Malaquite Beach Area. URL https://www.nps.gov/pais/planyourvisit/weather.htm (accessed 7.6.24).
- Paepen, M., Hanssens, D., De Smedt, P., Walraevens, K., Hermans, T., 2020. Combining resistivity and frequency domain electromagnetic methods to investigate submarine groundwater discharge in the littoral zone. Hydrol. Earth Syst. Sci. 24, 3539–3555. https://doi.org/10.5194/hess-24-3539-2020
- Paine, J.G., 2003. Determining salinization extent, identifying salinity sources, and estimating chloride mass using surface, borehole, and airborne electromagnetic induction methods.

  Water Resour. Res. 39. https://doi.org/10.1029/2001WR000710
- Panthi, J., Boving, T.B., Pradhanang, S.M., Russoniello, C.J., Kang, S., 2024. The contraction of freshwater lenses in barrier island: A combined geophysical and numerical analysis. J.
   Hydrol. 637, 131371. https://doi.org/10.1016/j.jhydrol.2024.131371
- Patra, H.P., Bhattacharya, P.K., 1966. Geophysical exploration for ground water around Digha in the coastal region of West Bengal, India. Geoexploration 4. https://doi.org/10.1016/0016-7142(66)90019-6
- Pendleton, E.A., Thieler, E.R., Williams, S.J., Beavers, R.L., 2004. Coastal Vulnerability

  Assessment of Padre Island National Seashore (PAIS) to Sea-Level Rise: US Geological

  Survey Open-File Report 2004-1090, 1-25.

- https://doi.org/https://www.researchgate.net/publication/237683541
- Pondthai, P., Everett, M.E., Micallef, A., Weymer, B.A., Faghih, Z., Haroon, A., Jegen, M., 2020. 3D characterization of a coastal freshwater aquifer in SE malta (mediterranean sea) by time-domain electromagnetics. Water (Switzerland) 12. https://doi.org/10.3390/W12061566
- Reid, J.E., Howlett, A., 2001. Application of the EM-31 terrain conductivity meter in highly-conductive regimes. Explor. Geophys. 32, 219–224.
- Ruggiero, P., Hacker, S., Seabloom, E., Zarnetske, P., 2018. The role of vegetation in determining dune morphology, exposure to sea-level rise, and storm-induced coastal hazards: a US Pacific Northwest perspective, in: Barrier Dynamics and Response to Changing Climate. Springer, pp. 337–361.
- Russoniello, C.J., Konikow, L.F., Kroeger, K.D., Fernandez, C., Andres, A.S., Michael, H.A., 2016. Hydrogeologic controls on groundwater discharge and nitrogen loads in a coastal watershed. J. Hydrol. 538. https://doi.org/10.1016/j.jhydrol.2016.05.013
- Sallenger Jr, A.H., 2000. Storm impact scale for barrier islands. J. Coast. Res. 16, 890–895.
- Sathish, S., Elango, L., 2016. An integrated study on the characterization of freshwater lens in a coastal aquifer of Southern India. Arab. J. Geosci. 9. https://doi.org/10.1007/s12517-016-2656-7
- Satish Kumar, V., Dhakate, R., Amarender, B., Sankaran, S., 2016. Application of ERT and GPR for demarcating the saline water intrusion in coastal aquifers of Southern India. Environ. Earth Sci. 75, 1–17. https://doi.org/10.1007/s12665-015-5207-8

- Schneider, J.C., Kruse, S.E., 2006. Assessing selected natural and anthropogenic impacts on freshwater lens morphology on small barrier Islands: Dog Island and St. George Island, Florida, USA. Hydrogeol. J. 14, 131–145. https://doi.org/10.1007/s10040-005-0442-9
- Schneider, J.C., Kruse, S.E., 2003. A comparison of controls on freshwater lens morphology of small carbonate and siliciclastic islands: Examples from barrier islands in Florida, USA. J. Hydrol. 284, 253–269. https://doi.org/10.1016/j.jhydrol.2003.08.002
- Sherwood, C.R., Ritchie, A.C., Over, J.S.R., Kranenburg, C.J., Warrick, J.A., Brown, J.A.,
  Wright, C.W., Aretxabaleta, A.L., Zeigler, S.L., Wernette, P.A., Buscombe, D.D.,
  Hegermiller, C.A., 2023. Sound-Side Inundation and Seaward Erosion of a Barrier Island
  During Hurricane Landfall. J. Geophys. Res. Earth Surf. 128, 1–32.
  https://doi.org/10.1029/2022JF006934
- Shevnin, V., Mousatov, A., Ryjov, A., Delgado-rodriquez, O., 2007. Estimation of clay content in soil based on resistivity modelling and laboratory measurements. Geophys. Prospect. 55, 265–275. https://doi.org/10.1111/j.1365-2478.2007.00599.x
- Shideler, G.L., 1986. Seismic and physical stratigraphy of late Quaternary deposits, South Texas coastal complex. US Geol. Surv. Prof. Pap. 1328, 9–31.
- Simms, A.R., Anderson, J.B., Blum, M., 2006. Barrier-island aggradation via inlet migration:

  Mustang Island, Texas. Sediment. Geol. 187, 105–125.

  https://doi.org/10.1016/j.sedgeo.2005.12.023
- Small, C., Nicholls, R.J., 2003. A global analysis of human settlement in coastal zones. J. Coast. Res. 19, 584–599.

- Soupios, P.M., Kalisperi, D., Kanta, A., Kouli, M., Barsukov, P., Vallianatos, F., 2010. Coastal aquifer assessment based on geological and geophysical survey, northwestern Crete, Greece. Environ. Earth Sci. 61, 63–77.
- Stone, G.W., McBride, R.A., 1998. Louisiana Barrier Islands and their importance in wetland protection: Forecasting shoreline change and subsequent response of wave climate. J. Coast. Res. 14.
- Stutz, M.L., Pilkey, O.H., 2011. Open-ocean barrier islands: Global influence of climatic, oceanographic, and depositional settings. J. Coast. Res. 27, 207–222. https://doi.org/10.2112/09-1190.1
- Tajul Baharuddin, M.F., Othman, A.R., Taib, S., Hashim, R., Zainal Abidin, M.H., Radzuan, M.A., 2013. Evaluating freshwater lens morphology affected by seawater intrusion using chemistry-resistivity integrated technique: A case study of two different land covers in Carey Island, Malaysia. Environ. Earth Sci. 69, 2779–2797. https://doi.org/10.1007/s12665-012-2098-9
- Thissen, L., Greskowiak, J., Gaslikova, L., Massmann, G., 2024. Climate change impact on barrier island freshwater lenses and their transition zones: a multi-parameter study.

  Hydrogeol. J. https://doi.org/10.1007/s10040-024-02800-3
- Todd, D.K., Mays, L.W., 2004. Groundwater hydrology. John Wiley & Sons.
- Torres, J., Kulp, M., FitzGerald, D., Georgiou, I., Lepper, K., 2020. Geomorphic and temporal evolution of a Mississippi delta flanking barrier island: Grand Isle, LA. Mar. Geol. 430, 106341. https://doi.org/10.1016/j.margeo.2020.106341

- TPWD, 2024. Texas Parks and Wildlife Department, Upper Laguna Madre [WWW Document].

  URL https://tpwd.texas.gov/landwater/water/habitats/bays/ulm/ulm\_index.phtml (accessed 7.4.23).
- Trabelsi, F., Mammou, A. Ben, Tarhouni, J., Piga, C., Ranieri, G., 2013. Delineation of saltwater intrusion zones using the time domain electromagnetic method: The Nabeul-Hammamet coastal aquifer case study (NE Tunisia). Hydrol. Process. 27. https://doi.org/10.1002/hyp.9354
- Tully, K., Gedan, K., Epanchin-Niell, R., Strong, A., Bernhardt, E.S., Bendor, T., Mitchell, M., Kominoski, J., Jordan, T.E., Neubauer, S.C., Weston, N.B., 2019. The invisible flood: The chemistry, ecology, and social implications of coastal saltwater intrusion. Bioscience. https://doi.org/10.1093/biosci/biz027
- UNEP, 2014. The importance of mangroves to people: A call to action, United Nations Environment Programme World Conservation Monitoring Centre.
- Urisha, D.W., Ozbilginb, M.M., 1989. The Coastal Ground-Water Boundary. Ground Water 27, 310–315.
- USGS, 2022. What is the vertical accuracy of the 3D Elevation Program (3DEP) DEMs? [WWW Document]. URL https://www.usgs.gov/faqs/what-vertical-accuracy-3d-elevation-program-3dep-dems (accessed 5.25.23).
- USGS, 2020. U.S. Geological Survey, 20200330, USGS one meter x69y309 TX South B5 2018:

  U.S. Geological Survey [WWW Document]. URL

  https://www.sciencebase.gov/catalog/item/5ead063282cefae35a253d64 (accessed 5.25.23).

- Vafidis, A., Soupios, P., Economou, N., Hamdan, H., Andronikidis, N., Kritikakis, G.,
  Panagopoulos, G., Manoutsoglou, E., Steiakakis, M., Candansayar, E., Schafmeister, M.,
  2014. Seawater intrusion imaging at Tybaki, Crete, using geophysical data and joint inversion of electrical and seismic data. First Break 32. https://doi.org/10.3997/1365-2397.32.8.76970
- Van der veer, P., 1977. Analytical solution for a two-fluid flow in a coastal aquifer involving a phreatic surface with precipitation. J. Hydrol. 35, 271–278. https://doi.org/10.1016/0022-1694(77)90006-3
- Weise, B.R., White, W.A., 1980. Padre Island National Seashore: a guide to the geology, natural environments, and history of a Texas barrier island. Bureau Of Economic Geology, Austin, Texas.
- Werner, A.D., Bakker, M., Post, V.E.A., Vandenbohede, A., Lu, C., Ataie-Ashtiani, B., Simmons, C.T., Barry, D.A., 2013. Seawater intrusion processes, investigation and management: Recent advances and future challenges. Adv. Water Resour. 51, 3–26. https://doi.org/10.1016/j.advwatres.2012.03.004
- Wernette, P., Houser, C., Bishop, M.P., 2016. An automated approach for extracting Barrier Island morphology from digital elevation models. Geomorphology 262, 1–7. https://doi.org/10.1016/j.geomorph.2016.02.024
- Wernette, P., Houser, C., Weymer, B.A., Everett, M.E., Bishop, M.P., Reece, B., 2018. Influence of a spatially complex framework geology on barrier island geomorphology. Mar. Geol. 398, 151–162. https://doi.org/10.1016/j.margeo.2018.01.011
- Winker, C.D., 1979. Late Pleistocene fluvial-deltaic deposition, Texas coastal plain and shelf.

GCAGS Transactions.

- Withers, K., Smith, E., Gomez, O., Wood, J., 2004. Assessment of Coastal Water Resources and Watershed Conditions at Padre Island National Seashore, Texas.
- Wu, C.L.R., Stigter, T.Y., Craig, S.G., 2022. Assessing the Quantity and Quality Controls of the Freshwater Lens on a Semi-Arid Coral-Limestone Island in Sri Lanka. Front. Water 4, 1–18. https://doi.org/10.3389/frwa.2022.832227

#### 3- Section (III)

# Integrated Geophysical-Geospatial Analysis of Breach-Prone Zones on Northern Padre Island

Sections I and II demonstrated that geologic-stratigraphic features (GSF) vary systematically alongshore, cross-shore, and with depth and that this spatial variability governs dune height, width, and, ultimately, island topography. Building on those findings, Section II presented a refined three-dimensional model of the barrier-island system that links subsurface architecture to dune morphology, surface drainage, and groundwater salinity. This model pinpoints where Padre Island is most sensitive to sea-level rise, saltwater intrusion, and storm-induced breaching.

This section combines that subsurface framework with high-resolution geospatial data to delineate breach-susceptible corridors across developed and undeveloped portions of northern Padre Island. The resulting maps give stakeholders three practical tools:

- **a- Smart zoning** steer new construction away from corridors prone to breaching, saltwater intrusion, or freshwater-lens thinning.
- **b- Targeted engineering** identify reaches that warrant immediate or future interventions such as dune restoration, sand fencing, or shoreline stabilization.
- **c- Adaptive planning** design long-term mitigation strategies that protect critical infrastructure while preserving the island's ecological and recreational value.

#### 3.1 Elevation-Based Vulnerability Framework

Island inundation and breaching are governed first and foremost by topographic defence—specifically dune crest height and dune-ridge width. Broad, high dunes dissipate wave energy and block storm surge; narrow, low dunes fail early and open pathways for marine water and sediment. To translate this principle into planning guidance, we classified northern Padre Island into four elevation bands corresponding to progressively lower resilience against tidal flooding, storm surge, and saltwater intrusion (Figure 3-1).

Table 3- 1 Elevation-based vulnerability classes for northern Padre Island. This table groups island terrain into four elevation bands (NAVD88) and summarizes, for each band, the typical hydrodynamic forcing required to cause flooding or breaching, the expected recurrence interval based on regional hurricane climatology, and key management implications (e.g., permitting restrictions, dune-nourishment priorities). Higher classes (III–IV) correspond to wider, higher dune ridges that offer robust protection. Classes I–II identify low-lying corridors exposed to daily tidal inundation or frequent storm-surge overtopping.

Viilnerahility	Elevation Range (NAVD88)	Hydrodynamic	Recurrence Expectation*	Management Implications
Class I – High Vulnerability	0 – 1 m	,	Continuous / seasonal	Preserve as intertidal wetlands or wash-over corridors; no permanent infrastructure
Class II – Moderate Vulnerability	1 – 3 m	$\mathcal{C}^{J}$	Annual to biennial	Restrict new development; elevate critical utilities; consider dune fencing / vegetation planting
Class III – Low Vulnerability	3 – 5 m			Maintain dune volume; designate emergency

Viilnerahility	Elevation Range (NAVD88)	Typical Hydrodynamic Exposure		Management Implications
		hurricanes; surge $\approx 3$ –5 m (8–16 ft)		breach-closure stockpiles
Class IV – Very Low Vulnerability	> 5 m	Compromised only by exceptionally large Cat 4–5 events (return period > 50 yr)	Multidecadal to centennial	Suitable for critical facilities if backed by redundant protection; monitor for gradual lowering by aeolian processes

<sup>\*</sup>Based on regional hurricane climatology and SLOSH surge envelopes for the South Texas coast.

# **Key points**

- **Dune geometry matters as much as crest height.** A 4 m dune that is only 15 m wide stores far less sand than a 3 m dune that is 60 m wide: width controls post-storm recovery time. Consequently, our GIS overlay weights dune-ridge width (at 1 m resolution) alongside elevation when mapping Classes II–IV.
- Classes are additive with subsurface risk factors. Areas that fall into Class II for elevation but coincide with high-conductivity paleochannels (Sections I–II) are promoted to Class I+ to flag compounded vulnerability.
- Management thresholds align with existing TGLO guidance. The 3 m contour
  roughly tracks the landward limit of active overwash observed during Hurricanes Dolly
  (2008) and Hanna (2020); the 5 m contour matches FEMA's Coastal High Hazard Zone
  in this reach.

Figure 3-1 presents the resulting **Elevation-Based Vulnerability Map**, providing a rapid visual tool for identifying where dune nourishment, setback requirements, or conservation easements will deliver the greatest resilience return per dollar invested.

## 3.2 Composite Elevation-Conductivity Screening for Breach Susceptibility

Figure 3-2 merges two independent indicators of coastal resilience—dune-ridge geometry and subsurface electrical conductivity—to pinpoint where breaching, erosion, and overwash are most likely to occur.

# 3.2.1 Mapping the Robust Dune Core

- Extraction logic. All terrain ≥ 3 m NAVD88 is classified as Low (Class III) to Very Low
  (Class IV) vulnerability (see Table 3-1). These higher, wider ridges form the island's
  primary storm barrier.
- Cartographic symbol. In Figure 3-2 the preserved dune core is shown as black, hollow polygons; their interior shading (yellow for Class III, gray for Class IV) conveys the relative protection level.
- Interpretation. Where these polygons are broad—tens of meters wide and dominated by Class IV cells—the likelihood of storm-induced breaching drops sharply because the ridge stores sufficient sand to absorb wave run-up and recover post-storm.

# 3.2.2 Subsurface Salinity Proxy: Frequency-Domain EM Conductivity

Data source. Apparent conductivity was measured with frequency-domain EM (FDEM) profiling and binned into three ranges: 195–272 mS m<sup>-1</sup> (blue), 272–300 mS m<sup>-1</sup> (green), and > 300 mS m<sup>-1</sup> (pink).

 Hydro-geomorphic meaning. Elevated conductivity signals shallow saltwater and/or finer-grained, water-saturated sediments, both symptomatic of low elevation, frequent inundation, and, ultimately, greater breach potential.

# 3.2.3 Spatial Patterns and Management Hotspots

- Northern segment (Figure 3-2a).
  - O Dominated by  $> 300 \text{ mS m}^{-1}$  anomalies coincident with thin Class I–II ridges.
  - The area includes the most intensely developed real estate and the north Packery
     Channel, which has a history of overwashing openings.
  - Recommendation: impose stricter building setbacks, bolster dune-walkover design, and prioritize dune-volume augmentation.

# • Central barrier (Figure 3-2c).

- Narrow belts of high conductivity thread through otherwise moderate ridges,
   creating pinch-points where breaching could initiate.
- Recommendation: targeted vegetation planting or sand fencing to widen the dune toe and interrupt these conductive corridors.

#### • Southern segment (Figure 3-2d).

- Ridges are markedly wider, with extensive Class III–IV cover, yet isolated **pink** circles still flag pockets of > 300 mS m<sup>-1</sup>.
- Recommendation: monitor these patches; if conductivity or shoreline-retreat rates increase, elevate them to priority sites for future intervention.

Overall, areas where narrow Class I and II ridges overlap pink (> 300 mS m<sup>-1</sup>) conductivity cells define the island's highest composite risk. Conversely, sectors with wide Class IV ridges and blue conductivity represent the island's natural "backbone," demanding only routine management.

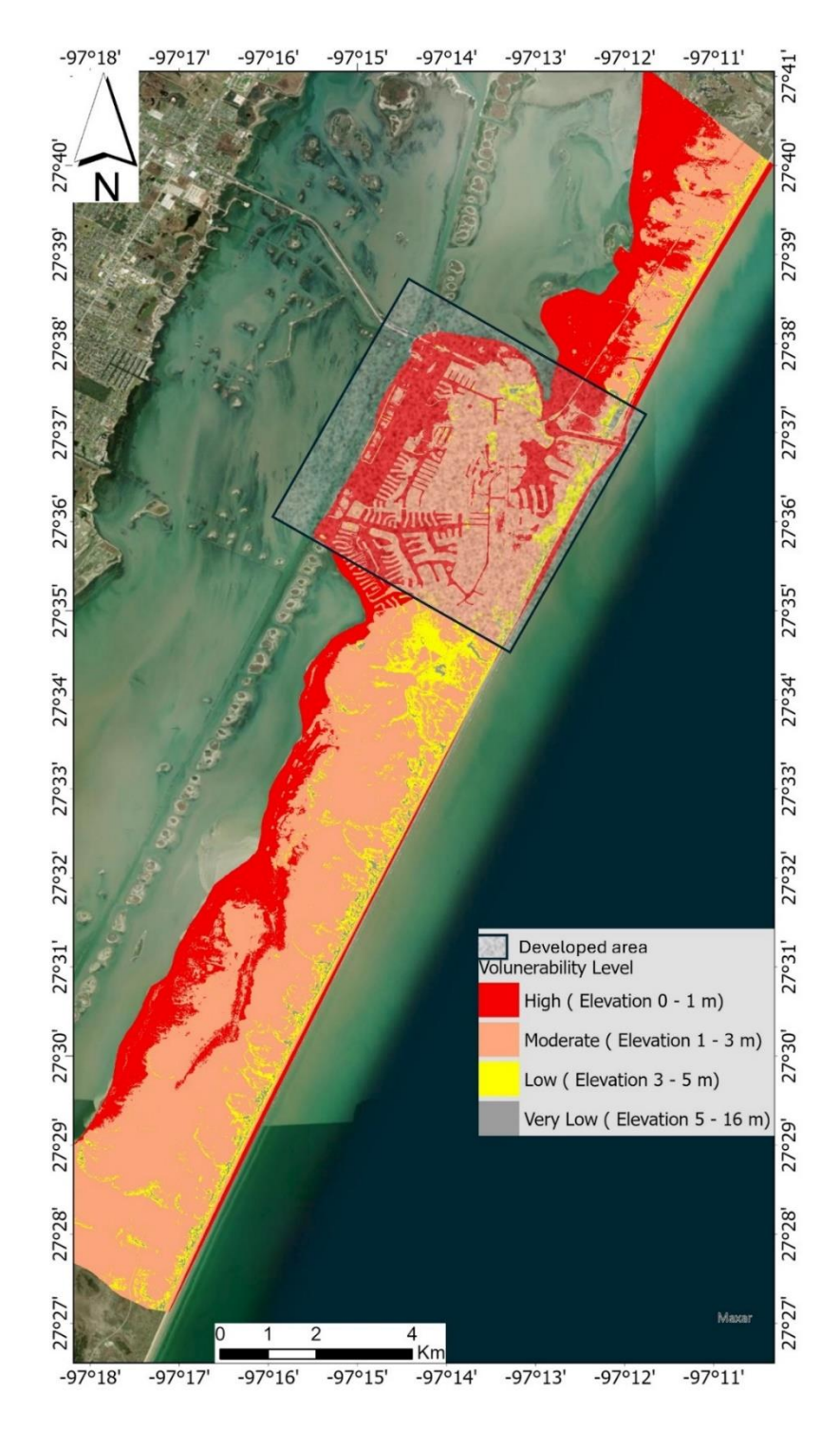


Figure 3- 1. Elevation-based vulnerability map of northern Padre Island. Colored polygons delineate four elevation bands derived from 1-m USGS LiDAR (NAVD88): Class I (0–1 m, red), Class II (1–3 m, orange), Class III (3–5 m, yellow), and Class IV (> 5 m, gray). Warmer colors indicate progressively higher susceptibility to daily tidal flooding, storm-surge overtopping, and barrier-island breaching, as summarized in Table 3-1. Gray hatching marks developed areas.

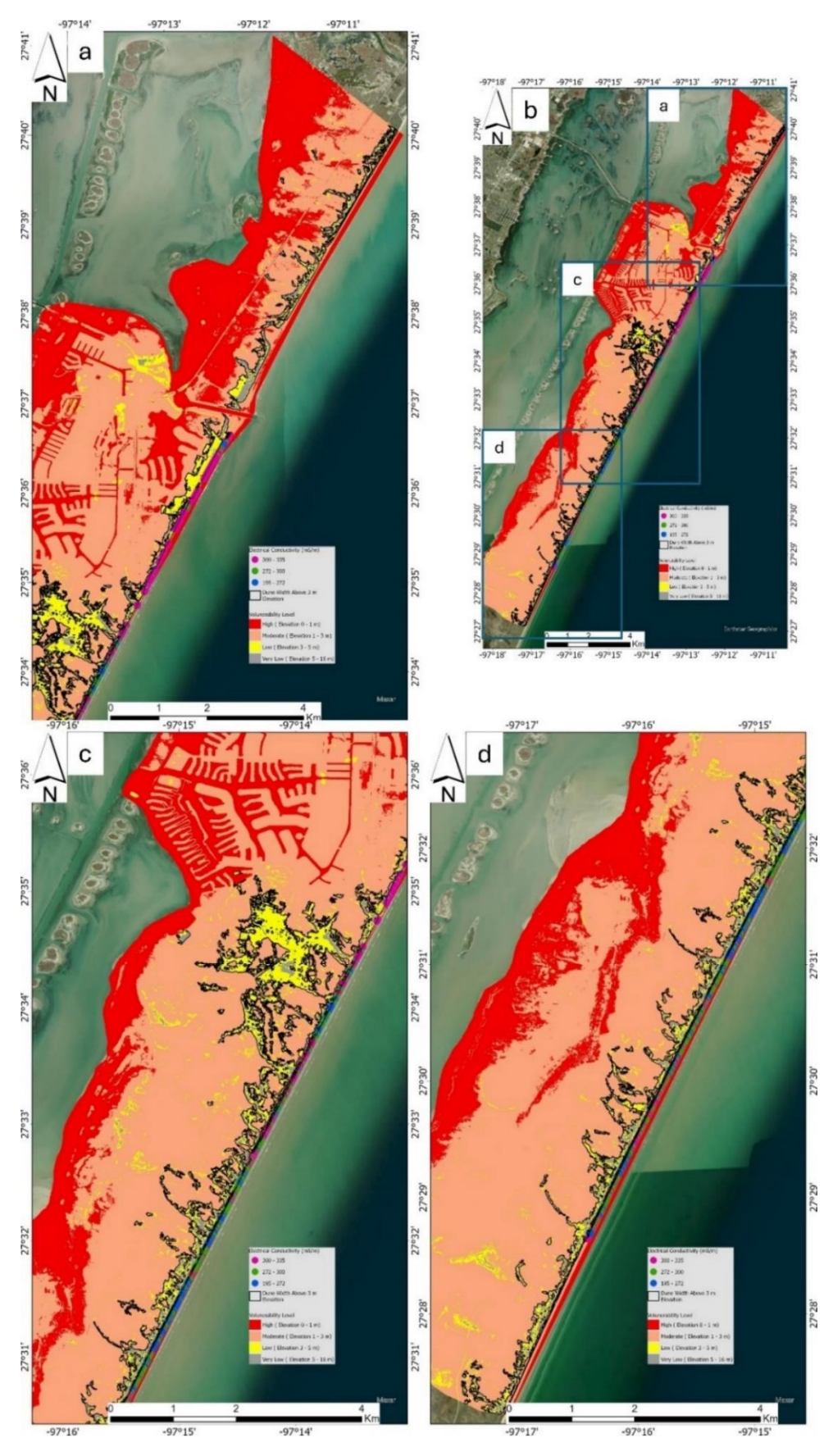


Figure 3- 2. Composite breach-susceptibility map integrating dune-ridge elevation and subsurface electrical conductivity. Panel (a) is the entire study area. Panels (a, c, and d) progress from north to south along northern Padre Island. Hollow black polygons outline the dune-core corridor where ground elevation is ≥ 3 m NAVD88 (Classes III–IV; interior shading: yellow = Class III, gray = Class IV). Superimposed circles plot FDEM apparent conductivity, color-coded by salinity proxy: blue (195–272 mS m<sup>-1</sup>), green (272–300 mS m<sup>-1</sup>), and pink (> 300 mS m<sup>-1</sup>). Narrow Class I–II ridges overlain by pink, high-conductivity points mark the island's highest composite risk—locations with shallow saline groundwater, thin dunes, and a documented history of overwash (e.g., panel a, north of Packery Channel). Conversely, wide Class IV ridges with blue conductivity denote the island's most resilient backbone (e.g., panel d). This dual-layer visualization guides managers to prioritize dune nourishment, setback enforcement, and monitoring where natural defenses are weakest.

#### 3.3 Subsurface Controls on Breach Susceptibility

Time-domain electromagnetic (TDEM) soundings define the island's three-dimensional hydrostratigraphic framework, which we translate into spatial indicators of storm-breach risk (Figures 3-3 to 3-5).

# **3.3.1** Fresh-Water Lens (FWL) Resistivity (Figures 3-3)

The palette expresses pore-water salinity:

- Cool colors (high resistivity  $\geq 15 \Omega$  m) = fresh to brackish water.
- Warm colors (low resistivity < 15  $\Omega$  m) = more saline groundwater or tidal saturation.

Where low-resistivity cells hug the surface (red circles), the freshwater lens is already thinned or absent, signaling frequent marine inundation and a reduced capacity to buffer saltwater intrusion.

# 3.3.2 Thickness of the FWL (Figures 3-4)

FWL thickness is calculated as the vertical distance between the saline interface (resistivity  $\approx 8$   $\Omega$  m) and the land surface.

- Thick lens (≥ 8 m, greens and blues) coincides with the widest, highest dunes; these zones experience minimal overwash and show long recovery times after storms.
- Thin lens (< 8 m, reds and yellows) marks sectors where fine sands, silts, and clays lie close to the surface, inviting rapid salinization and facilitating scour during storm run-up.

# 3.3.3 Depth to Pleistocene Clay Base (Figure 3-5)

The Pleistocene clay represents the mechanical "floor" of Padre Island. Its depth controls the thickness of the erodible sand column:

- **Deep clay** (> 18 m) provides a substantial sandy buffer against wave attack.
- Shallow clay (< 8 m) means only a thin veneer of sand overlies easily erodible, low-permeability clay; once exposed, this material promotes scour pits that can evolve into permanent breach channels.

# 3.3.4 Composite Interpretation

Across all three maps, three hotspots emerge (red circles):

- North of Packery Channel (developed reach). Low resistivity, thin FWL, and shallow clay converge beneath an already narrow dune ridge—explaining the corridor's history of repetitive overwash cuts.
- 2. **The southern part of the developed area.** Despite moderate dune elevation, the FWL thins abruptly landward, creating a latent salinity conduit that could accelerate breaching if the foredune erodes.
- 3. **Southern study area.** Here, the clay base shoals to < 6 m and the lens pinches out, producing a broad saline swale that undercuts dune stability.

These subsurface indicators corroborate the surface-based risk patterns outlined in Section 3.2, reinforcing the need for heightened monitoring, restrictive zoning, and targeted dune-nourishment in the flagged corridors.

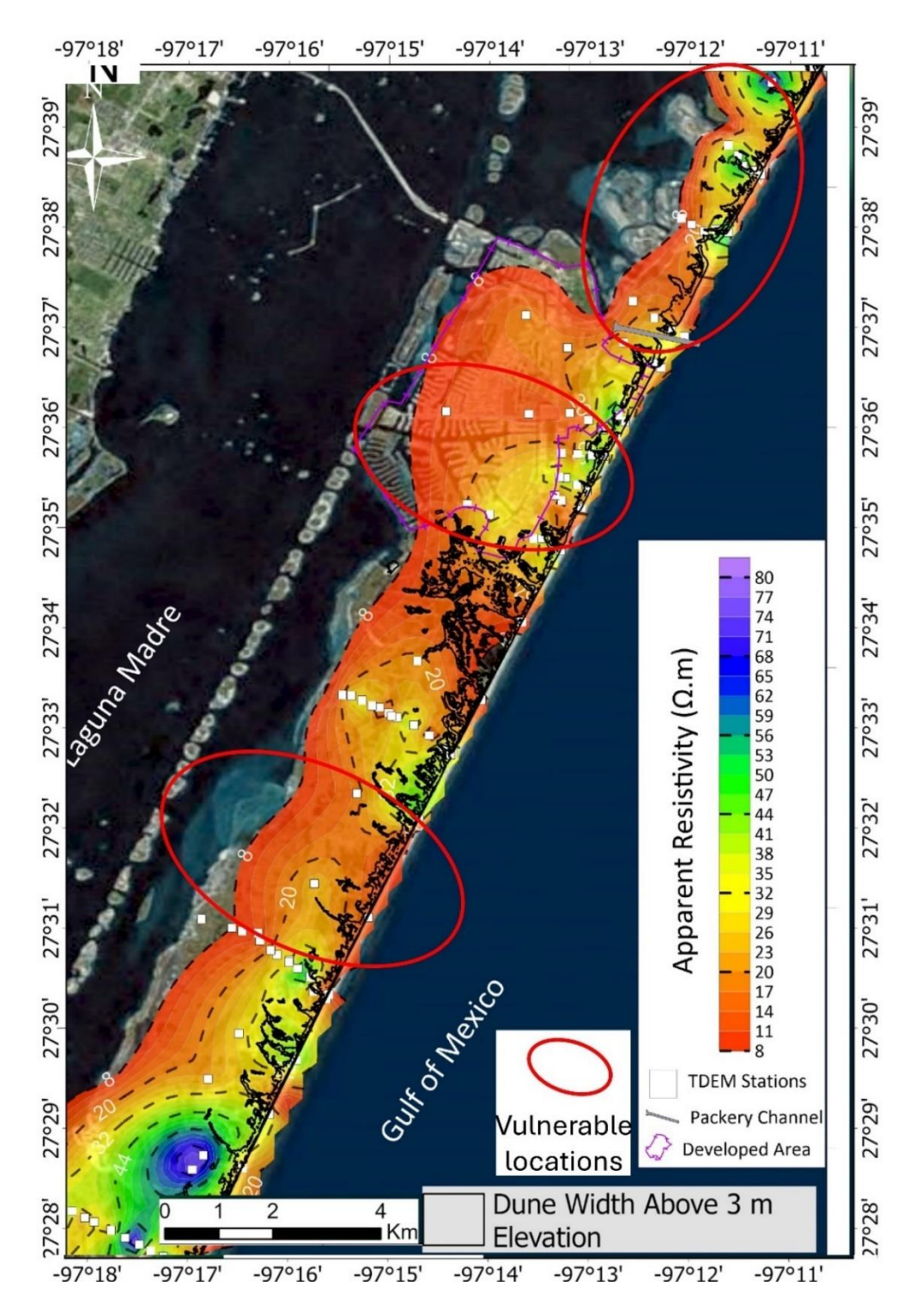


Figure 3- 3. Fresh-water-lens resistivity map derived from TDEM soundings. Cool colors ( $\geq$  15  $\Omega$  m) indicate fresh-brackish groundwater; warm colors (< 15  $\Omega$  m) reveal shallow saline intrusion and frequent tidal saturation. Red circles mark the most saline, breach-prone corridors.

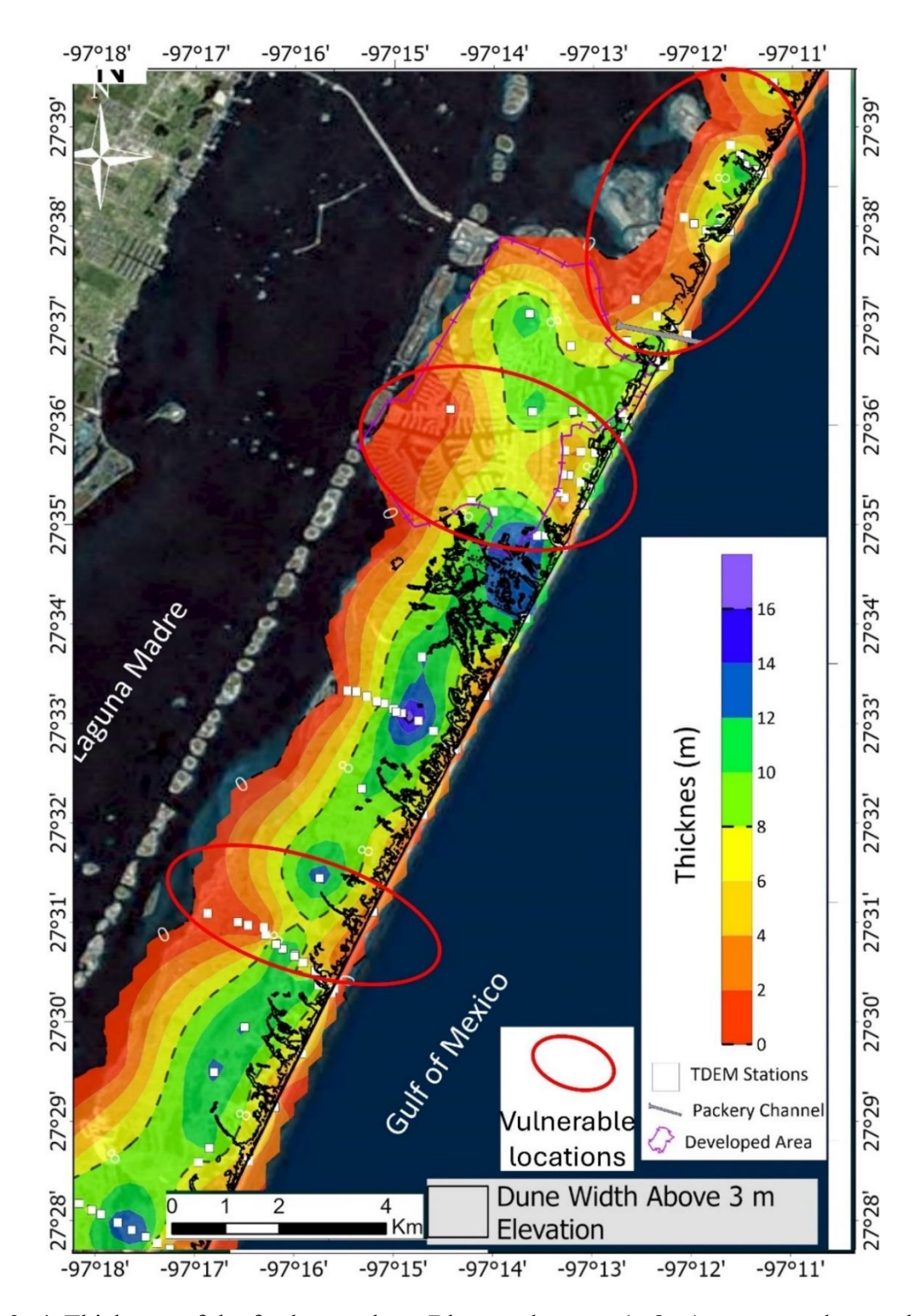


Figure 3- 4. Thickness of the freshwater lens. Blues and greens (≥ 8 m) correspond to a robust lens beneath wide, high dunes, whereas reds and yellows (< 8 m) flag areas where the lens has nearly pinched out—zones prone to rapid salinization, overwash, and eventual breaching. Critical thinning sectors are circled in red.

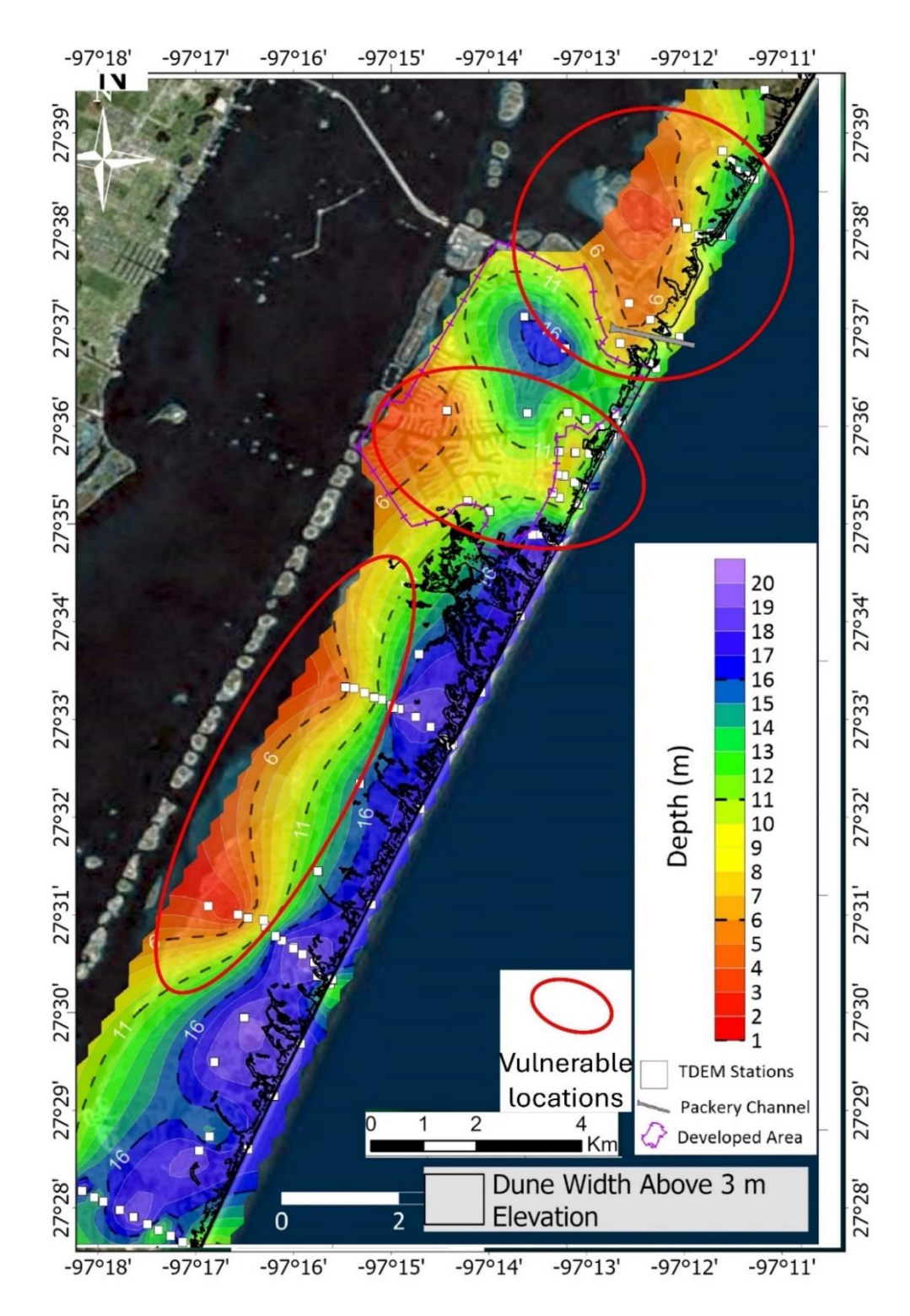


Figure 3- 5. Depth to the Pleistocene clay layer. Deep clay (> 18 m, blue) provides a substantial sandy buffer; shallow clay (< 8 m, red) means only a thin, easily erodible sand veneer overlies the island's clay floor, elevating scour and breach risk. Red circles highlight the shallowest, most vulnerable pocket